UNIVERSITY OF CALIFORNIA, SAN DIEGO

Linearization of CDMA Receiver Front-Ends

A dissertation submitted in partial satisfaction of the

requirements for the degree Doctor of Philosophy

in

Electrical Engineering (Electronic Circuits & Systems)

by

Vladimir Aparin

Committee in charge:

Professor Lawrence Larson, Chair
Professor Peter Asbeck
Professor Paul Yu
Professor William Trogler
Professor Andrew Kummel

2005

The dissertation of Vladimir Aparin is approved, and it is acceptable in quality and form for publication on microfilm:

_____

_____

_____

_____

_____
Chair

University of California, San Diego

2005

To my mother, who always supported me.

TABLE OF CONTENTS

LIST OF FIGURES

LIST OF TABLES

ACKNOWLEDGEMENTS

I would like to thank my advisor, Professor Lawrence Larson, for encouraging me to start my graduate studies and for his continuous support throughout these studies. I would also like to thank the members of my committee, Professors Peter Asbeck, Paul Yu, William Trogler, and Andrew Kummel, for their patience and understanding.

I also wish to thank Brian Butler, who found an error in my analysis of cross modulation distortion using the new CDMA signal model. Without catching that error, the theoretical explanation of the “double-hump” spectrum shape would not be possible.

Special thanks to Charlie Persico for his support of my research at QUALCOMM and to Dale Carmichael for his test support.

The text of Chapters II, IV, V and VI in this dissertation, in part or in full, is a reprint of the material as it appears in our published papers or as it has been submitted for publication in *IEEE Transactions on Microwave Theory and Techniques*, *IEEE International Microwave Symposium*, *IEEE RFIC Symposium*, *IEEE International Symposium on Circuits and Systems*, and *European Solid-State Circuits Conference*. The dissertation author was the primary author listed in these publications directed and supervised the research which forms the basis for these chapters.

VITA

1983–1989	Diploma of Engineer-Physicist, Electronics and Automatics (with Honors), Moscow Institute of Electronic Engineering (MIEE), Russian Federation
1989–1992	MIEE, Moscow, Russian Federation
1992–1996	Hittite Microwave Corp., Woburn, MA, United States
1996–present	QUALCOMM Inc., San Diego, CA, United States
2001–2005	Ph.D., Electrical Engineering (Electronic Circuits & Systems), University of California, San Diego, CA, United States

PUBLICATIONS

V. Aparin and C. Persico, "Effect of out-of-band terminations on intermodulation distortion in common-emitter circuits," *IEEE MTT-S Int. Microwave Symp. Dig.*, vol. 3, pp. 977-980, 1999.

V. Aparin and L. E. Larson, "Analysis and reduction of cross modulation distortion in CDMA receivers," *IEEE Trans. Microwave Theory Tech.*, vol. 51, no. 5, pp. 1591-1602, May 2003.

V. Aparin and L. E. Larson, "Linearization of monolithic LNAs using low-frequency low-impedance input termination," *Europ. Solid-State Circ. Conf.*, pp. 137-140, Sept. 2003.

V. Aparin, G. Brown, and L. E. Larson "Linearization of CMOS LNAs via optimum gate biasing," *IEEE Int. Symp. on Circ. and Sys.*, vol. IV, pp. 748-751, May 2004.

V. Aparin and L. E. Larson "Modified derivative superposition method for linearizing FET low-noise amplifiers," *IEEE RFIC Symp. Dig.*, pp. 105-108, June 2004.

V. Aparin and L. E. Larson, "Analysis of cross modulation in W-CDMA receivers," *IEEE MTT-S Int. Microwave Symp. Dig.*, vol. 2, pp. 787-790, June 2004.

V. Aparin and L. E. Larson "Modified derivative superposition method for linearizing FET low-noise amplifiers," *IEEE Trans. Microwave Theory Tech.*, vol. 53, no. 2, Feb. 2005.

FIELDS OF STUDY

Major Field: Electrical and Computer Engineering

Studies in Linearization Techniques of Low Noise Amplifiers

Professor Lawrence E. Larson

ABSTRACT OF THE DISSERTATION

Linearization of CDMA Receiver Front-Ends

by

Vladimir Aparin

Doctor of Philosophy in Electrical Engineering (Electronic Circuits & Systems)

University of California, San Diego, 2005

Professor Lawrence E. Larson, Chair

The CDMA receiver sensitivity can be significantly degraded by the cross modulation distortion (XMD), which is generated primarily by the LNA. To analyze XMD, this dissertation proposes a new model of the reverse-link CDMA signal. The derived XMD expression is used to specify the requirement to the input 3rd-order intercept point (IIP_3) of CDMA LNAs.

Among linearization techniques suitable for the CDMA LNA design, this dissertation investigates the optimum out-of-band tuning, optimum gate biasing, and derivative superposition (DS) methods. These techniques are analyzed using the Volterra series. Practical LNA designs are used to confirm the theoretical results.

The optimum out-of-band tuning can be applied to both the difference-frequency and 2nd-harmonic terminations, or just one of them. It is shown that optimizing both terminations results in a higher IIP_3, but the latter is very sensitive to the tone frequency. Using

just a low-frequency low-impedance input termination is more suitable for high-volume production, but it works only under certain restrictions on the BJT cut-off frequency, the emitter degeneration impedance and the 2nd-harmonic input termination.

This dissertation proposes a novel bias circuit to automatically generate the gate-source voltage at which the 3rd-order derivative of the FET transfer characteristic is zero. However, at RF, the IIP_3 peak shifts from this voltage and becomes smaller due to the 2nd-order interaction. The proposed optimum tuning of the drain load impedance improves IIP_3, but its peak remains shifted relative to the bias for zero derivative. Thus, a manual bias adjustment is required, which makes IIP_3 very sensitive to the bias variations.

The DS method extends the bias voltage range in which a significant IIP_3 improvement is achieved. However, the 2nd-order interaction still degrades IIP_3 at RF. A modified DS method is proposed to improve IIP_3. An observation is made that the composite FET in both the conventional and modified DS methods exhibits a higher NF than that of a single FET. This phenomenon is theoretically attributed to the contribution of the induced gate noise of the FET operating in the subthreshold region.

Chapter I

Introduction

I.1 Coexistence of Wireless Standards

The genesis of todays wireless technology began in the early 1980s with the introduction of the analog cellular systems, which were designated as the First Generation (1G). These systems utilized frequency modulation for speech encoding and frequency division multiplexing as an access technique. They supported only voice communications, had poor sound quality, low cell capacity, short battery life, and were vulnerable to fraud and eavesdropping. This technology is still being used in many parts of the world today.

The explosive growth in the number of mobile subscribers demanded a higher cell capacity. As a result, in early 1990s, the Second Generation (2G) standards were introduced. Unlike the analog 1G systems, the 2G systems rely on digital modulation and sophisticated digital signal processing. They are categorized by two multiple access techniques: Time Division Multiple Access (TDMA) and Code Division Multiple Access (CDMA) [1]. The TDMA-based Global System for Mobile communications (GSM) has become the world's most widely used digital air interface due to its early entry and universal acceptance as a pan-European standard, which allowed roaming throughout the European Union. The latter

feature proved to be so desirable that GSM was accepted in many other parts of the world. Though superior to TDMA, CDMA[1] took a distant 2nd position in the world and became dominant in North America, Japan, and South Korea. Besides increasing cell capacity and voice quality, the 2G systems enabled wireless data transmission, longer battery life, and a host of other digitally-based services, such as call waiting, call forwarding, caller ID, and encryption.

Following the demand for high data-rate applications, such as internet access and wireless video, the third generation (3G) systems were introduced in late 2001. Two rival 3G standards were proposed: Wideband CDMA (WCDMA)[2] and CDMA2000. The differences between these two standards are relatively minor, mostly small discrepancies in parameter choices, with one exception: the issue of whether or not to synchronize base stations. The CDMA2000 standard was designed to be an evolutionary path for cdmaOne system, whereas WCDMA was proposed as a replacement for GSM, without backward compatibility.

The process of upgrading wireless networks with next generation technologies is not instantaneous and universal; it depends on readiness of base station operators. Therefore, in the same geographical area covered by different service providers, several standards can coexist. This coexistence is especially diverse in the US, which has adopted the policy of *technology neutrality*, granting the licensees the freedom to choose any standard. As a result, such carriers as Verizon Wireless and Sprint PCS deployed cdmaOne, while AT&T

[1] To distinguish 2G CDMA systems from 3G CDMA systems, the former are also called cdmaOne.
[2] In Europe, this standard is known as the Universal Mobile Telephone Service (UMTS).

Wireless[3], Cingular Wireless, and T-Mobile deployed GSM. These 2G standards coexist with the Advanced Mobile Phone Service (AMPS) used in 1G systems. The main characteristics of these standards are summarized in Table I.1.

Table I.1: Main characteristics of cellular systems in North America.

Standard	Multiple Access Method	Uplink Frequency Band [MHz]	Downlink Frequency Band [MHz]	Channel Spacing [MHz]
AMPS	FDMA	824-849	869-894	0.03
cdmaOne	CDMA	824-849 (Cellular)	869-894 (Cellular)	1.25
GSM[4]	TDMA	1850-1910 (PCS)	1930-1990 (PCS)	0.2

This coexistence of multiple standards in the same geographical area creates a hostile jamming environment for radio receivers. For example, a cellular cdmaOne phone can be jammed by either AMPS or GSM850 signals transmitted by offending base stations co-sited with the home base stations. The interfering signals degrade the mobile RX sensitivity and, eventually, can cause the handset to drop the call.

This dissertation will concentrate on mobile cdmaOne systems and will use the term “CDMA” instead of “cdmaOne”.

I.2 Cross Modulation Distortion in CDMA Receivers

Mobile CDMA systems use offset quaternary phase-shift keying (OQPSK) spreading, which produces signals with non-constant (time-varying) envelopes. In addition to

[3] AT&T Wireless was acquired by Cingular Wireless on October 27, 2004.

[4] GSM in the US cellular and PCS bands are referred to as GSM850 and GSM1900, respectively.

transmitting non-constant envelope signals, CDMA systems operate in the full-duplex mode; i.e., they receive and transmit signals at the same time. Such an operation requires different frequency bands for signal reception and transmission. The transmitter (TX) and receiver (RX) signal paths are separated at the antenna by a duplex filter (duplexer). Unfortunately, duplexers have a finite isolation between the TX and RX ports, causing a TX signal leakage to the RX input. The reduction in size of phones and, thus, of their components has led to a lower TX-RX isolation attainable in the duplexers. The TX leakage to the RX input is generally not a problem on its own, but it becomes dangerous in the presence of a strong narrowband jammer (an AMPS or a GSM signal transmitted from an offending base station collocated with the home base station). When a CDMA TX leakage and a narrowband jammer pass through the low-noise amplifier (LNA), the odd-order nonlinearities of the latter transfer the modulation from the TX leakage to the jammer, widening its spectrum as shown in Fig. I.1. This widened spectrum of the jammer is called *cross modulation distortion* (XMD). It acts as an added noise. If the desired CDMA signal is received in the channel adjacent to the jammer, XMD of the latter contaminates the desired signal, reducing the RX sensitivity.

Besides XMD, the desired signal is also contaminated by the thermal noise generated by the RX, the TX noise coupled through the duplexer, and the phase noise of the local oscillator (LO) reciprocally mixed with the jammer. A tolerable level of the total interference is specified by the *single-tone desensitization* requirement of the IS-95 standard [2]. To aid the LNA design satisfying this requirement, its XMD must be accurately quantified. It

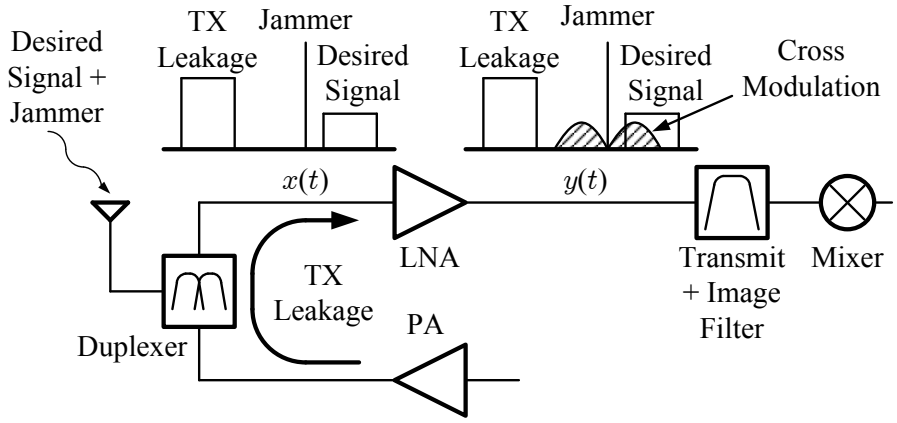

Figure I.1: Cross modulation distortion in a CDMA transceiver.

can be either simulated at the transistor level using harmonic balance or circuit envelope techniques or estimated analytically using behavioral modeling techniques [3], [4]. The transistor-level simulations are rigorous, but require a substantial amount of computer time and memory when a digitally-modulated signal is involved. The behavioral modeling techniques significantly speed up the distortion estimation, but suffer from a lower accuracy due to approximations of their circuit and signal models. The circuit transfer function is typically modeled by a power series [5]-[9] because of its simplicity. By definition, the power series is only applicable to memoryless circuits, i.e., those with zero reactances and, thus, frequency independent characteristics. However, it can be modified to include the memory effects by making the series coefficients complex to fit the single-tone AM-AM and AM-PM characteristics of a circuit [6], [7], or by expressing the series coefficients through the corresponding intercept points, determined with the circuit reactances taken into account [8], [9]. The latter approach is more accurate because it uses more than one discrete tone to characterize the circuit nonlinearity and, thus, accounts for the circuit reactances at a larger

set of frequencies than just dc and harmonics of the fundamental frequency. A circuit can also be modeled by a Volterra series [10] to accurately include the memory effects. But the mathematical complexity of this approach limits its application to single-transistor circuits.

Another challenge of the behavioral modeling techniques is taking into account the pseudo-random nature of a CDMA signal. The analyses presented in [5] and [6] treat a CDMA signal as a Band-Pass Gaussian Noise (BPGN) by using the well-known expansion formulas of the higher-order normal moments [11] to derive the output autocorrelation and spectral density functions. The authors of [12] modeled a CDMA signal in the frequency domain as n equal-power random-phase tones uniformly spaced within the signal bandwidth and derived its distortions using the 2-tone intermodulation analysis. According to the central limit theorem [11], with n approaching infinity, this multi-tone excitation becomes BPGN, and its distortions are described by the same equations derived using the Gaussian noise statistics. The Gaussian approximation of the TX leakage in a CDMA RX leads to a triangle-shaped XMD spectrum [5], but the simulation results presented in [13] and measured data indicate that the XMD spectrum has a "double-hump" shape. As a result of this modeling inaccuracy[5], the Gaussian approximation overestimates the XMD power closer to the jammer and, thus, requires an empirical correction [13]. The BPGN model of a CDMA signal also overestimates its spectral regrowth [9].

[5]The Gaussian approximation can be justifiably used only for a forward-link CDMA signal with a large number of Walsh-coded channels transmitted at the same frequency [7], [8]. These channels are summed in the analog domain before quadrature modulation, and the resulting baseband signal approaches a normal distribution according to the central limit theorem.

I.3 Linearization Techniques

For a mobile CDMA RX to meet the single-tone desensitization requirement, its LNA must be very linear and, at the same time, have a low noise figure (NF) and high power gain. It also should consume a low dc current to extend the battery life and have a low cost. The latter goal recommends the use of Si technology, which offers a low cost material and a high yield. It also offers a high integration level by allowing analog and digital blocks to be integrated on a single chip.

The LNA linearity is typically measured by the 3rd-order intercept point (IP_3), which can be referred to the input (IIP_3) or output (OIP_3). Achieving a high IP_3 in combination with a low NF, high gain, low power consumption, and low-cost technology is a design challenge, which can be met by using linearization techniques. Due to the phone sensitivity to the size and cost of its components, these techniques must be fairly simple. Omitting costly and space-inefficient ones, the linearization methods suitable for a CDMA LNA can be categorized as optimum biasing, linear feedback, optimum out-of-band terminations, analog pre- and post-distortion, nonlinear feedback, and feedforward. The first three methods are based on optimization of the bias of the main active device and passive circuits around it. The last four methods are based on adding nonlinear elements into the circuit to compensate for distortion generated by the main device.

Linearization of LNAs based on envelope tracking has also been reported [14]. However, the interfering input signals of LNAs are typically very weak; therefore, extracting their envelopes without using high gain amplifiers is challenging. Moreover, an LNA is

often subject to multiple interfering signals, including those whose distortion does not contaminate the desired signal. Envelope tracking methods can not separate the "dangerous" interferers from others.

I.3.1 Optimum Biasing

This is the simplest technique. It does not require any additional hardware and uses a device bias at which its IP_3 is maximum.

For a common-emitter BJT biased in the forward-active region and operating at low current levels, the device nonlinearities arise from the bias-dependent transconductance. In this case, the input tone amplitude at the IP_3 is given by

$$A_{\mathrm{IP3}} = \sqrt{8}\phi_{\mathrm{t}}, \tag{I.1}$$

where ϕ_{t} is the thermal voltage kT/q [15]. The IIP_3 can be found in terms of the delivered input power. The dc input resistance of a common-emitter BJT is $R_{\mathrm{in}} = \beta_{\mathrm{F}}\phi_{\mathrm{t}}/I_{\mathrm{C}}$, where β_{F} is the forward dc current gain and I_{C} is the collector dc current. Therefore,

$$\mathrm{IIP}_3 = \frac{A_{\mathrm{IP3}}^2}{2R_{\mathrm{in}}} = \frac{4\phi_{\mathrm{t}}I_{\mathrm{C}}}{\beta_{\mathrm{F}}}. \tag{I.2}$$

We can see from (I.2) that the IIP_3 of a common-emitter BJT is proportional to its collector dc current, and this dependence is often used to implement a high-linearity mode in LNAs [16].

The above simplified analysis shows that IP_3 is independent on the collector-emitter voltage. However, under high current conditions, when the effective transconductance

is dominated by the emitter degeneration impedance (emitter resistance and inductance), the nonlinearity of the collector-base capacitance dominates, and IP_3 increases with the collector-emitter voltage [17]-[22]. The authors of [21] and [22] reported a significant IP_3 peaking at the collector current densities just below the onset of the Kirk effect (base pushout).

For a common-source FET, the IP_3 is a function of the gate-source voltage. It also has a tendency to improve at high currents [23], which has been utilized in high-linearity CMOS LNA designs [24]. But there is a gate bias voltage at the boundary of the moderate and strong inversion regions at which IP_3 exhibits a significant peaking due to a null in the 3rd-order derivative of the FET transfer characteristic [25]-[31]. This null can be utilized to achieve a high linearity. However, it is very narrow and, thus, very difficult to maintain over a wide range of operating conditions and process parameters.

I.3.2 Linear Feedback

Invented by Harold S. Black in 1927 [32], feedback is the most widely known linearization technique. It is based on feeding back a linearly scaled version of the output signal and subtracting it from the input. The block diagram of the method is shown in Fig. I.2. To explain how the feedback affects the 3rd-order distortion, we will describe the open-loop transfer function of the amplifier in Fig. I.2 by the following power series

$$y(t) = a_1 e(t) + a_2 e^2(t) + a_3 e^3(t) + \cdots , \tag{I.3}$$

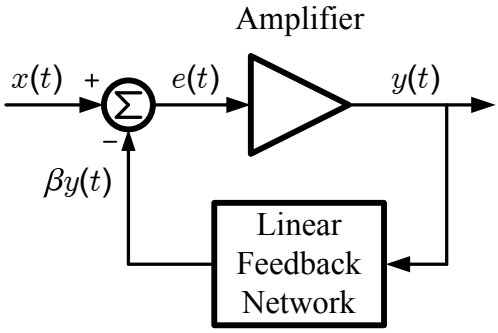

Figure I.2: Linear feedback method.

where a_1 is the open-loop small-signal gain of the amplifier, and the higher-order coefficients (a_2, a_3 etc.) characterize the nonlinearities of the open-loop transfer function. Above, $e(t)$ is the error signal, given by

$$e(t) = x(t) - \beta y(t), \tag{I.4}$$

where β is the feedback factor. The closed-loop transfer function can be represented by a power series as

$$y(t) = c_1 x(t) + c_2 x^2(t) + c_3 x^3(t) + \cdots . \tag{I.5}$$

The coefficients c_n's are functions of a_n's and β. Their derivations can be found in [15] and [33]. The two important coefficients are

$$c_1 = \frac{a_1}{1+T}, \tag{I.6a}$$

$$c_3 = \frac{a_3}{(1+T)^4} - \frac{2a_2^2}{a_1}\frac{T}{(1+T)^5}, \tag{I.6b}$$

where $T = a_1\beta$ is the loop gain. As expected, the negative feedback reduces the small-signal gain of the amplifier by a factor of $(1+T)$. The closed-loop 3rd-order nonlinearity, represented by c_3, has two contributions: that of an open-loop 3rd-order nonlinearity, re-

duced by a factor of $(1+T)^4$, and that of the 2nd-order nonlinearity. The latter contribution is called the *second-order interaction* [15]. For small values of the loop gain T, the first term of (I.6b) is dominant, and

$$c_3 \approx \frac{a_3}{(1+T)^4}, \tag{I.7}$$

and, thus,

$$A_{\mathrm{IP3}} = \sqrt{\frac{4}{3}\left|\frac{c_1}{c_3}\right|} \approx \sqrt{\frac{4}{3}\left|\frac{a_1}{a_3}\right|(1+T)^3}, \tag{I.8}$$

i.e., A_{IP3} is increased by a factor of $(1+T)^{3/2}$ in comparison with the open-loop case. For large loop gains, the second term of (I.6b) dominates. But in most cases, its absolute value is still much smaller than $|a_3|$, resulting in a significantly reduced distortion. It is interesting to note that, under this condition of a strong feedback ($T \gg 1$), c_1 and c_3 have opposite signs, i.e., the closed-loop amplifier always exhibits a gain compression regardless of the behavior of the open-loop amplifier.

By rewriting (I.6b) as

$$c_3 = \frac{a_3}{(1+T)^4}\left(1 - \frac{2a_2^2}{a_1 a_3}\frac{T}{1+T}\right), \tag{I.9}$$

we can see that, if a_1 and a_3 have the same sign (i.e., the open-loop amplifier exhibits gain expansion), c_3 and, thus, the 3rd-order intermodulation distortion (IMD_3) can be made zero by properly selecting the loop gain T as a function of $2a_2^2/(a_1 a_3)$. This IMD_3 cancellation has rarely been used in practical analog circuits because the c_3 null is very narrow and, thus, very difficult to maintain over a wide range of operating conditions and process parameters [33]. At RF, a parasitic ground inductance interferes with the described IMD_3 cancellation [34].

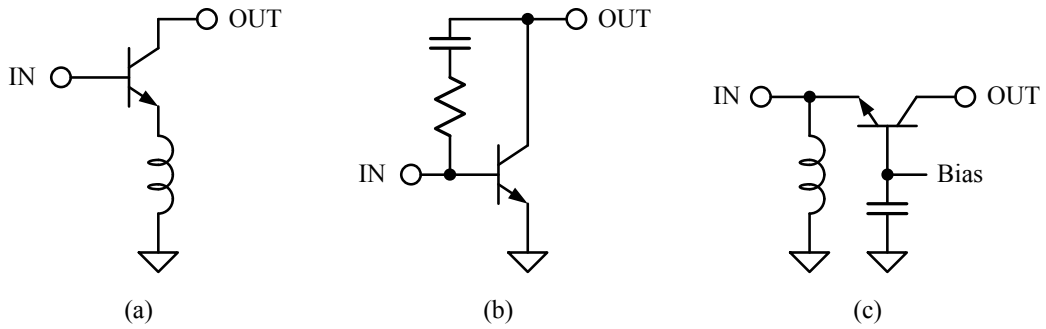

Figure I.3: Examples of negative feedback. (a) Series-series feedback through an emitter degeneration. (b) Shunt-shunt feedback. (c) Shunt-series feedback or a common-base amplifier.

There are three main approaches to apply a negative feedback in an amplifier: a source or emitter degeneration, a parallel resistive feedback, and a common-gate or common-base amplifier. Their examples are illustrated in Fig. I.3. The common-gate or common-base amplifier has the highest linearity among these approaches due to its lower input impedance [35]. However, it is also the least suitable for LNAs due to its high NF [35], [36]. The inductive degeneration has the second best linearity according to the simulation results presented in [37]. It is commonly used in LNAs to bring the conjugate input impedance closer to the source impedance needed for the minimum NF. An improved linearity comes as a benefit. The main drawback of the negative feedback method is the reduced gain.

I.3.3 Optimum Out-of-Band Terminations

This method uses distortion cancellation predicted by (I.9). However, (I.9) was derived assuming that the circuit in Fig. I.2 is broadband, i.e., its characteristics are frequency independent. This assumption is invalid for RF circuits, whose reactances can not be ne-

glected. Let us now consider the case of a frequency dependent feedback factor β. Then, the coefficients c_n's, describing the transfer function of the closed-loop amplifier, will also be frequency dependent. Their derivations can be found in [38] and [39]. The two important coefficients are

$$c_1(\omega) = \frac{a_1}{1+T(\omega)}, \tag{I.10}$$

$$c_3(\omega_1,\omega_2,\omega_3) = \frac{a_3}{(1+T(\omega_\Sigma))(1+T(\omega_1))(1+T(\omega_2))(1+T(\omega_3))} \cdot\left\{1-\frac{2a_2^2}{3a_1a_3}\left[\frac{T(\omega_2+\omega_3)}{1+T(\omega_2+\omega_3)}+\frac{T(\omega_1+\omega_3)}{1+T(\omega_1+\omega_3)}+\frac{T(\omega_1+\omega_2)}{1+T(\omega_1+\omega_2)}\right]\right\}, \tag{I.11}$$

where $T(\omega) = a_1\beta(\omega)$ is the frequency dependent loop gain, and $\omega_\Sigma = \omega_1+\omega_2+\omega_3$. The coefficient $c_3(\omega_1,\omega_2,\omega_3)$ defines the response at $\omega_1+\omega_2+\omega_3$. To find the coefficient that defines the response at the IMD$_3$ frequency $2\omega_1-\omega_2$, we simply replace ω_2 with ω_1 and ω_3 with $-\omega_2$ in (I.11). Assuming closely spaced frequencies, such that $\omega_1 \approx \omega_2 \approx (2\omega_1-\omega_2) \approx \omega$, we get

$$c_3(\omega_1,\omega_1,-\omega_2) \approx \frac{a_3}{(1+T(\omega))^3(1+T(-\omega))}\left\{1-\frac{2a_2^2}{3a_1a_3}\left[\frac{2T(\Delta\omega)}{1+T(\Delta\omega)}+\frac{T(2\omega)}{1+T(2\omega)}\right]\right\}, \tag{I.12}$$

where $\Delta\omega = \omega_1-\omega_2$. This expression is more general than (I.9). IMD$_3$ is cancelled when the expression in the braces of (I.12) is zero. The second term in the braces represents the contribution of the 2nd-order nonlinearity to IMD$_3$. This nonlinearity generates the difference-frequency ($\Delta\omega$) and 2nd-harmonic (2ω) responses and, after they are fed back to the amplifier input, mixes them with the fundamental excitations, producing the $2\omega_1-\omega_2$ and $2\omega_2-\omega_1$ IMD$_3$ responses. The amplitude and phase of the 2nd-order contributions to

IMD_3 depend on the values of the feedback components and the termination impedances of the circuit at $\Delta\omega$ and 2ω, which is reflected by $T(\Delta\omega)$ and $T(2\omega)$. These frequencies are typically outside of the operating frequency band; therefore, the values of $T(\Delta\omega)$ and $T(2\omega)$ can be adjusted to reduce IMD_3 by tuning the out-of-band terminations of the circuit without affecting its in-band operation. This is the idea behind the linearization method using the optimum out-of-band tuning. It is not necessary to have an intentional feedback path for this method to work. The feedback can exist through circuit parasitics, such as transistor capacitances and a parasitic inductance in the ground path of a common-emitter circuit.

The effect of out-of-band terminations on IMD_3 has already been recognized [40]-[59]. The low-frequency input termination impedance is considered to be particularly important in reducing IMD_3. To prevent the difference-frequency response from modulating the bias, this impedance is typically made as low as possible [42]-[56]. However, its optimum value is in general nonzero and complex [57]. It adjusts the amplitude and phase of the difference-frequency response appearing at the circuit input such that the product of its mixing with the fundamental response cancels the remaining IMD_3 terms. Second-harmonic tuning has also been used to improve linearity of amplifiers [58]-[60].

The described method of optimizing the circuit out-of-band terminations to reduce its IMD_3 is somewhat related to *low-frequency* and *2nd-harmonic feedback* techniques [61]-[66]. These techniques introduce intentional feedback paths at the corresponding frequencies to achieve a certain degree of the distortion cancellation according to (I.12).

I.3.4 Analog Predistortion

The idea of adding nonlinear elements to compensate for the distortion already present in a circuit is not new [67]. The predistortion method adds a nonlinear element (also called *linearizer*) prior to an amplifier such that the combined transfer characteristic of the two devices is linear. In practice though, it is impossible to cancel all orders of nonlinearity simultaneously; therefore, the linearizer is usually designed to cancel the nonlinearity of a certain order. The cancellation of the 3rd-order nonlinearity is more common because it controls IMD_3 and the gain compression or expansion of an amplifier. If the amplifier exhibits a gain compression, the predistortion linearizer is designed to have a gain expansion characteristic, and vice versa. The linearizer can be either shunt or series, active or passive. The simplest example of predistortion is a current mirror with an input current flowing through the diode-connected device. Other examples are shown in Fig. I.4. They were developed to linearize power amplifiers (PAs) with gain compression and positive phase deviation.

The series diode linearizer in Fig. I.4(a) [68]-[70] works as follows. With an increasing input power, the average dc current through the diode increases due to the rectification. As a result, the equivalent series resistance decreases, causing a gain expansion of the linearizer. In the shunt diode linearizer shown in Fig. I.4(b) [71]-[73], the rectified dc current through the diode also increases at higher input powers. But because the diode is biased through a resistor, the voltage across the diode decreases, increasing the equivalent shunt resistance and causing a gain expansion. If such a diode is placed in series with a base bias

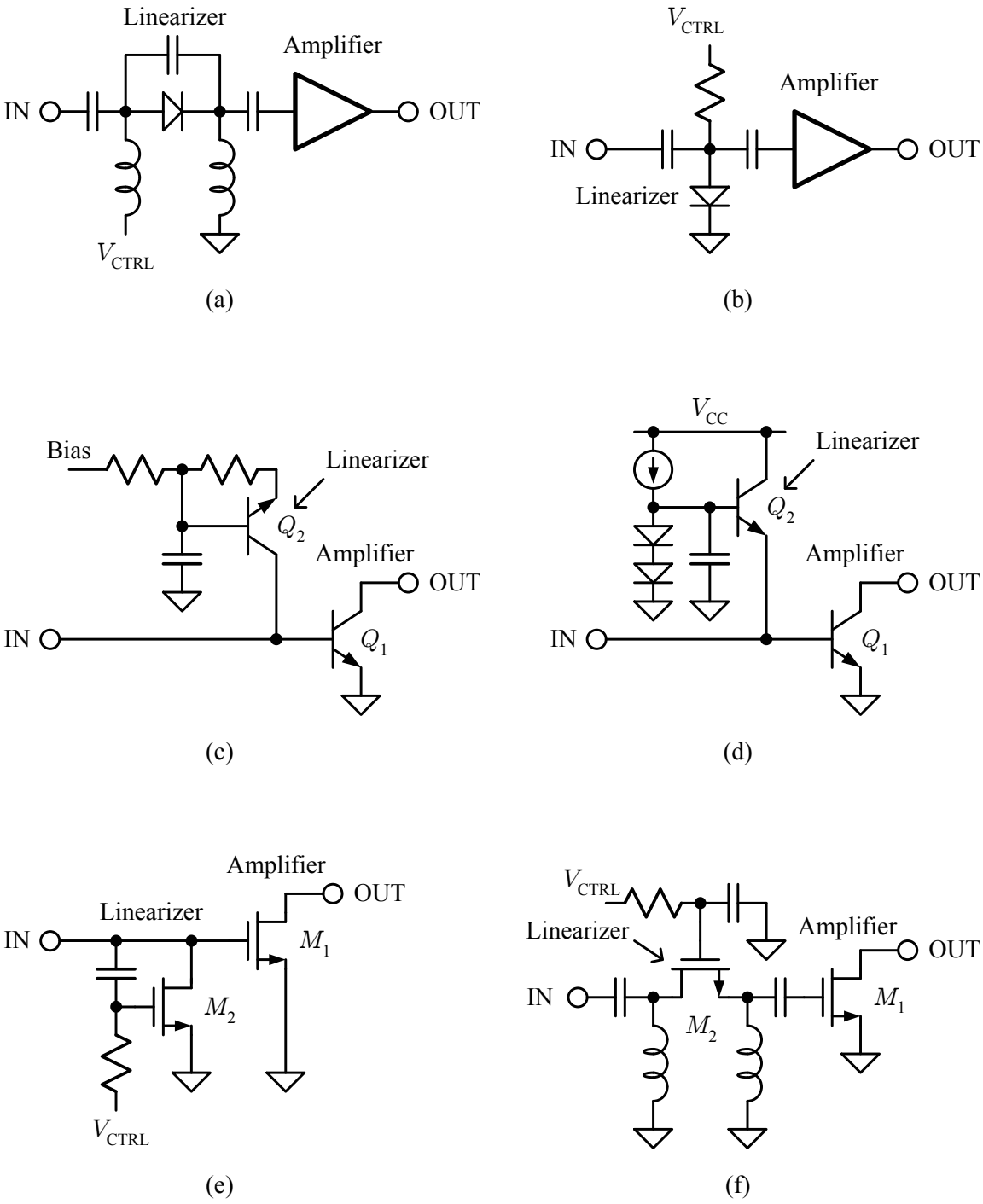

Figure I.4: Examples of predistortion. (a) Series diode [68]-[70]. (b) Shunt diode [71]-[73]. (c) Diode in a bias feed [74]-[77]. (d) Active bias [78]-[82]. (e) Shunt active FET [83]. (f) Series passive FET [84].

resistor of a BJT as shown in Fig. I.4(c), where the diode is implemented as the forward biased base-collector junction of Q_2 [74], then the reducing voltage across this diode raises the base dc bias of the main transistor at higher input powers, compensating for the gain compression of the latter. The linearizing diode in the input bias feed can also be implemented as a base-emitter junction of a BJT [75], [76], or a diode-connected FET [77]. The latter implementation is suitable for CMOS PAs. The linearizer in Fig. I.4(d) is based on the same principle, but uses an active bias [78]-[82]. The linearizer in Fig. I.4(e) [83] uses a shunt FET (M_2) biased near the threshold voltage, where the 3rd-order derivative of its transfer characteristic is negative. It generates an IMD_3 response in the input voltage of M_1, which cancels the IMD_3 response generated by the 3rd-order nonlinearity of M_1. Finally, the linearizer in Fig. I.4(f) uses a series FET switch, which acts as a variable resistor [84]. When biased near pinch-off, its resistance decreases with increasing input power, causing gain expansion. The shunt inductors are used for attaining a negative phase deviation.

The described predistortion examples use a linearizer to compensate for the nonlinearities in both the transconductance and input capacitance of an amplifying transistor. However, an input nonlinear capacitance can be compensated alone, as shown in Fig. I.5 [85]-[88].

The main challenge of the described method of the open-loop analog predistortion is to design a practical linearizer with the desired transfer function. Variations in the amplifier transfer function, caused by tolerances of the manufacturing process, require manual tuning of the linearizer from part to part, making this method costly and ill-suited for high-volume

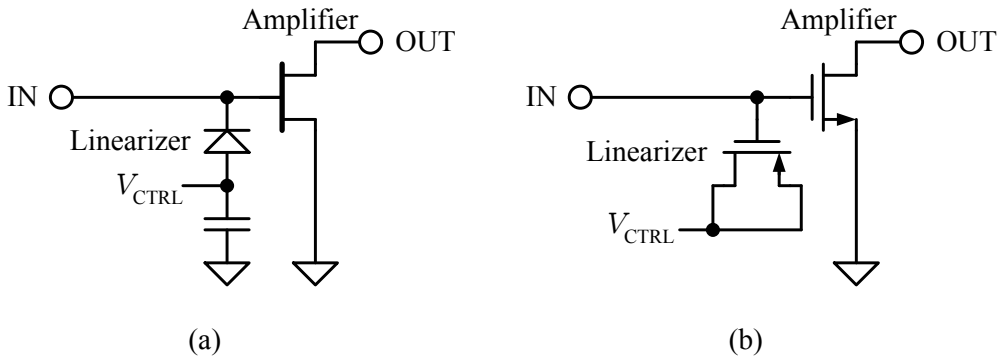

Figure I.5: Examples of compensation for a nonlinear input capacitance. (a) By a shunt diode [85]-[87]. (b) By a complementary FET [88].

production. An adaptive feedback is often added to overcome this drawback, but it makes the circuit rather complex.

Another challenge of the predistortion technique is dealing with multiple contributions to the overall IMD_3. Being a nonlinear circuit, a predistorter generates distortion responses of many orders. Among them, only a certain order is used for the cancellation of the overall IMD_3. The examples in Fig. I.4(a), (b), (e), and (f) rely on the IMD_3 responses of the predistorter. Their desired magnitude and phase are such that, after being linearly amplified by the main device, they cancel the IMD_3 responses generated by the main device. The examples in Fig. I.4(c) and (d) rely on the 2nd-order responses of the predistorter, and more specifically, on the difference-frequency response. For a single-tone excitation, this response is at dc and, thus, controls the input dc bias of the main device in the mentioned examples. This bias affects the gain of the main device through the 2nd-order nonlinearity of the latter. Therefore, the mentioned examples cancel the overall IMD_3 thanks to the interacting 2nd-order nonlinearities of the linearizer and the main device: the

linearizer generates the difference-frequency responses at the input of the main device, and, the 2nd-order nonlinearity of the latter mixes them with the fundamental responses, generating the correcting IMD_3 responses. However, besides the difference-frequency response, the linearizer also generates the 2nd-harmonic responses, which also contribute to the overall IMD_3 through the same mixing mechanism in the 2nd-order nonlinearity of the main device. The amplitude and phase of these 2nd-harmonic responses depend on the input termination at the corresponding frequencies. The linearizer also generates its own IMD_3 responses, which are linearly amplified by the main device, adding to the overall IMD_3. These responses depend on the input termination at the operating frequency. Therefore, in general, the overall IMD_3 response of an amplifier linearized by a predistorter includes contributions of 2nd and 3rd-order responses of both circuits. These contributions are complex quantities, whose vectors are generally not aligned because they are produced by different mechanisms and depend on different frequencies[6]. Therefore, for the predistortion method to achieve a high degree of the IMD_3 cancellation, both the in-band and out-of-band termination impedances of the amplifier must be optimally tuned. To avoid the necessity of tuning the out-of-band terminations, a linearizer with zero 2nd-order nonlinearity can be used. Such a linearizer has a symmetrical transfer characteristic around the bias point. It can be implemented as antiparallel diodes [90]-[93] or a passive FET (see Fig. I.4(f)).

Because of the difficulty to match the transfer function of a predistorter to that of an amplifier and because of the 2nd-order contribution to the overall IMD_3, the open-loop

[6]The Volterra series analysis showing how cascaded nonlinearities contribute to the overall 3rd-order transfer function and how these contributions define its frequency dependence can be found in [89] and [10].

predistortion method reduces distortion only by 3 to 6dB on average[7]. Series linearizers also exhibit a high insertion loss of 3 to 6dB in L-band and, thus, are not suitable for LNAs. Shunt linearizers have a typical insertion loss of 1 to 3dB in L-band, and, for the active bias, it can be as low as 0.4dB [78]. To the author's knowledge, the active bias is the only predistorter used in LNAs [81], [82].

I.3.5 Postdistortion

Postdistortion is similar to predistortion, but uses a linearizer after an amplifier. Its examples are shown in Fig. I.6. The first example is well known to analog designers: it uses an exponential current-to-voltage converter in the form of a diode-connected load. At very low frequencies, this load compensates for the transconductance nonlinearities of the input BJT, producing a linear voltage. The second example uses a reverse biased diode connected to the output of an HBT amplifier to compensate for the nonlinearity of its collector-base capacitance [94]. The third example uses an active postdistortion linearizer [95]. Its operation in the first-order, low-frequency approximation can be explained as follows. If the gate-source voltage of M_1 is undistorted and equal to v_{in}, the gate-source voltage of M_3 is also undistorted due to the postdistortion action of M_2 even though the current of M_1 is distorted. Neglecting the body effect, if M_1 and M_2 have the same dimensions, then $v_{\text{gs3}} = -v_{\text{in}}$, and the currents of M_1 and M_3 are

[7] The standouts are the shunt-diode and shunt-FET predistorters reported in [72] and [83], which improved IP_3 up to 6dB and 13.9dB, respectively. But with an insertion loss of around 2dB, these predistorters are not well suitable for CDMA LNAs.

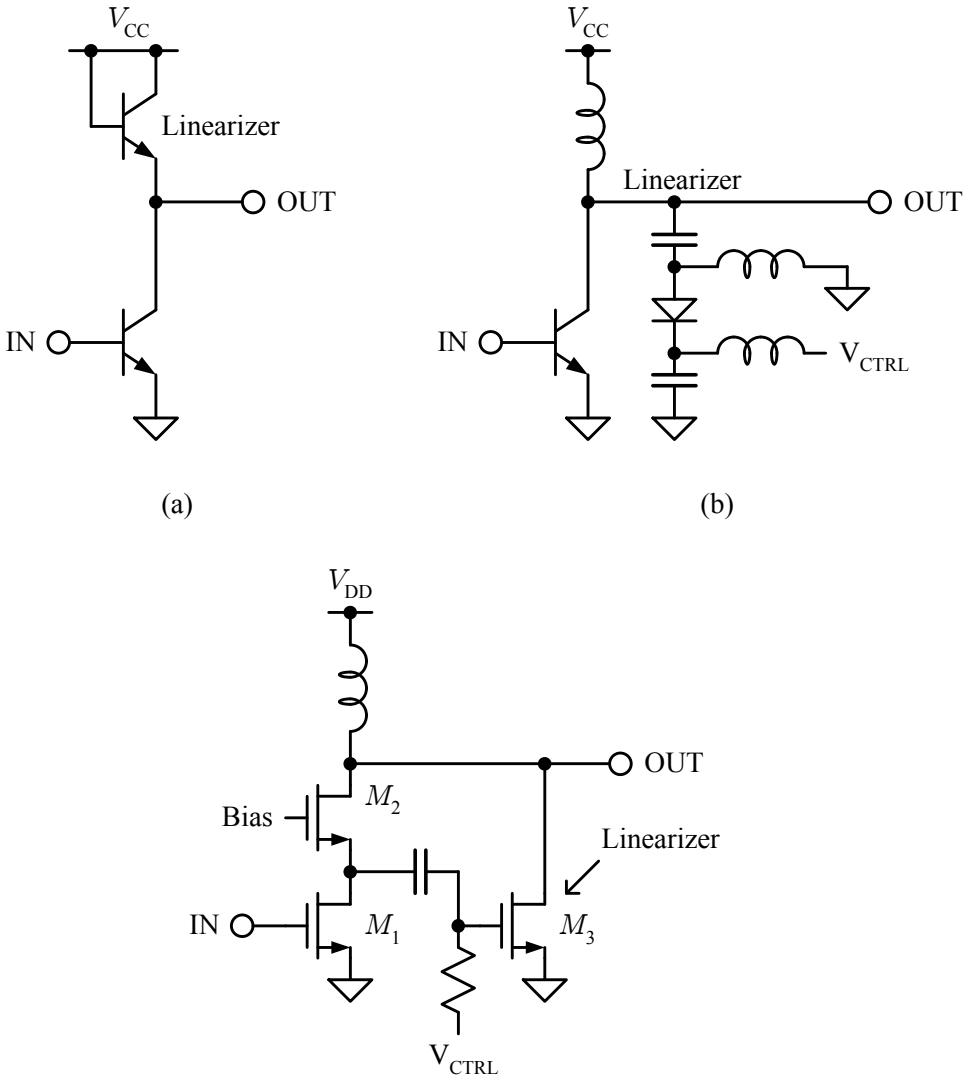

Figure I.6: Examples of postdistortion. (a) Active diode load. (b) Reverse-biased diode to compensate for C_{bc} nonlinearity [94]. (c) Active postdistortion [95].

$$i_1 = g_1 v_{\text{in}} + g_2 v_{\text{in}}^2 + g_3 v_{\text{in}}^3 + \cdots , \tag{I.13}$$

$$i_3 = -\sigma_1 v_{\text{in}} + \sigma_2 v_{\text{in}}^2 - \sigma_3 v_{\text{in}}^3 + \cdots . \tag{I.14}$$

Adding the two currents, we get

$$i_{\text{out}} = (g_1 - \sigma_1) v_{\text{in}} + (g_2 + \sigma_2) v_{\text{in}}^2 + (g_3 - \sigma_3) v_{\text{in}}^3 + \cdots . \tag{I.15}$$

Since the 3rd-order derivative of the FET transfer characteristic is nonmonotonic as a function of the gate-source voltage, it is possible to bias M_1 and M_3 such that $g_3 = \sigma_3$ and $\sigma_1 \ll g_1$. Then, the 3rd-order nonlinearity is cancelled without degrading the small-signal gain. Typically, to achieve this distortion cancellation, M_1 is biased in the strong inversion region, and M_3 is biased close to the threshold voltage. Because M_3 draws very little current, its contribution to NF is relatively small.

Postdistortion has not found a wide acceptance yet despite resolving the NF issue of the predistortion method. The main reason for the lack of popularity is that most linearization techniques have been developed for PAs, and the latter have a very large signal swing at the output, which makes it difficult to correct for the distortion. The other reason is that a postdistorter reduces the power added efficiency (PAE) - a critical parameter in the PA design. However, in LNAs, the output signal swing is relatively small, and PAE is not vital. Therefore, the postdistortion method deserves a wider attention.

I.3.6 Nonlinear Feedback

The nonlinear feedback method uses a linearizer in a feedback path of an amplifier. Examples are shown in Fig. I.7. The nonlinear emitter-degeneration circuit shown in Fig. I.7(a) [96] compensates for the gain expansion exhibited by Q_1 at small signal levels. With increasing input power, the dc component of the rectified current through the diode increases. Since all the dc current of the diode flows through $R_{\rm b}$, the voltage across the diode decreases, increasing the equivalent degeneration resistance and causing a gain compression. In Fig. I.7(b) [97], FET M_2 operates in the triode region and is used to compensate for the gain compression of M_1. As the input power increases, the current through M_2 becomes clipped from the lower side, and, thus, its dc component increases. Because all of the dc current of M_2 flows through M_1, the increased dc current of the latter causes a gain expansion. As a result, the 3rd-order distortion is reduced by 3-5dB at high power levels. The nonlinear shunt-shunt feedback in Fig. I.7(c) [76] is used to compensate for the gain compression of the main device. With increasing input power, the total dc current through the diode in the feedback path increases due to the rectification. The voltage drop across the diode is then decreases because of the resistor in series. As a result, the equivalent feedback resistance increases, causing a gain expansion. The linearity of the gain-compressing main FET M_1 in Fig. I.7(d) [98] is also improved thanks to an increase in the feedback resistance at higher signal powers. Larger voltage swings across the FET varistor M_2 move its operating point closer to saturation, increasing its average resistance. The linearization principle of the circuits shown in Fig. I.7(e) and (f) [99], [100] has not

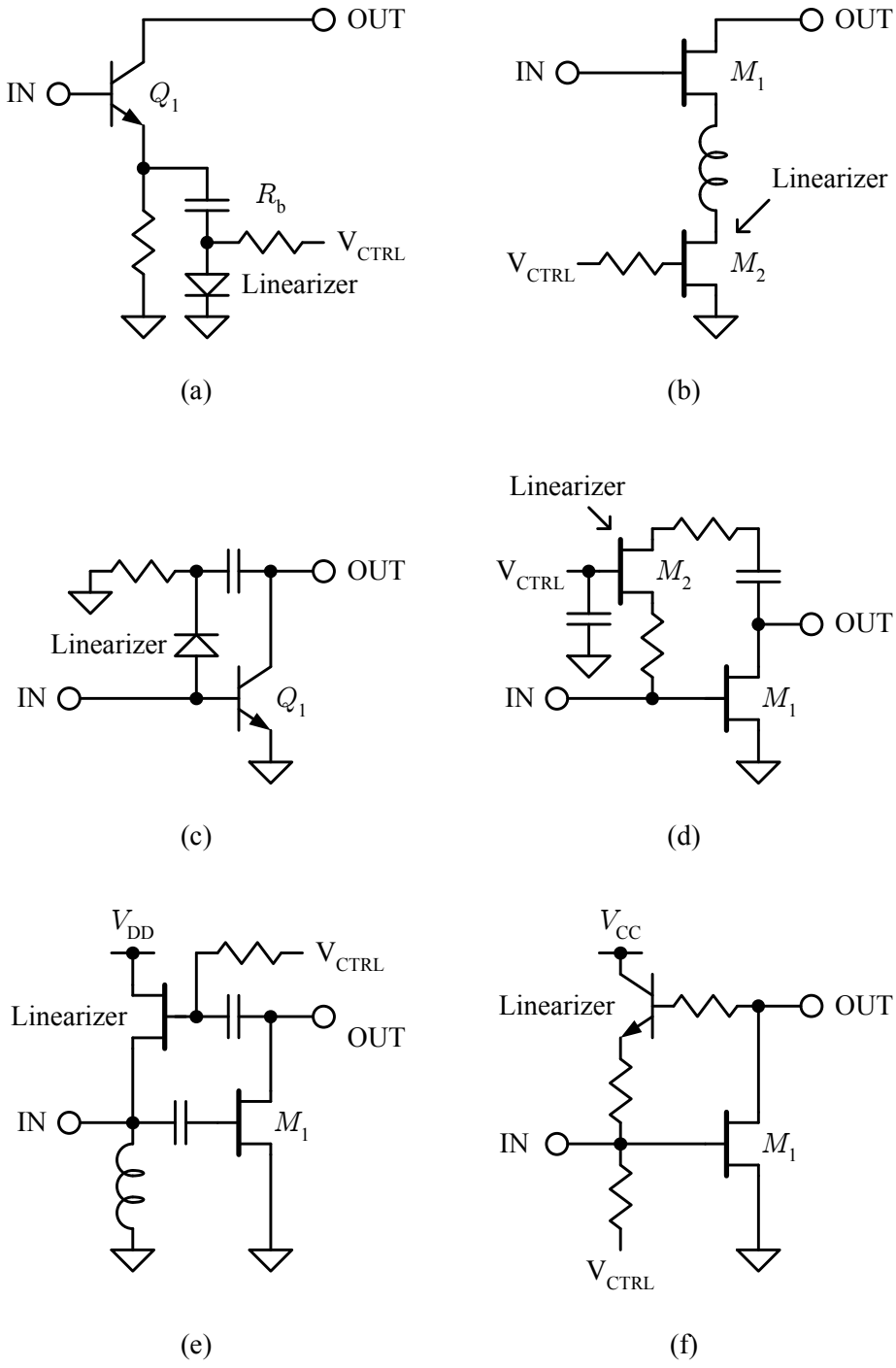

Figure I.7: Examples of nonlinear feedback. (a) Diode in an emitter-degeneration circuit [96]. (b) FET in a source-degeneration circuit [97]. (c) Diode in a parallel feedback [76]. (d) FET varistor in a parallel feedback [98]. (e), (f) Voltage follower in a parallel feedback [99], [100].

been well explained. To the author's opinion, the distortion is reduced thanks to the unilateral gain-compressing characteristics of the voltage follower in the parallel feedback path. The gain compression of this follower means a weaker negative feedback at higher power levels, which compensates for the gain compression of the main device M_1. The distortion is reduced by approximately 15dB, but at the expense of lower gain (6dB in [99] and 9dB in [100]) and higher NF (7dB in [99] and 3dB in [100]).

The theory of the nonlinear feedback can be described using the block diagram in Fig. I.2. If the transfer function of the feedback network is modeled by a power series with coefficients β_n's, and the transfer function of the open-loop amplifier is modeled by (I.3), then the 3rd-order coefficient of the closed-loop transfer function is [101]

$$c_3 = \frac{a_3}{(1+T)^4} - \frac{2a_2^2}{a_1}\frac{T}{(1+T)^5} - a_1^4\left[\frac{\beta_3}{(1+T)^4} - \frac{2\beta_2^2}{\beta_1}\frac{T}{(1+T)^5}\right] - \frac{4a_1^2 a_2\beta_2}{(1+T)^5}, \quad \text{(I.16)}$$

where $T = a_1\beta_1$. The first two terms in (I.16) are the same as in (I.6b) and describe the composite 3rd-order nonlinearity of the amplifier with a linear feedback. The third term represents the composite 3rd-order nonlinearity of the feedback network with a linear amplifier. Finally, the fourth term is created by interactions of the 2nd-order nonlinearities of the amplifier and the feedback network. Neglecting the 2nd-order interactions by making $a_2 = \beta_2 = 0$, we see that the 3rd-order nonlinearity of the open-loop amplifier is suppressed by a factor $(1+T)^4$ as before, but the 3rd-order nonlinearity of the feedback network is not suppressed at all. In fact, for a large loop gain ($T \gg 1$), this nonlinearity is amplified by a factor of $1/\beta_1^4$, where $\beta_1 < 1$, and, for a small loop gain ($T \ll 1$), it is amplified by a factor of a_1^4, where a_1 is the small-signal open-loop gain of the amplifier.

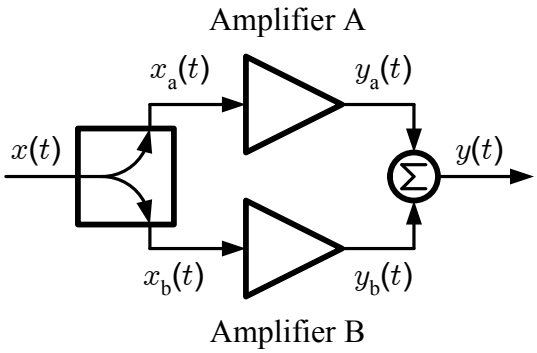

Figure I.8: Feedforward linearization technique.

If a nonlinear feedback is used to linearize an amplifier, its contribution to the overall distortion should be comparable to that of the amplifier, which means that the nonlinearities of the feedback network should be approximately a_1^4 times weaker than the nonlinearities of the amplifier. Because a_1 is typically very large, even small deviations in the nonlinearities of the feedback network will result in large variations of their contribution to the overall distortion, limiting the level of its suppression. For this reason, the nonlinear feedback method did not find a wide acceptance.

I.3.7 Feedforward

The feedforward technique was invented in 1924 by Harold S. Black in an attempt to linearize telephone repeaters [102]. Here we will deviate from the traditional feedforward linearization scheme, which uses couplers and delay lines, and will a simpler, more general scheme shown in Fig. I.8. This technique is based on splitting the input into two signals amplified by two amplifiers with different transfer characteristics such that, upon combining their output signals, their distortions cancel each other.

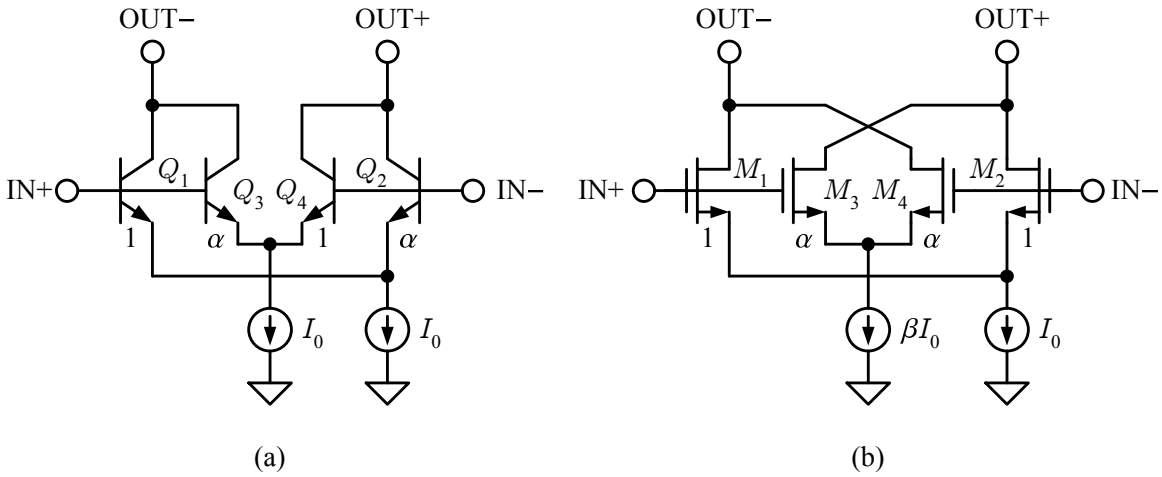

Figure I.9: Examples of feedforward linearization. (a) Multi-tanh doublet. (b) Cross-coupled CMOS differential pairs.

One of the well known implementations of this technique is the multi-tanh doublet shown in Fig. I.9(a) [103], [104]. It consists of two differential pairs connected in parallel, with BJTs in each one of them having different emitter widths. These widths are denoted by the scaling ratios 1 and α, where $\alpha < 1$. The combined differential output current can be modeled by the following power series in terms of the differential input voltage:

$$i_{\text{out}} = g_1 v_{\text{in}} + g_2 v_{\text{in}}^2 + g_3 v_{\text{in}}^3 + \cdots . \tag{I.17}$$

A simple analysis shows that the composite transconductance and the 3rd-order expansion coefficients are, respectively,

$$g_1 = \frac{I_0}{\phi_{\text{t}}} \frac{4\alpha}{(1+\alpha)^2}, \tag{I.18}$$

$$g_3 = \frac{I_0}{6\phi_{\text{t}}^3} \frac{4\alpha(\alpha^2 - 4\alpha + 1)}{(1+\alpha)^4}. \tag{I.19}$$

As can be seen, making $\alpha = 2 - \sqrt{3}$ results in zero g_3 and, thus, zero 3rd-order distortion. With this value of α, the composite transconductance is reduced by 1.5 times, or 3.52dB,

relative to the transconductance of a simple differential pair with the same total current. Though often used in low-frequency analog circuits, the multi-tanh method has not yet been used in RF LNAs (to the author's knowledge). Several publications have reported using it for WCDMA downconversion mixers [105], [106], but with IIP_3 of only -6...-3dBm. One of the reasons for such a poor linearity is the second-order interaction, whose contribution to IMD_3, being significant at RF, is not cancelled by this method.

An approach similar to the multi-tanh method has been adapted for CMOS differential pairs [107]-[110]. It is shown in Fig. I.9(b). The differential pair formed of M_1 and M_2 can be viewed as the main amplifier, whereas the pair formed of M_3 and M_4 is an auxiliary amplifier, whose purpose is to cancel IMD_3 of the main amplifier. Assuming the square-law characteristics of the FETs, the combined differential output current is given by

$$i_{\text{out}} = v_{\text{in}}\sqrt{KI_0}\sqrt{1-\frac{Kv_{\text{in}}^2}{4I_0}} - v_{\text{in}}\sqrt{\alpha K\beta I_0}\sqrt{1-\frac{\alpha K v_{\text{in}}^2}{4\beta I_0}}, \tag{I.20}$$

where v_{in} is the differential input voltage, K is the transconductance parameter of M_1 and M_2, and $\alpha < 1$ and $\beta < 1$ are the scaling ratios explained in Fig. I.9(b). The corresponding power series coefficients are

$$g_1 = \sqrt{KI_0}\left(1-\sqrt{\alpha\beta}\right), \tag{I.21}$$

$$g_3 = -\frac{1}{8}\sqrt{\frac{K^3}{I_0}}\left(1-\sqrt{\frac{\alpha^3}{\beta}}\right). \tag{I.22}$$

If β is designed to be equal to α^3, g_3 is zero, and the transconductance is degraded by $(1-\alpha^2)$. To reduce the gain degradation, α should be chosen as small as possible. For example, for $\alpha = 0.5$, the gain is degraded by 2.5dB.

An approach similar to the one shown in Fig. I.9(b) is used to linearize the differential CMOS LNA in [111]. In this LNA, both the tail current and the differential FETs of the auxiliary amplifier are scaled by the same ratio α. The input signal of the main amplifier is attenuated β times the input signal of the auxiliary amplifier. Using the block-diagram in Fig. I.8, with amplifier A being the main amplifier and amplifier B being the auxiliary amplifier, we can write their transfer functions as

$$y_{\mathrm{a}}(t) = a_1\beta x(t) + a_3(\beta x(t))^3, \tag{I.23}$$

$$y_{\mathrm{b}}(t) = \alpha[a_1 x(t) + a_3 x^3(t)], \tag{I.24}$$

where we have neglected the 2nd-order terms for simplicity. After subtracting $y_b(t)$ from $y_a(t)$, we get

$$y(t) = y_{\mathrm{a}}(t) - y_{\mathrm{b}}(t) = (\beta - \alpha)a_1 x(t) + (\beta^3 - \alpha)a_3 x^3(t). \tag{I.25}$$

If α is designed to be equal to β^3, the 3rd-order distortion is cancelled, and the fundamental signal is attenuated by $\beta(1-\beta^2)$. The choice of β is somewhat free. However, it is desirable to maximize the overall gain. In this case, the optimum value of β is $1/\sqrt{3}$ and the overall gain is reduced by $2\sqrt{3}/9$, or 8.3dB, relative to the gain of the main amplifier[8].

This implementation of the feedforward linearization technique suffers from several drawbacks. First, the overall gain of the composite amplifier is significantly degraded. The power gain reported in [111] is only 2.5dB. Second, NF is unacceptably high due to the fact that the noise powers of the two amplifiers add, while their desired signals subtract.

[8] Our treatment of this case is different from the one presented in [111], where the overall gain is unfairly calculated relative to the attenuated signal of the main stage (i.e., $\beta x(t)$), which gives a higher overall gain.

Third, splitting the signal with a well controlled attenuation value is technically challenging without using bulk coaxial assemblies. The presented analysis did not take into account the 2nd-order interaction, which also affects the match of the transfer functions and, thus, reduces the degree of distortion cancellation.

The reviewed feedforward linearization techniques are designed to work with differential amplifiers. The *derivative superposition* (DS) method proposed in [112] can be applied to single-ended amplifiers. It uses the fact that the 3rd-order derivative of the transfer characteristics of FETs and degenerated BJTs changes from positive to negative with an increasing input bias. The distortion cancellation is achieved by connecting two devices in parallel and biasing them in different regions of their transfer characteristics, in which the signs of the 3rd-order derivative are opposite. With the proper device scaling and biasing, the composite 3rd-order derivative can be made zero for an extended range of biases. Examples of the DS method are shown in Fig. I.10. The two FETs in Fig. I.10(a) have different input biases: one is biased in the strong inversion region, and the other is biased in the weak inversion (WI) region [112]-[115]. The latter FET has a negligible gain, but yet increases the overall input capacitance of the composite transistor, reducing the overall cut-off frequency and, thus, degrading the overall gain and NF. The gain and NF can be improved by replacing the FET biased in the WI region by a BJT, as shown in Fig. I.10(b) [116]. For the same amount of the transconductance nonlinearity, the dc current of a BJT is lower than that of a FET in the WI region, and its cut-off frequency is higher. To eliminate the need for the on-chip dc blocking capacitors, which occupy a large die area and typi-

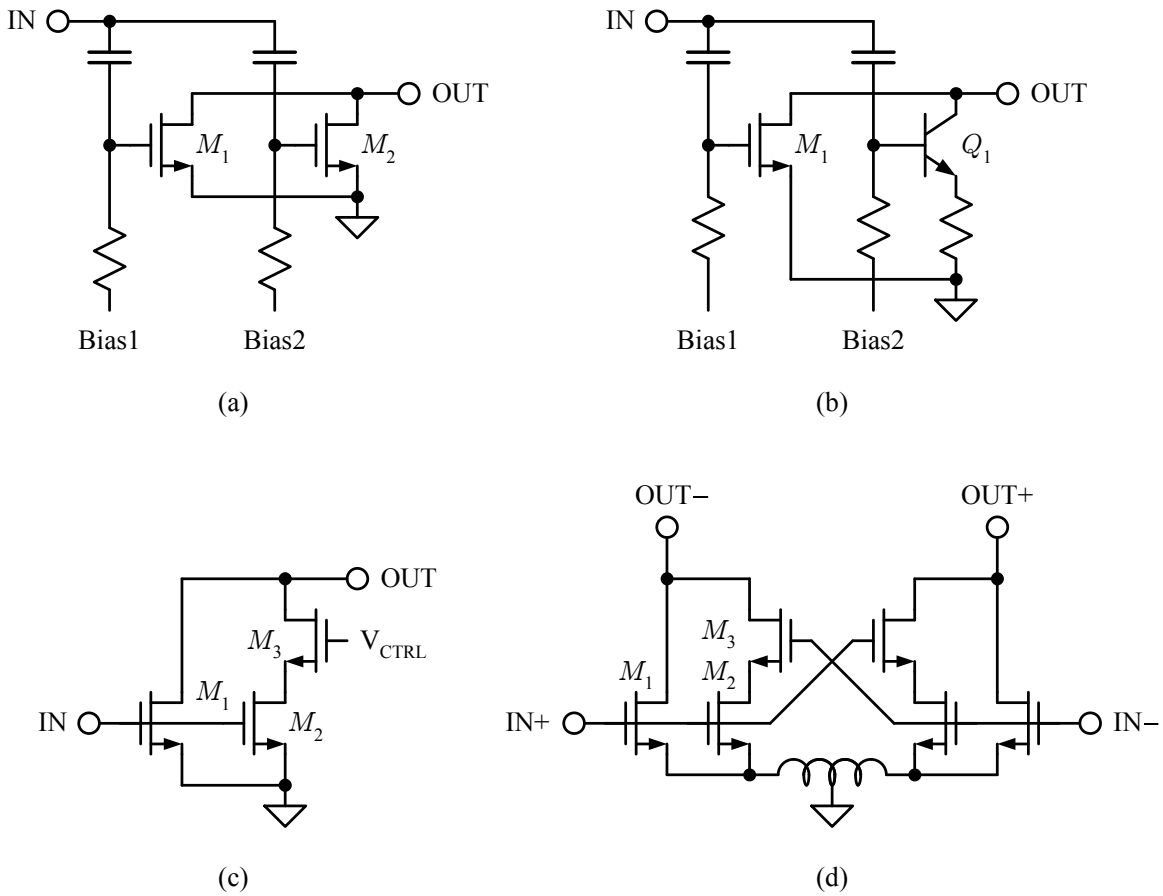

Figure I.10: Examples of DS method. (a) Conventional DS method using two parallel FETs in saturation [112]-[115]. (b) A FET in parallel with a degenerated BJT [116]. (c), (d) A FET in saturation connected in parallel with a FET in triode [117], [118].

cally degrade the LNA NF, the input FETs can be biased at the same gate-source voltage as shown in Fig. I.10(c) and (d) [117], [118]. In this case, different inversion levels and the resulting opposite signs of the 3rd-order derivatives are achieved by biasing the input FETs at different drain voltages. FET M_1 is biased in the saturation region, and FET M_2 is biased in the triode region thanks to M_3.

Besides the mentioned lower gain and higher NF, another significant drawback of the DS method is the effect of the 2nd-order interaction on IMD_3, which makes it difficult to

achieve a high degree of distortion cancellation.

I.4 Dissertation Focus

Recognizing the importance of modeling XMD in CDMA LNAs and the deficiencies of the existing treatments of a CDMA signal, we proposed a new, time-domain CDMA signal model, based on mathematical description of the reverse-link modulator [119]. Using this model, we derived a closed-form expression of XMD in a weakly-nonlinear circuit as a function of the signal properties and the circuit gain and IIP_3. For the first time in the technical literature, the "double-hump" XMD spectrum shape was correctly predicted by this expression and attributed to the statistical properties of the CDMA signal. The circuit in [119] was modeled by a Volterra series, which made the XMD analysis very complex and difficult to follow. However, its final result is very simple and could have been obtained using a power series model of the circuit, with the expansion coefficients expressed through the appropriate intercept points. This dissertation uses the CDMA signal model proposed in [119] and the power series method to derive an essentially the same XMD expression as in [119], but using only a few simple steps. The measured data is used to confirm the theoretical results. The derived XMD expression is then used to develop the linearity requirements of CDMA LNAs. These requirements in combination with other design goals, such as low NF, high gain, low dc current, and low-cost, high integration-level implementation, make the LNA design very challenging and suggest the use of linearization techniques. Among the latter, we considered the optimum out-of-band tuning, optimum gate biasing, and DS

method as the most promising, based on their ability to meet all the design goals.

The method of optimum out-of-band tuning has been previously implemented by optimizing either a difference-frequency or second-harmonic termination. As it is shown theoretically and experimentally in [120], both terminations must be optimized simultaneously to achieve the lowest distortion possible. The Volterra series analysis presented in [121] shows that simply reducing the bias circuit impedance to reduce IMD_3, as was proposed in [42]-[44], works only under certain restrictions on the BJT cut-off frequency, emitter degeneration impedance, and 2nd-harmonic input termination. This dissertation reviews the Volterra series theory of the optimum out-of-band tuning and the methods for generating the desired circuit terminations. It also shows that the low-frequency low-impedance input termination is a very robust linearization technique, but is only suitable for BJTs, not FETs. While BJTs have many advantages over FETs, including high cut-off frequency, high gain, and low NF, FETs are the only active devices available in CMOS technology, which offers a low cost - one of the key goals of the CDMA RX design.

Among the linearization techniques suitable for FET LNAs, the optimum gate biasing is the simplest. It is based on biasing a FET at the gate-source voltage at which the 3rd-order derivative of its dc transfer characteristic is zero. Such biasing causes an IMD_3 null. However, this null is very narrow and, thus, requires precise biasing at the mentioned voltage. A novel bias circuit is proposed in [122] to automatically generate this voltage in the presence of process and temperature variations. Its sensitivity to mismatches between FETs is analyzed. In addition to being narrow, the IMD_3 null is shown to shift at RF from

the bias voltage for zero 3rd-order derivative and become shallow, causing a lower IIP_3 peak. This behavior is theoretically attributed to the 2nd-order interaction, which becomes stronger at RF due to stronger parasitic feedbacks around a FET. This dissertation reviews the dc and RF theories of the optimum gate biasing and proposes an approach to reduce the degrading effect of the 2nd-order interaction on IIP_3 at RF. Even though this approach increases the IIP_3 peak, the latter remains shifted relative to the gate bias for zero 3rd-order derivative; thus, a manual bias adjustment is required, which makes IIP_3 very sensitive to the bias variations.

The DS method extends the bias voltage range in which a significant IIP_3 improvement is achieved. As a result, its sensitivity to the mentioned variations is reduced. However, as explained in [123], the 2nd-order interaction still degrades IIP_3 at RF. A modified DS method is proposed to improve IIP_3. In addition to high linearity, a low NF is another design goal for CDMA LNAs. In [123], an observation is made that the composite FET in both the conventional and modified DS methods exhibits a higher NF than that of a single FET. A possible theoretical explanation is given for this phenomenon. This dissertation reviews the dc and RF theories of the conventional DS method and, based on the Volterra series analysis, explains the principle of operation of the proposed modified DS method. We also give a detailed theoretical explanation of the higher NF of the composite FET in the DS method.

I.5 Dissertation Organization

The dissertation consists of seven chapters:

Chapter I is an introduction of cross modulation distortion in CDMA mobile RXs and methods to analyze and reduce it. An accurate XMD estimation is important for developing linearity requirements of CDMA LNAs. Deficiencies of existing CDMA signal models are addressed. Different approaches to meet these linearity requirements are reviewed.

Chapter II derives the time-domain model of a reverse-link CDMA signal, summarizes its statistical properties, and compares them to those of BPGN. The Volterra series approach in modeling the LNA nonlinear transfer function is compared to a much simpler power-series approach. A closed-form expression of XMD in a CDMA LNA is derived and compared to the measured results.

Chapter III derives the IIP_3 and NF requirements of CDMA LNAs, based on the RX sensitivity and single-tone desensitization requirements of the IS-95 standard. The closed-form expression of XMD, obtained in Chapter II, is used in these derivations.

Chapter IV explains the theory of the optimum out-of-band tuning technique based on the Volterra series analysis of a common-emitter circuit. An optimization routine of the difference-frequency and 2nd-harmonic terminations is described. A much simpler version of this linearization technique, using only the low-frequency low-impedance input termination, is investigated. Different methods for generating such a termination are reviewed. Two practical LNA examples are described to prove the theories.

Chapter V explains the dc theory of the optimum gate biasing, and describes the

novel bias circuit that automatically generates the optimum bias voltage. The effect of dc offsets on the bias circuit operation is analyzed. The effect of the 2nd-order interaction on IIP_3 at RF is also analyzed. An approach to increase the peak IIP_3 is proposed. A practical example of a CMOS LNA using this approach is described.

Chapter VI explains the theory and limitations of the conventional DS method. A modified DS method is proposed to improve the IIP_3 performance at RF. Its principle of operation is explained based on the Volterra series analysis. The NF performance of the composite FET in the DS method is analyzed by extending the van der Ziel noise theory to the subthreshold region. A practical example of a CMOS LNA using the modified DS method is described.

Chapter VII concludes the whole dissertation.

Chapter II

Analysis of Cross Modulation Distortion in Mobile CDMA Systems

II.1 Introduction

As was mentioned in the previous chapter, a mobile CDMA RX is a subject to interferences from offending base stations and from its own TX, whose signal leaks through the antenna duplexer to the LNA input. After passing through the LNA, a narrow-band jammer and the TX leakage become distorted. Particularly, the jammer spectrum widens due to XMD. This spectral splatter can contaminate the desired signal if the latter is received in the channel adjacent to the jammer. As a result, the RX sensitivity is degraded. The phone specification that deals with this contamination is the single-tone desensitization requirement. To determine whether an LNA passes this requirement, its XMD must be accurately estimated. Among different methods to quantify XMD, behavioral modeling is the simplest and fastest. But it requires accurate models for the CDMA signal and the LNA transfer function.

This chapter begins with a mathematical description of a CDMA reverse-link modulator, which yields a simple analytical model of an OQPSK signal. Based on this model, the

statistical properties of the reverse-link CDMA signal are derived and compared to those of BPGN. Then, the behavioral modeling issues of the LNA transfer function are discussed. The proposed OQPSK signal and LNA transfer function models in combination with statistical methods are then used to derive a closed-form expression of XMD as a function of the signal properties and the circuit gain and IIP_3. The theoretical results are compared to those derived using the Gaussian approximation and to the measured data.

II.2 Time-Domain Model of Reverse-Link CDMA Signal and Its Statistical Properties

A CDMA reverse-link modulator uses OQPSK spreading. Its block-diagram is shown in Fig. II.1. A ± 1-valued data stream is first split into the I and Q branches of the modulator and multiplied by orthogonal pseudo-noise (PN) codes with the chip rate $R = 1.2288$M chips/sec. The codes are assumed infinitely long. The Q sequence is delayed by half a PN chip time. Each sequence is then multiplied by the baseband filter impulse response resulting in the following baseband signals:

$$I(t) = \sum_{k=-\infty}^{\infty} i_k h(t + (\phi/\pi - k)T), \tag{II.1a}$$

$$Q(t) = \sum_{k=-\infty}^{\infty} q_k h(t + (\phi/\pi - k + 1/2)T), \tag{II.1b}$$

where i_k and q_k are uncorrelated random numbers taking values of ± 1 with equal probability, $h(t)$ is the baseband filter impulse response, ϕ is a random phase uniformly distributed

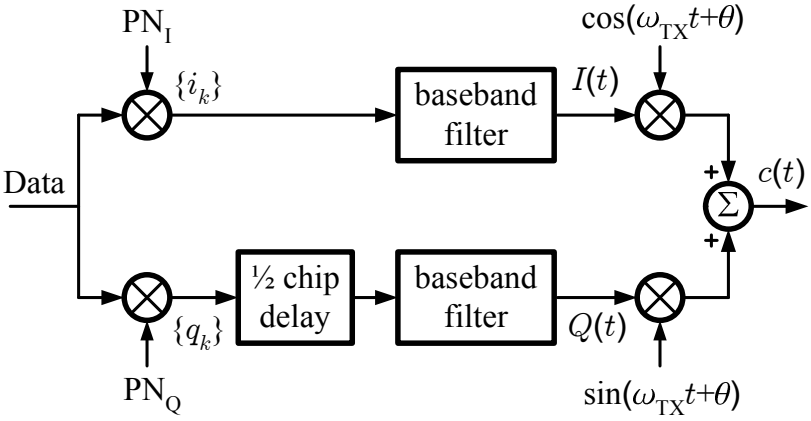

Figure II.1: CDMA reverse-link modulator.

in $(0, 2\pi)$, and T is the chip time equal to $1/R$.

The IS-95 baseband filter is implemented as a 48-tap finite impulse response filter. With an acceptable accuracy, it can be modeled as an ideal low-pass filter with the cutoff frequency of $b/2$ and infinite impulse response $h(t) = \mathrm{sinc}(bt)$, where $\mathrm{sinc}(z) = \sin(\pi z)/(\pi z)$ and $b = 1/T = 1.2288$MHz. The impulse and frequency responses of this brick-wall filter are compared to the IS-95 filter responses in Fig. II.2. With this approximation, the filtered I and Q signals are given by

$$I(t) = \sum_{k=-\infty}^{\infty} i_k \,\mathrm{sinc}(bt + \phi/\pi - k), \tag{II.2a}$$

$$Q(t) = \sum_{k=-\infty}^{\infty} q_k \,\mathrm{sinc}(bt + \phi/\pi - k + 1/2). \tag{II.2b}$$

After the baseband pulse-shaping, the I and Q signals are modulated on two carriers in quadrature and summed, producing an OQPSK signal:

$$c(t) = I(t)\cos(\omega_{\mathrm{TX}}t + \theta) + Q(t)\sin(\omega_{\mathrm{TX}}t + \theta), \tag{II.3}$$

where ω_{TX} is the angular frequency of the carriers and θ is their random phase indepen-

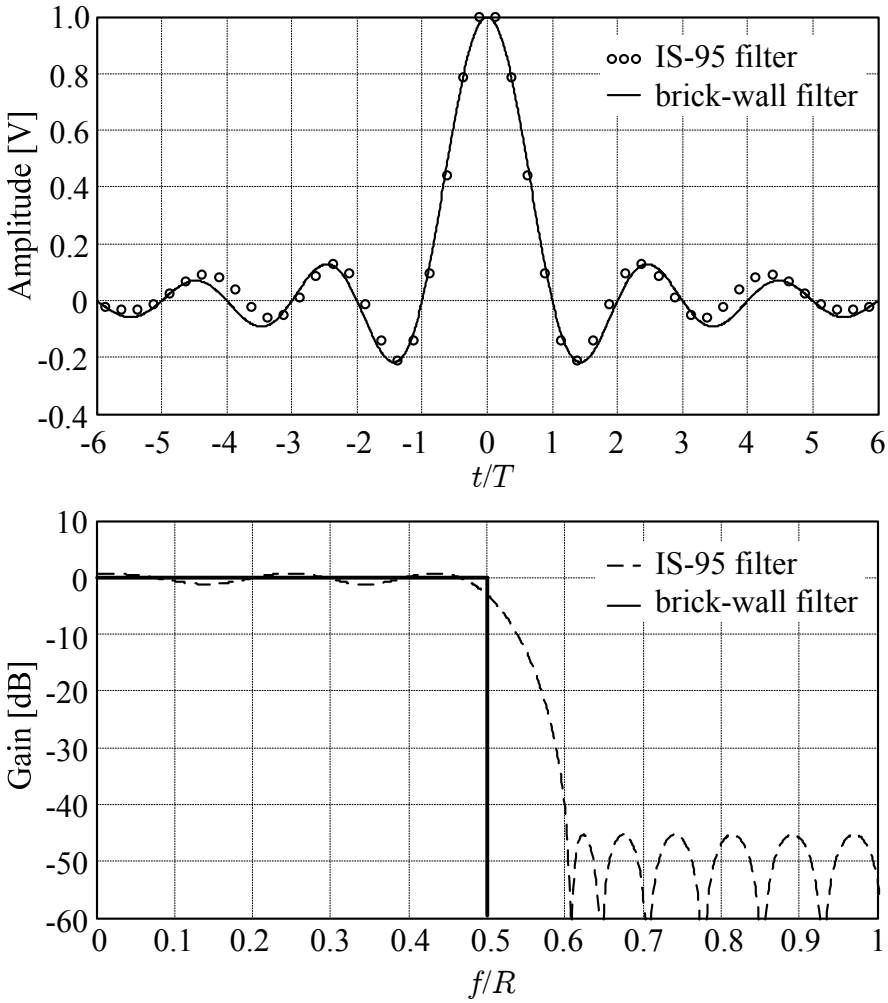

Figure II.2: Impulse and frequency responses of the IS-95 and brick-wall filters.

dent of ϕ and uniformly distributed in $(0, 2\pi)$. Equations (II.2a)-(II.3) constitute the time-domain model of an OQPSK signal with unity variance.

For a distortion analysis using statistical methods, it is important to know the moments of i_k and q_k in (II.2a) and (II.2b). The following 1st and 2nd-order moments do not need an explanation:

$$E\{i_k\} = E\{q_k\} = 0, \tag{II.4a}$$

$$E\{i_k q_l\} = E\{i_k\}E\{q_l\} = 0, \tag{II.4b}$$

$$E\{i_k i_l\} = E\{q_k q_l\} = \delta_{kl} = \begin{cases} 1, & \text{if } k = l \\ 0, & \text{otherwise} \end{cases}, \tag{II.4c}$$

where $E\{\}$ is the statistical average (or expectation) operator and δ_{kl} is the Kronecker delta. We will also need the following 4th-order moments [124]:

$$E\{i_k i_l i_m i_n\} = E\{q_k q_l q_m q_n\} = \delta_{kl}\delta_{mn} + \delta_{km}\delta_{ln} + \delta_{kn}\delta_{lm} - 2\delta_{kl}\delta_{km}\delta_{kn}, \tag{II.5a}$$

$$E\{i_k i_l q_m q_n\} = E\{i_k i_l\}E\{q_m q_n\} = \delta_{kl}\delta_{mn}. \tag{II.5b}$$

The first three terms on the right side of (II.5a) reflect three occurrences of the case with two pairs of equal indexes, which yields $E\{i_k i_l i_m i_n\} = E\{q_k q_l q_m q_n\} = 1$. These terms also count the case $k = l = m = n$ three times, yielding 3. However, $E\{i_k^4\} = E\{q_k^4\} = 1$; therefore, the correction term $-2\delta_{kl}\delta_{km}\delta_{kn}$ in (II.5a) had to be applied.

II.3 Comparison of CDMA Signal with BPGN

According to the interpolation formula of the sampling theorem [125], any signal confined to the band $(-b/2, b/2)$ can be accurately represented by an infinite sum of the sinc pulses spaced periodically $1/b$ sec apart and weighted by the signal samples at the corresponding time instants. So, equations (II.2a)-(II.3) can be viewed as a general time-domain model of two band-limited signals modulated in quadrature on a carrier, with i_k and q_k being their samples. If these samples are normally distributed, (II.2a)-(II.3) describe BPGN. So, the important difference between a CDMA signal and BPGN is in the statistical properties of their baseband samples i_k and q_k. Some of these properties are compared in Table II.1. As can be seen from this table, the 1st and 2nd-order moments of the baseband samples are the same for these signals, whereas the 4th order moments are different. This difference is also expected for higher order moments.

Table II.1: Moments of the baseband samples of a CDMA signal and BPGN.

Moment	OQPSK	BPGN
$E\{i_k^n\}, E\{q_k^n\}$	$0, \quad n$ is odd $1, \quad n$ is even	$0, \quad n$ is odd $\frac{n!}{(n/2)!2^{n/2}}, \quad n$ is even
$E\{i_k i_l\}, E\{q_k q_l\}$	δ_{kl}	δ_{kl}
$E\{i_k q_l\}$	0	0
$E\{i_k i_l i_m i_n\}$, $E\{q_k q_l q_m q_n\}$	$\delta_{kl}\delta_{mn} + \delta_{km}\delta_{ln} + \delta_{kn}\delta_{lm}$ $-2\delta_{kl}\delta_{km}\delta_{kn}$	$\delta_{kl}\delta_{mn} + \delta_{km}\delta_{ln} + \delta_{kn}\delta_{lm}$
$E\{i_k i_l q_m q_n\}$	$\delta_{kl}\delta_{mn}$	$\delta_{kl}\delta_{mn}$
All odd-order	0	0

Let us also compare the power spectral density (PSD) functions of the above sig-

nals. First, we need to derive the autocorrelation function. As shown in Appendix A, this function uses the correlation properties of i_q and q_k, which are the same for the considered signals, and, therefore, they have the same autocorrelation given by

$$R_c(\tau) = \mathrm{sinc}(b\tau)\cos(\omega_{\mathrm{TX}}\tau). \tag{II.6}$$

Applying the Fourier transform to (II.6) and using the *Wiener-Khinchin* theorem [11], we get the following PSD of an OQPSK signal and BPGN:

$$S_c(\omega) = \int_{-\infty}^{+\infty} R_c(\tau)e^{-j\omega\tau}d\tau = \begin{cases} 1/(2b), & ||\omega| - \omega_{\mathrm{TX}}| \leq \pi b \\ 0, & \text{otherwise.} \end{cases} \tag{II.7}$$

So, despite different statistical properties of the baseband samples, a reverse-link CDMA signal and BPGN spectrally look the same.

II.4 LNA Behavioral Modeling

A power series is the simplest way to describe a transfer function of a nonlinear circuit. It is well suited for low-frequency, memoryless circuits. However, a CDMA LNA operates at RF; therefore, its reactances can not be neglected. In this case, a Volterra series is more appropriate. This section will show that a power series can still be used to account for the reactances of an RF circuit as long as the series coefficients are expressed through the appropriate measures of the circuit nonlinearity.

Let the transfer function of the LNA in Fig. I.1 be expanded into the following

Volterra series:

$$y(t) = C_1(s) \circ x(t) + C_2(s_1, s_2) \circ x^2(t) + C_3(s_1, s_2, s_3) \circ x^3(t) + \cdots , \tag{II.8}$$

where $C_n(s_1, s_2, \cdots , s_n)$ is the Laplace transform of the nth-order Volterra kernel, also often called as the nth-order nonlinear transfer function, $s = j\omega$ is the Laplace variable, and the operator "$\circ$" means that the magnitude and phase of each spectral component of $x^n(t)$ is to be changed by the magnitude and phase of $C_n(s_1, s_2, \cdots , s_n)$, where the frequency of the component is $\omega_1 + \omega_2 + \cdots + \omega_n$ [15].

Let the input signal of the LNA consist of a continuous-wave (CW) jammer $A_\mathrm{j} \cos(\omega_\mathrm{j} t)$ and a TX leakage, modeled by (II.3) with the deterministic baseband signals $I(t) = Q(t) = \cos(\Delta\omega t/2)$, i.e.,

$$x(t) = A_\mathrm{j} \cos(\omega_\mathrm{j} t) + A_\mathrm{TX} \cos(\Delta\omega t/2) \left[\cos(\omega_\mathrm{TX} t) + \sin(\omega_\mathrm{TX} t)\right] , \tag{II.9}$$

where θ was set to 0 for simplicity. Trigonometric manipulations show that $x(t)$ contains three spectral components: ω_j, $\omega_\mathrm{TX} - \Delta\omega/2$, and $\omega_\mathrm{TX} + \Delta\omega/2$. The first one has the amplitude of A_j, and the latter two have the amplitude of $A_\mathrm{TX}/\sqrt{2}$. Let us denote the frequencies of these spectral components as ω_1, ω_2, and ω_3, respectively. Substituting (II.9) into (II.8) and neglecting the nonlinear terms of the order higher than three, we will find that the LNA output contains the following spectral components among others:

$$\begin{aligned}
&|C_1(s_1)|\, A_\mathrm{j} \cos\left[\omega_\mathrm{j} t + \angle C_1(s_1)\right] \\
&+ \frac{3}{4} |C_3(s_1, s_2, -s_3)|\, A_\mathrm{j} A_\mathrm{TX}^2 \cos\left[(\omega_\mathrm{j} - \Delta\omega)t + \angle C_3(s_1, s_2, -s_3)\right] \\
&+ \frac{3}{4} |C_3(s_1, -s_2, s_3)|\, A_\mathrm{j} A_\mathrm{TX}^2 \cos\left[(\omega_\mathrm{j} + \Delta\omega)t + \angle C_3(s_1, -s_2, s_3)\right] .
\end{aligned} \tag{II.10}$$

They describe the amplified jammer with two sidebands representing XMD. We are interested in the amplitudes of these sidebands. They depend on the input signal strengths as well as the magnitudes of the corresponding 3rd-order nonlinear transfer functions. The purpose of the behavioral modeling is to relate these transfer functions to widely-used measures of nonlinearity. Since, in this particular case, the input signal consists of three single tones, the nonlinear transfer functions defining XMD can be found from the *triple-beat distortion factor* (TB).

If a circuit is driven by three tones at ω_1, ω_2, and ω_3, with the amplitudes of A_1, A_2, and A_3, respectively, its output contains the following spectral components, which are similar to (II.10):

$$\begin{aligned}
&|C_1(s_1)|\, A_1 \cos\left[\omega_1 t + \angle C_1(s_1)\right] \\
&+ \frac{3}{2} |C_3(s_1, s_2, -s_3)|\, A_1 A_2 A_3 \cos\left[(\omega_1 + \omega_2 - \omega_3)t + \angle C_3(s_1, s_2, -s_3)\right] \\
&+ \frac{3}{2} |C_3(s_1, -s_2, s_3)|\, A_1 A_2 A_3 \cos\left[(\omega_1 - \omega_2 + \omega_3)t + \angle C_3(s_1, -s_2, s_3)\right]. \qquad \text{(II.11)}
\end{aligned}$$

TB is measured as the ratio of the amplitude of one of the sidebands around ω_1 to the amplitude of the response at ω_1:

$$\mathrm{TB} = \frac{3}{2} \left| \frac{C_3(s_1, -s_2, s_3)}{C_1(s_1)} \right| A_2 A_3. \qquad \text{(II.12)}$$

In the TB definition, the three tones have an equal amplitude. However, after taking the ratio, one of the amplitudes cancels out; therefore, only the remaining two have to be equal (A_2 and A_3 in our example). As in the case of IIP_3, used to characterize IMD_3, we can introduce the triple-beat intercept point (TBIP), defined as the power of the tones at ω_2 and

ω_3 at which TB=1. Substituting TB=1 and $A_2 = A_3 = A$ into (II.12), we can find:

$$A_{\mathrm{TBIP}} = \sqrt{\frac{2}{3}\left|\frac{C_1(s_1)}{C_3(s_1,-s_2,s_3)}\right|}, \tag{II.13}$$

and

$$\mathrm{TBIP} = \frac{A_{\mathrm{TBIP}}^2}{2} = \frac{1}{3}\left|\frac{C_1(s_1)}{C_3(s_1,-s_2,s_3)}\right|. \tag{II.14}$$

The advantage of using TBIP instead of TB is that the former is independent on the signal strength. It can be measured by varying the power of all three tones simultaneously or by varying the power of just the ω_2 and ω_3 tones. The latter approach results in 2:1dB slope of the triple-beat distortion power versus the input power of the mentioned tones.

From (II.14), we can easily derive the nonlinear transfer function that controls XMD:

$$|C_3(s_1,-s_2,s_3)| = \frac{|C_1(s_1)|}{3\mathrm{TBIP}}. \tag{II.15}$$

The quantity $|C_1(s_1)|$ is simply the square root of the circuit power gain at ω_1. Therefore, to find the 3rd-order nonlinear transfer function that defines XMD, we can use a triple-beat test in which one of the tones is at the jammer frequency, and the other two tones of equal amplitude are within the bandwidth of the TX leakage as shown in Fig. II.3.

Though TB or TBIP are the most suitable measures of the LNA nonlinearity that generates XMD, they are not as widely used in LNA specifications as IIP_3. To see how the 3rd-order transfer function can be expressed through IIP_3, we will substitute the following two-tone input into (II.8):

$$x(t) = A_1\cos(\omega_1 t) + A_2\cos(\omega_2 t). \tag{II.16}$$

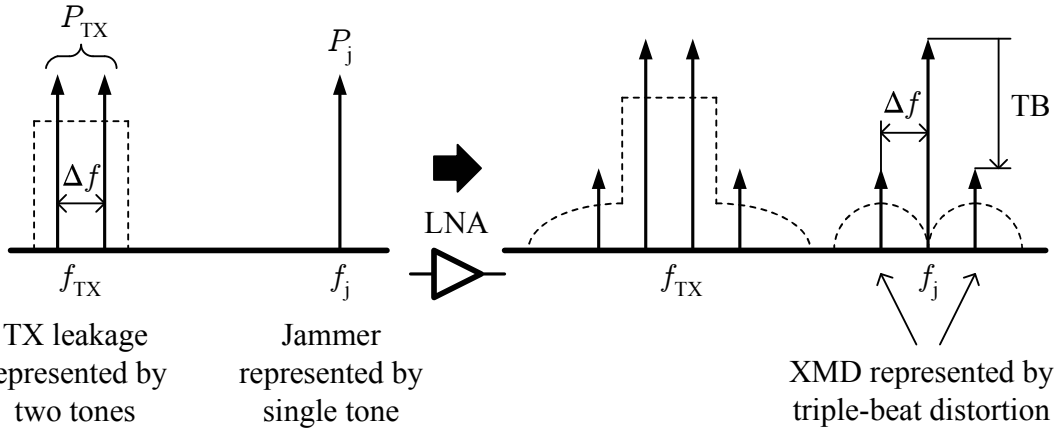

Figure II.3: Triple-beat test to probe for the LNA nonlinear transfer function that controls XMD.

We will find that the LNA output contains the following spectral components among others:

$$\begin{aligned}
&|C_1(s_1)|\, A_1 \cos\left[\omega_1 t + \angle C_1(s_1)\right] + |C_1(s_2)|\, A_2 \cos\left[\omega_2 t + \angle C_1(s_2)\right] \\
&+ \frac{3}{4} |C_3(s_1, s_1, -s_2)|\, A_1^2 A_2 \cos\left[(2\omega_1 - \omega_2)t + \angle C_3(s_1, s_1, -s_2)\right] \\
&+ \frac{3}{4} |C_3(s_2, s_2, -s_1)|\, A_2^2 A_1 \cos\left[(2\omega_2 - \omega_1)t + \angle C_3(s_2, s_2, -s_1)\right]. \qquad \text{(II.17)}
\end{aligned}$$

The $(2\omega_1 - \omega_2)$ and $(2\omega_2 - \omega_1)$ spectral components represent IMD_3. The 3rd-order intermodulation ratio (IM_3) is defined as

$$\text{IM}_3 = \frac{3}{4} \left| \frac{C_3(s_1, s_1, -s_2)}{C_1(s_2)} \right| A_2^2. \qquad \text{(II.18)}$$

With the two input tones having equal amplitude ($A_1 = A_2 = A$), IIP_3 is defined as the power of each tone at which IM_3=1. Substituting IM_3=1 into (II.18), we can find:

$$A_{\text{IP3}} = \sqrt{\frac{4}{3} \left| \frac{C_1(s_1)}{C_3(s_2, s_2, -s_1)} \right|}, \qquad \text{(II.19)}$$

and

$$\text{IIP}_3 = \frac{A_{\text{IP3}}^2}{2} = \frac{2}{3} \left| \frac{C_1(s_1)}{C_3(s_2, s_2, -s_1)} \right|. \qquad \text{(II.20)}$$

From (II.20), we can easily derive the transfer function that controls IMD_3:

$$|C_3(s_2, s_2, -s_1)| = \frac{2\,|C_1(s_1)|}{3\text{IIP}_3}. \tag{II.21}$$

It is important to understand the differences between $C_3(s_2, s_2, -s_1)$ in (II.21) and $C_3(s_1, -s_2, s_3)$ in (II.15). These functions determine a distortion response appearing at the frequency equal to the sum of their arguments. They themselves depend on the circuit impedances at frequencies equal to their arguments and their possible linear combinations. In a triple-beat test with $f_1 = f_\text{j}$, $f_2 = f_\text{TX} - \Delta f/2$, and $f_3 = f_\text{TX} + \Delta f/2$, the frequency of the distortion response controlled by $C_3(s_1, -s_2, s_3)$ is $f_\text{j} + \Delta f$. Assuming that $\Delta f \ll f_\text{j} - f_\text{TX}$, the frequencies on which $C_3(s_1, -s_2, s_3)$ depends are Δf, $f_\text{j} - f_\text{TX}$, f_TX, f_j, and $f_\text{j} + f_\text{TX}$. In an IMD_3 test with $\Delta f = f_2 - f_1$ and $f_1 \approx f_2 \approx f_\text{j}$, the frequency of the distortion response controlled by $C_3(s_2, s_2, -s_1)$ is $f_\text{j} + \Delta f$, i.e., the same as in the triple-beat test. Assuming that $\Delta f \ll f_\text{j}$, the frequencies controlling $C_3(s_2, s_2, -s_1)$ are Δf, f_j, and $2f_\text{j}$. They are different from those controlling $C_3(s_1, -s_2, s_3)$ in the triple-beat test. Therefore, these transfer functions are in general different except when the circuit impedances are the same at the following pairs of frequencies: Δf and $f_\text{j} - f_\text{TX}$, f_TX and f_j, $f_\text{j} + f_\text{TX}$ and $2f_\text{j}$. In the rest of this chapter, we will assume that the mentioned transfer functions are the same and will use IIP_3 as their measure.

At the beginning of this section, we chose the Volterra series model of the LNA output to show how the excitation frequencies and their linear combinations affect the 3rd-order transfer function controlling a particular distortion response. Because the frequency of this response is known ahead of time, we can express $C_3(s_1, s_2, s_3)$ in (II.8) through the

appropriate intercept point (TBIP or IIP_3) and replace "$\circ$" with multiplication. The linear transfer function $C_1(s)$ can be expressed through the circuit gain at the frequency of the tone to which the distortion response is compared. If other terms of the series are neglected, it would look like a power series with the 1st and 3rd-order coefficients expressed through the circuit gain and intercept point, respectively. Such a power series can accurately capture the effect of the circuit reactances on the particular distortion response.

II.5 Derivation of XMD Spectral Density

Let the input signal of the LNA in Fig. I.1 be

$$x(t) = A_{\mathrm{j}} \cos(\omega_{\mathrm{j}} t + \psi) + A_{\mathrm{TX,rms}} c(t), \tag{II.22}$$

where the first term describes a CW jammer with a constant amplitude A_{j} and a random phase ψ, uniformly distributed over the interval $(0, 2\pi)$, and the second term describes a TX leakage with the root-mean-square amplitude $A_{\mathrm{TX,rms}}$.

The LNA output can be modeled by the following truncated power series

$$y(t) = c_1 x(t) + c_3 x^3(t), \tag{II.23}$$

where we have neglected the 2nd-order term because it does not contribute to XMD. The nonlinear terms of the order higher than three were also neglected because most RX circuits operate well below their 1dB gain compression points. Such circuits exhibit so-called *weakly nonlinear* behavior. We have chosen the power series model of the LNA output

based on its equivalence to the Volterra series model, provided that c_3 will be later expressed through IIP_3 as explained in the previous section.

Substituting (II.3) into (II.22) and the latter into (II.23), we get multiple spectral components, among which we are interested in the following one

$$y_{\text{XMD}}(t) = \frac{3}{2} c_3 A_{\text{j}} A_{\text{TX,rms}}^2 \left[I^2(t) + Q^2(t) \right] \cos(\omega_{\text{j}} t + \psi). \tag{II.24}$$

This component represents the jammer modulated by the sum of the squared baseband signals used for the TX signal modulation. Therefore, at the LNA output, the modulation of the TX leakage is transferred to the jammer, which is the essence of XMD. Because the modulation signals in (II.24) are squared, the bandwidth of XMD is twice the bandwidth of the TX leakage. This XMD contaminates the desired signal if it is received in the channel adjacent to the jammer. The total power of the portion of XMD that falls into the desired signal band has to be quantified in order to determine the LNA IIP_3 requirement. This goal can be achieved by knowing the PSD of XMD.

The first step is to find the autocorrelation function of $y_{\text{XMD}}(t)$:

$$\begin{aligned} R_{\text{XMD}}(\tau) &= E\{y_{\text{XMD}}(0) y_{\text{XMD}}(\tau)\} \\ &= \frac{9}{4} c_3^2 P_{\text{j}} P_{\text{TX}}^2 \cos(\omega_{\text{j}} \tau) \\ &\quad \cdot E\left\{ I^2(0) I^2(\tau) + Q^2(0) Q^2(\tau) + I^2(0) Q^2(\tau) + I^2(\tau) Q^2(0) \right\}, \end{aligned} \tag{II.25}$$

where $P_{\text{j}} = A_{\text{j}}^2/2$ and $P_{\text{TX}} = A_{\text{TX,rms}}^2$ are the jammer and TX leakage input powers, respectively.

The 3rd-order expansion coefficient c_3 can be expressed through IIP_3 using (II.21).

We get

$$c_3^2 = \frac{4G}{9 \cdot \mathrm{IIP}_3^2}, \tag{II.26}$$

where G is the power gain of the circuit equal to c_1^2. Substitution of (II.26) into (II.25) gives

$$R_{\mathrm{XMD}}(\tau) = \frac{G P_{\mathrm{j}} P_{\mathrm{TX}}^2}{\mathrm{IIP}_3^2} \cos(\omega_{\mathrm{j}} \tau) \cdot E\left\{I^2(0)I^2(\tau) + Q^2(0)Q^2(\tau) + I^2(0)Q^2(\tau) + I^2(\tau)Q^2(0)\right\}. \tag{II.27}$$

The randomness of the baseband signals $I(t)$ and $Q(t)$ is due to the randomness of their samples i_k and q_k and their phase ϕ. Therefore, the average of any function of $I(t)$ and $Q(t)$ can be computed by sequentially averaging this function over i_k and q_k and then over θ if necessary. We will begin the evaluation of $E\left\{I^2(0)I^2(\tau)\right\}$ in (II.27) by taking the average over i_k first:

$$E_i\left\{I^2(0)I^2(\tau)\right\} = \sum_{k,l,m,n} E\{i_k i_l i_m i_n\} \operatorname{sinc}(\phi/\pi - k) \operatorname{sinc}(\phi/\pi - l) \cdot \operatorname{sinc}(b\tau + \phi/\pi - m) \operatorname{sinc}(b\tau + \phi/\pi - n), \tag{II.28}$$

where the summation operator with four indexes denotes four independent infinite sums over these indexes. Substituting (II.5a) into (II.28), we get

$$E_i\left\{I^2(0)I^2(\tau)\right\} = \sum_{k=-\infty}^{\infty} \operatorname{sinc}^2(\phi/\pi - k) \sum_{k=-\infty}^{\infty} \operatorname{sinc}^2(b\tau + \phi/\pi - k) + 2\left[\sum_{k=-\infty}^{\infty} \operatorname{sinc}(\phi/\pi - k) \operatorname{sinc}(b\tau + \phi/\pi - k)\right]^2 - 2\sum_{k=-\infty}^{\infty} \operatorname{sinc}^2(\phi/\pi - k) \operatorname{sinc}^2(b\tau + \phi/\pi - k). \tag{II.29}$$

Using symbolic math as explained in Appendix B, we can find closed form results of the above infinite sums. Substituting these results into (II.29) and taking the average over ϕ, we get

$$E_{i,\phi}\left\{I^2(0)I^2(\tau)\right\} = 1 + 2\,\mathrm{sinc}^2(b\tau) - 2\frac{1-\mathrm{sinc}(2b\tau)}{(\pi b\tau)^2}. \tag{II.30}$$

It can be shown that $E_{q,\phi}\left\{Q^2(0)Q^2(\tau)\right\} = E_{i,\phi}\left\{I^2(0)I^2(\tau)\right\}$.

The average $E_{i,q}\left\{I^2(0)Q^2(\tau)\right\}$ in (II.27) can be expanded as

$$E_{i,q}\left\{I^2(0)Q^2(\tau)\right\} = \sum_{k,l,m,n} E\{i_k i_l q_m q_n\}\,\mathrm{sinc}(\phi/\pi - k)\,\mathrm{sinc}(\phi/\pi - l) \cdot\ \mathrm{sinc}(b\tau + \phi/\pi - m)\,\mathrm{sinc}(b\tau + \phi/\pi - n). \tag{II.31}$$

Using (II.5b), we get

$$E_{i,q}\left\{I^2(0)Q^2(\tau)\right\} = \sum_{k=-\infty}^{\infty}\mathrm{sinc}^2(\phi/\pi - k)\sum_{k=-\infty}^{\infty}\mathrm{sinc}^2(b\tau + \phi/\pi - k) = 1. \tag{II.32}$$

The average $E_{i,q}\left\{I^2(\tau)Q^2(0)\right\}$ is also equal to 1.

Substituting the evaluated averages into (II.27), we get

$$R_{\mathrm{XMD}}(\tau) = \frac{4GP_{\mathrm{j}}P_{\mathrm{TX}}^2}{\mathrm{IIP}_3^2}\cos(\omega_{\mathrm{j}}\tau)\left[1 + \ \mathrm{sinc}^2(b\tau) - \frac{1-\mathrm{sinc}(2b\tau)}{(\pi b\tau)^2}\right]. \tag{II.33}$$

It can be shown that the summand 1 in the brackets of (II.33) represents a distortion component that is spectrally coincident with the jammer. We are only interested in those distortion components that are adjacent to the jammer. Therefore, we will rewrite the final result for the autocorrelation function of XMD as

$$R_{\mathrm{XMD}}(\tau) = \frac{4GP_{\mathrm{j}}P_{\mathrm{TX}}^2}{\mathrm{IIP}_3^2}\cos(\omega_{\mathrm{j}}\tau)\left[\mathrm{sinc}^2(b\tau) - \frac{1-\mathrm{sinc}(2b\tau)}{(\pi b\tau)^2}\right]. \tag{II.34}$$

Taking the Fourier transform of (II.34), we get the following two-sided PSD:

$$S_{\mathrm{XMD}}(u) = \frac{2GP_{\mathrm{j}}P_{\mathrm{TX}}^2}{b \cdot \mathrm{IIP}_3^2}|u|(1-|u|) \tag{II.35}$$

for $|u| < 1$, where $u = (|\omega| - \omega_{\mathrm{j}})/(2\pi b)$. It can be shown that XMD from BPGN is described by (II.35) with $|u|(1-|u|)$ replaced with $(1-|u|)$.

II.6 Comparison of Theoretical and Measured XMD Spectra

As a basis to compare theoretical and measured XMD spectra, we used an amplifier with $G = 14.5$dB and $\mathrm{IIP}_3 = -6.7$dBm. The TX leakage and jammer input powers were -25dBm. The measurement was done using a spectrum analyzer, which plots power within the resolution bandwidth (RBW) versus frequency. This plot is equivalent to a single-sided PSD. To convert the theoretical two-sided PSD $S_{\mathrm{XMD}}(u)$ into the corresponding single-sided spectrum, it was multiplied by two. The theoretical and measured single-sided XMD spectra are plotted in Fig. II.4. For comparison, this figure includes the XMD spectrum predicted by the Gaussian approximation. As can be seen, the proposed OQPSK signal model agrees well with the measured results, whereas the Gaussian approximation does not predict the XMD spectrum shape correctly.

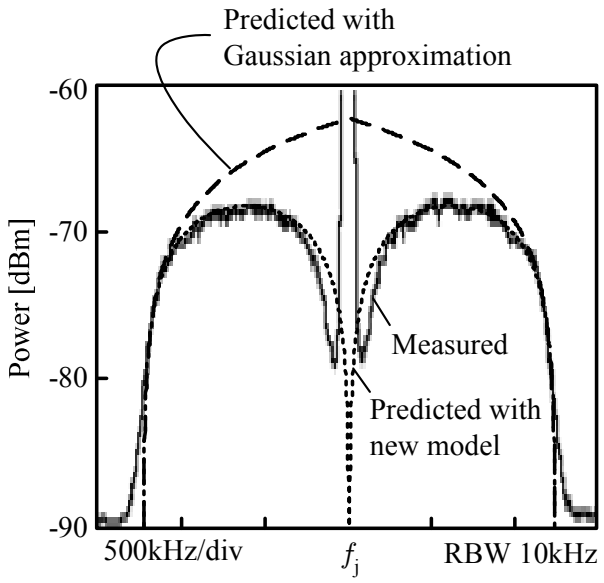

Figure II.4: Theoretical and measured single-sided XMD spectra.

II.7 Conclusions

We have proposed a new model of an OQPSK signal based on the mathematical description of a CDMA reverse-link modulator. Using this model, we showed that the statistical properties of the CDMA reverse-link signal are different from those of BPGN. We also showed that the power series model of the LNA transfer function can accurately take into account the circuit reactances if the expansion coefficients are expressed through the appropriate intercept points. Based on the proposed signal and transfer function models, we derived a closed-form expression of XMD in a CDMA LNA. It agreed well with the measured results, whereas the Gaussian approximation overestimated XMD closer to the jammer. The derived expression can be used to predict XMD of CDMA LNAs and to specify their IIP_3.

Chapter III

Derivation of NF and Linearity Requirements for CDMA LNAs

III.1 Introduction

As was explained in Chapter I, XMD generated by a CDMA LNA degrades the RX sensitivity in the presence of a jammer. To be able to estimate XMD, its closed-form expression was derived in the previous chapter based on the proposed models of the TX leakage signal and the LNA transfer function. This expression characterizes XMD in terms of the LNA IIP_3 and the signal properties, such as the input power and bandwidth. However, XMD is only a part of the total interference that degrades the RX sensitivity. Other contributors to this interference are the thermal noise generated in the RX, the thermal noise coupled from the TX through the antenna duplexer, and the LO phase noise reciprocally mixed with the jammer [126]. All of these contributors must be quantitively estimated to determine the linearity requirement of a CDMA LNA and choose the appropriate linearization method.

This chapter first quantifies the tolerable contribution of the RX thermal noise and derives the NF target for CDMA LNAs based on the sensitivity requirement of the phone.

Then, the targets for the LO phase noise and the LNA IIP_3 are derived using the single-tone desensitization requirement of the IS-95 standard.

III.2 Thermal Noise

As was mentioned earlier, there are two major contributors to the RX thermal noise: the noise generated by the RX itself and the TX noise in the RX band coupled through the antenna duplexer to the LNA input. Let us denote the corresponding available noise powers, referred to the antenna connector and integrated over the desired signal bandwidth, as N_{RX} and N_{TX}, respectively. The combined noise degrades the RX sensitivity, which is measured as the minimum power of the desired signal (forward-link CDMA signal) at the antenna connector at which the frame error rate (FER) does not exceed a specified value.

The maximum tolerable RX thermal noise power is set by the *receiver sensitivity and dynamic range* requirement of the IS-95 standard [2]. The power of the received desired signal at the mobile station antenna connector is denoted as $\hat{I}_{\mathrm{or}}$ in the standard. This signal contains several traffic channels transmitted at the same frequency and dedicated to different users in the same cell. The fractional power of a traffic channel in the desired signal is described as the ratio of the energy per PN chip in the traffic channel, E_c^{tr}, to the total power of the transmitted signal at the base station antenna connector, I_{or}. According to the RX sensitivity and dynamic range requirement, the RX FER must not exceed 0.5% when the desired signal power is -104dBm/1.23MHz at the mobile antenna, with the fractional

power of the dedicated traffic channel of -15.6dB, i.e.,

$$\hat{I}_{\rm or} = 10^{-104/10} \quad [\rm mW], \tag{III.1a}$$

$$\frac{E_c^{\rm tr}}{I_{\rm or}} = 10^{-15.6/10}. \tag{III.1b}$$

As specified by the standard, to guarantee 0.5% FER for a traffic channel in a white Gaussian noise, the ratio of the average energy per data bit to the effective noise power spectral density, $E_b^{\rm tr}/N_t$, should be 4.5dB or more. The maximum allowed thermal noise at the antenna can be computed using the following CDMA equation [2]:

$$I_{\rm oc} = \frac{\hat{I}_{\rm or} \times E_c^{\rm tr}/I_{\rm or}}{E_b^{\rm tr}/N_t} G_p, \tag{III.2}$$

where $I_{\rm oc}$ is the interference power within the desired signal bandwidth referred to the antenna connector, and G_p is the processing gain equal to the ratio of the spreading rate (1.2288Mcps) to the data rate (9.6kbps).

It is often much easier to reduce the RX thermal noise than other contributors to the total interference in the presence of a strong jammer. Therefore, reducing $N_{\rm RX} + N_{\rm TX}$ beyond the sensitivity requirement would give more room for XMD and the reciprocally mixed LO phase noise. For this reason, some margin is applied to the required sensitivity of -104dBm/1.23MHz. This margin is typically 4dB for a cellular-band RX and 2.5dB for a PCS band RX. The corresponding sensitivities of -108dBm/1.23MHz and -106.5dBm/1.23MHz are also used by wireless carriers as a benchmark of the phone performance. Substituting these sensitivities and $I_{\rm oc} = N_{\rm RX} + N_{\rm TX}$ into (III.2), we get the

following requirement to the total thermal noise:

$$N_{\mathrm{RX}} + N_{\mathrm{TX}} \leq \begin{cases} 10^{-107/10}, & \text{cellular RX} \\ 10^{-105.5/10}, & \text{PCS RX} \end{cases} \quad [\mathrm{mW}]. \tag{III.3}$$

The TX noise density in the RX band is typically -135dBm/Hz at the power amplifier output in both RX bands. Characteristics of some commonly-used SAW duplexers are listed in Table III.1, where L_{TX} is the TX-antenna insertion loss, L_{RX} is the antenna-RX insertion loss, $L_{\mathrm{TX-RX,TX}}$ is the TX-RX isolation in the TX band, and $L_{\mathrm{TX-RX,RX}}$ is the TX-RX isolation in the RX band. As can be seen, a typical $L_{\mathrm{TX-RX,RX}}$ is 45dB for a cellular duplexer and 40dB for a PCS duplexer. Therefore, the TX noise density in the RX band at the antenna is typically -180dBm/Hz for a cellular RX and -175dBm/Hz for a PCS RX. Dividing both sides of (III.3) by 1.23E6 and subtracting the estimated TX noise densities, we will find that the thermal noise generated by the cellular and PCS RXs should not exceed -168.2dBm/Hz and -167.1dBm/Hz, respectively, which corresponds to the cascaded NFs of 5.8dB and 6.9dB, respectively. As can be seen from Table III.1, the antenna-RX insertion loss is typically 3.2dB for a cellular duplexer and 4.2dB for a PCS duplexer. Most CDMA phones operate in both bands, and, in addition to the cellular and PCS duplexers, they use a diplexer to separate the two bands. Its typical insertion loss is 0.5dB along the cellular path and 0.6dB along the PCS path. Adding these losses to L_{RX} and subtracting the results from the cascaded NFs, we will find that the NF of both RXs without the front-end duplex and diplex filters should not exceed 2.1dB. To meet this requirement, the LNA maximum NF is usually specified to be 1.8dB with the power gain of 16 ± 1dB.

Table III.1: Characteristics of typical cellular and PCS SAW duplexers

Duplexer	Freq. Band	L_{TX} [dB]	L_{RX} [dB]	$L_{\mathrm{TX-RX,TX}}$ [dB]	$L_{\mathrm{TX-RX,RX}}$ [dB]	Size [mm^2]
Murata SAYDV836MAB0F00	Cell.	2.3	3.5	55	45	3.8x3.8
Fujitsu FAR-D5CF-881M50-D1F1	Cell.	2.3	3.3	55	45	3.8x3.8
Sawtek 856356	Cell.	2.3	3.0	55	45	3.8x3.8
EPCOS B7630	Cell.	2.5	3.2	54	46	3.8x3.8
Sanyo SS836P881PM22(ES-2)	Cell.	2.5	3.3	57	44	3.8x3.8
EPCOS LM56A	Cell.	3.0	4.5	55	46	3.0x2.5
Agilent ACMD-7402	PCS	3.5	3.8	54	45	3.8x3.8
Murata SAYHP1G88ED0F00R02	PCS	3.5	4.2	55	45	5x5
EPCOS B7634	PCS	3.5	4.5	50	44	5x5
Fujitsu FAR-D6CZ-1G9600-D1X3	PCS	3.5	4.2	50	40	5x5
Sanyo SS188P196QL12(ES-Q7)	PCS	4.0	4.3	50	40	5x5

III.3 LO Phase Noise

Another interference to a CDMA RX comes from the LO phase noise, which mixes with a strong jammer in the RX mixer, producing unwanted noise products at the intermediate frequency (IF). This phenomenon is called reciprocal mixing and is explained in Fig. III.1. The LO phase noise combined with the RX thermal noise and XMD degrade the RX sensitivity in the presence of a jammer. The maximum allowable total interference power $I_{\rm oc}$ in this case is set by the *single-tone desensitization* requirement of the IS-95 standard, in which the jammer is considered to be a CW signal. The test conditions for this requirement are summarized in Table III.2, where $P_{\rm j,ant}$ and $P_{\rm TX,ant}$ are respectively the jammer and TX leakage powers at the antenna connector, and $L_{\rm dip}$ is the diplexer insertion loss in the corresponding frequency band. As defined in [2], the RX FER must not exceed 1% when the received desired signal power $\hat{I}_{\rm or}$ is -101dBm/1.23MHz with the fractional power of the dedicated traffic channel of -15.6dB. Assuming that the total interference has a Gaussian distribution, the minimum E_b/N_t is 4.3dB for 1% FER.

The LO phase noise that contaminates the desired signal band is confined to the ($f_{\rm o}-b/2, f_{\rm o}+b/2$) offset frequency range, where $f_{\rm o}$ is given in Table III.2. Let us denote the phase noise power integrated over this range and referenced to the LO carrier power as N_ϕ. Assuming that the VCO phase noise exhibits a typical $1/f^2$ frequency dependence in this range, N_ϕ can be calculated as follows

$$N_\phi = S_\phi(f_{\rm o}) \int_{f_{\rm o}-b/2}^{f_{\rm o}+b/2} \left(\frac{f_{\rm o}}{f}\right)^2 df = S_\phi(f_{\rm o}) \frac{b f_{\rm o}^2}{f_{\rm o}^2 - b^2/4}, \qquad \text{(III.4)}$$

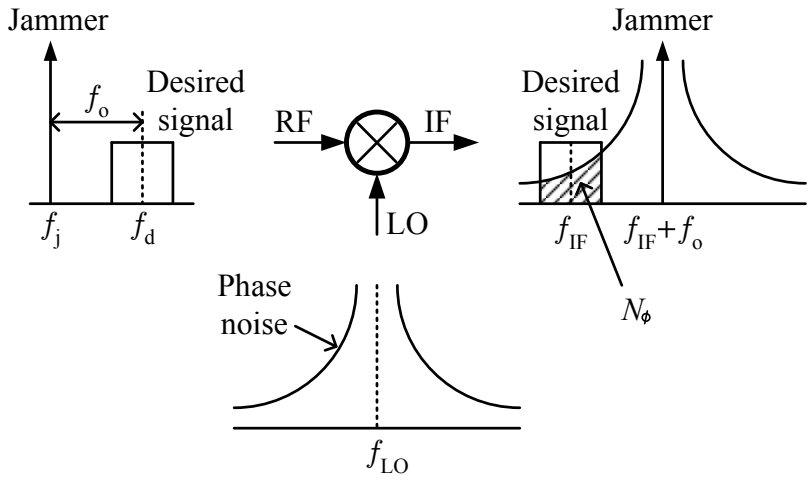

Figure III.1: Reciprocal mixing in a superheterodyne receiver.

Table III.2: Single-tone desensitization test conditions

Parameter	Cellular RX	PCS RX
Jammer power at antenna, $P_{\mathrm{j,ant}}$	-30dBm	-30dBm
TX power at antenna, $P_{\mathrm{TX,ant}}$	28dBm$-L_{\mathrm{TX}}-L_{\mathrm{dip}}$	28dBm$-L_{\mathrm{TX}}-L_{\mathrm{dip}}$*
Jammer offset from RX channel, f_{o}	0.9MHz	1.25MHz
RX-TX channel offset	45MHz	80MHz
Data rate	9600bps	9600bps
Forward-link signal power at mobile antenna connector, $\hat{I}_{\mathrm{or}}$	-101dBm/1.23MHz	-101dBm/1.23MHz
Traffic channel fractional power, $E_c^{\mathrm{tr}}/I_{\mathrm{or}}$	-15.6dB	-15.6dB

*In contrary to the requirements of the IS-95 standard, wireless carriers test the single-tone desensitization of a PCS RX at the maximum output power of the the power amplifier (typically, +28dBm) with the open-loop power control.

where $S_\phi(f_\mathrm{o})$ is the VCO phase noise density at the frequency offset f_o.

The reciprocal mixing interference component referenced to the antenna connector can be calculated as $N_\phi P_{\mathrm{j,ant}}$ in the linear domain [35]. For now, we will neglect XMD and add 3dB margin to E_b/N_t to account for XMD later. Substituting $N_\mathrm{RX} + N_\mathrm{TX} + N_\phi P_{\mathrm{j,ant}}$ in place of I_oc in (III.2), we can derive the following requirement:

$$N_\mathrm{RX} + N_\mathrm{TX} + N_\phi P_{\mathrm{j,ant}} \leq 10^{-102.8/10} \quad [\mathrm{mW}]. \tag{III.5}$$

Substituting $P_{\mathrm{j,ant}} = -30$dBm and (III.3) into (III.5), we will find that N_ϕ should not exceed -74.9dBc for a cellular RX and -76.2dBc for a PCS RX. Substituting these numbers into (III.4), we will find that the LO phase noise density should be less than -138.5dBc/Hz at 900kHz for a cellular RX and -138.3dBc/Hz at 1.25MHz for a PCS RX.

III.4 Cross-Modulation Distortion

Among the RX front-end stages, it is the LNA that is responsible for most of XMD. The post-LNA RF SAW filter (see Fig. I.1) significantly attenuates the TX leakage such that XMD generated in the mixer and the following stages is negligible. Therefore, it is safe to assume that XMD in a CDMA RX is generated entirely by the LNA.

As it is shown in Fig. III.2, only a portion of the total XMD power falls into the desired signal band. Let us denote this portion referred to the antenna connector as P_XMD. It can be found as

$$P_\mathrm{XMD} = 2\int_{f_\mathrm{j}+f_\mathrm{o}-b/2}^{f_\mathrm{j}+b} \frac{L_\mathrm{dip} L_\mathrm{RX} S_\mathrm{XMD}(u)}{G} df, \tag{III.6}$$

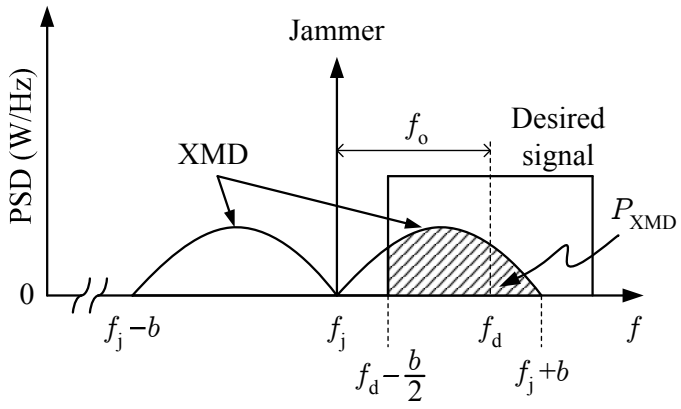

Figure III.2: XMD spectrum of a jammer adjacent to the desired signal.

where G is the LNA power gain, $S_{\mathrm{XMD}}(u)$ is the XMD PSD given by (II.35), and $u = (f - f_{\mathrm{j}})/b$. The factor of two is included in (III.6) to take into account the negative frequency spectrum. Replacing df with bdu in (III.6) and changing the integration domain to $(f_{\mathrm{o}}/b - 1/2, 1)$, we find

$$P_{\mathrm{XMD}} = \frac{4P_{\mathrm{j,ant}}P_{\mathrm{TX}}^2}{3\mathrm{IIP}_3^2}\frac{f_{\mathrm{o}}}{b}\left(\frac{3}{2} - \frac{f_{\mathrm{o}}}{b}\right)^2, \tag{III.7}$$

where we took into account the fact that $L_{\mathrm{dip}}L_{\mathrm{RX}}P_{\mathrm{j}} = P_{\mathrm{j,ant}}$ in the linear domain. Using the f_{o} values from Table III.2 and converting (III.7) to the log domain, we get

$$P_{\mathrm{XMD}} = P_{\mathrm{j,ant}} + 2P_{\mathrm{TX}} - 2\mathrm{IIP}_3 - \begin{cases} 2.4, & \text{cellular RX} \\ 5.0, & \text{PCS RX} \end{cases} \quad [\mathrm{dBm}]. \tag{III.8}$$

We should remember that P_{TX} is the TX leakage power at the LNA input, which can be related to the transmitted power at the antenna as $P_{\mathrm{TX}} = P_{\mathrm{TX,ant}} + L_{\mathrm{dip}} + L_{\mathrm{TX}} - L_{\mathrm{TX-RX,TX}}$ in the log domain.

Applying the CDMA equation (III.2) to the total interference and using the sensitivity requirements for the single-tone desensitization test without any margins, we can derive the

following requirement:

$$N_{\mathrm{RX}} + N_{\mathrm{TX}} + N_{\phi} P_{\mathrm{j,ant}} + P_{\mathrm{XMD}} \leq 10^{-99.8/10} \quad [\mathrm{mW}]. \tag{III.9}$$

Substituting (III.5) into (III.9), we fill find that P_{XMD} should be less than -102.8dBm. Substituting this value into (III.8) and using the data from Table III.2, we get the following requirement for the LNA IIP_3:

$$\mathrm{IIP}_3 \geq \begin{cases} 63.2 - L_{\mathrm{TX-RX,TX}}, & \text{cellular LNA} \\ 61.9 - L_{\mathrm{TX-RX,TX}}, & \text{PCS LNA} \end{cases} \quad [\mathrm{dBm}]. \tag{III.10}$$

As we can see, the LNA IIP_3 target is inversely proportional to the duplexer TX-RX isolation in the TX band. Referring to Table III.1, the minimum $L_{\mathrm{TX-RX,TX}}$ of typical cellular and PCS SAW duplexers is 55dB. Thus, the IIP_3 targets of cellular and PCS LNAs are +8.2dBm and +6.9dBm, respectively. Since the combined jammer and TX leakage power at the LNA input is approximately -26dBm in the worst case, the above IIP_3 targets should be met at the combined input power of the 2-tone excitation of less than -26dBm.

III.5 Conclusions

We have derived the IIP_3 and NF requirements of the LNAs used in CDMA mobile stations. Using a typical SAW duplexer, the minimum IIP_3 should be +8.2dBm for a cellular LNA and +6.9dBm for a PCS LNA, while the NF should not exceed 1.8dB with the power gain of 16 ± 1dB. This design goal is very challenging since the IIP_3 of a typical LNA does not exceed 0dBm without using linearization techniques.

Chapter IV

Optimum Out-of-Band Tuning

IV.1 Introduction

In the previous chapter, we have seen that the requirement to IIP_3 of a CDMA LNA is so challenging that it requires the use of linearization techniques. Among different techniques reviewed in Chapter I, the optimum out-of-band tuning is the only technique that can significantly increase IIP_3 without degrading other circuit performance such as NF and gain. Unfortunately, it is only suitable for circuits with a gain expansion, i.e., with the 1st and 3rd-order power series coefficients of the same sign. A common-emitter BJT amplifier is an example of such a circuit.

This chapter presents a Volterra Series analysis of a common-emitter circuit and explains how the difference-frequency and 2nd-harmonic terminations of the circuit affect its IMD_3. The derived closed-form expression of IIP_3 is used to find the optimum values of these terminations for a 2GHz Si BJT LNA. A simpler version of this method based on using a low-frequency low-impedance input termination is also theoretically explained and experimentally verified on a 900MHz SiGe HBT LNA. Different methods for generating such a termination are reviewed.

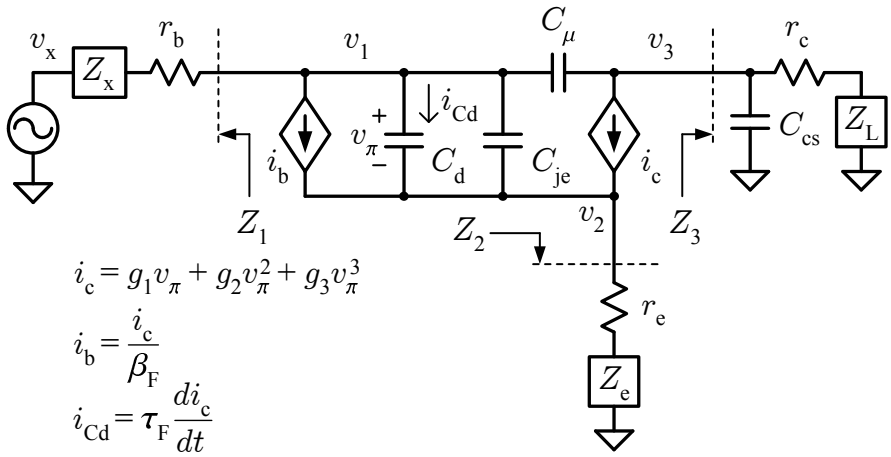

Figure IV.1: Small-signal nonlinear equivalent circuit of a common-emitter BJT.

IV.2 Volterra Series Analysis of Common-Emitter Circuit

In this section, a closed-form expression of IIP_3 of a common-emitter BJT is derived.

Consider a simplified model of a common-emitter gain stage shown in Fig. IV.1. The signal generator is connected to the base through a matching circuit and is modeled by a Thevenin equivalent circuit with an open-circuit voltage v_x and a transformed output impedance Z_x. The emitter is degenerated with Z_e, and the collector is loaded with Z_L. In general, the terminating impedances Z_x, Z_e, and Z_L are frequency dependent. The BJT is represented by its small-signal nonlinear equivalent circuit for the forward-active region. In this circuit, the following simplifying assumptions are made:

1. The collector current i_c is independent of the base-collector voltage. This assumption is valid if the BJT operates far from the saturation and breakdown regions. The output resistance modeling the Early effect can be ignored because it is much larger than the load impedance for most RF circuits. So, i_c can be expanded in a one-dimensional

power series in terms of the internal base-emitter voltage around the bias point as

$$i_{\rm c}(v_\pi) = g_1 v_\pi + g_2 v_\pi^2 + g_3 v_\pi^3 + \cdots \ , \tag{IV.1}$$

where $v_\pi = v_1 - v_2$, and g_n is the nth-order expansion coefficient, given by

$$g_n = \frac{1}{n!}\frac{\partial^n I_{\rm C}}{\partial V_{\rm BE}^n}. \tag{IV.2}$$

Above, $I_{\rm C}$ is the dc collector current, and $V_{\rm BE}$ is the dc base-emitter voltage. For a BJT biased in the forward active region,

$$I_{\rm C} = I_0 e^{V_{\rm BE}/\phi_{\rm t}}, \tag{IV.3}$$

where $\phi_{\rm t}$ is the thermal voltage kT/q. Therefore,

$$g_1 = \frac{I_{\rm C}}{\phi_{\rm t}}, \quad g_2 = \frac{I_{\rm C}}{2\phi_{\rm t}^2}, \quad g_3 = \frac{I_{\rm C}}{6\phi_{\rm t}^3}, \quad \cdots \quad . \tag{IV.4}$$

2. Base resistance $r_{\rm b}$ is constant. In reality, $r_{\rm b}$ decreases as the base current increases due to current crowding, base-width modulation, base conductivity modulation, and base push-out effects [127]. The assumption of the bias-independent $r_{\rm b}$ is acceptable if the real part of $Z_{\rm x}$ is much larger than $r_{\rm b}$.

3. Base-emitter junction capacitance $C_{\rm je}$ is constant. This assumption is plausible because of the relatively weak dependence of $C_{\rm je}$ on the bias voltage in the forward-active region at sufficiently high collector bias currents [128].

4. Base-collector and collector-substrate capacitances, C_μ and $C_{\rm cs}$, are constant. This is close to reality if the corresponding junctions are strongly reverse-biased.

5. The forward dc current gain $\beta_{\rm F}$ and the forward transit time $\tau_{\rm F}$ are constant. This assumption restricts the validity of the analysis to the collector bias currents below the levels causing the high-level injection and $f_{\rm T}$ roll-off. With constant $\beta_{\rm F}$ and $\tau_{\rm F}$, the base current $i_{\rm b}$ and the current through the base-emitter diffusion capacitance $C_{\rm d}$ are linear functions of the nonlinear collector current $i_{\rm c}$, i.e.,

$$i_{\rm b} = \frac{i_{\rm c}}{\beta_{\rm F}}, \tag{IV.5}$$

$$i_{\rm Cd} = \tau_{\rm F}\frac{di_{\rm c}}{dt} = s\tau_{\rm F} i_{\rm c}, \tag{IV.6}$$

where s is the Laplace variable.

The goal of the analysis is to find IIP_3 in the case of a two-tone excitation

$$v_{\rm x}(t) = A\left[\cos(\omega_{\rm a}t) + \cos(\omega_{\rm b}t)\right], \tag{IV.7}$$

where $\omega_{\rm a}$ and $\omega_{\rm b}$ are two closely spaced angular frequencies, and A is the amplitude of the tones. Since the output signal is linearly related to v_3, IIP_3 can be computed if we know the Volterra series for v_3 in terms of the input voltage $v_{\rm x}$:

$$v_3 = C_1(s)\circ v_{\rm x} + C_2(s_1,s_2)\circ v_{\rm x}^2 + C_3(s_1,s_2,s_3)\circ v_{\rm x}^3 + \cdots \quad , \tag{IV.8}$$

where $C_n(s_1, s_2, \cdots, s_n)$ is the nth-order nonlinear transfer function. We will treat IIP_3 as the available power of the signal generator. It is given by [10]

$$\text{IIP}_{3,2\omega_{\rm b}-\omega_{\rm a}} = \frac{A^2_{\text{IP3},2\omega_{\rm b}-\omega_{\rm a}}}{8\text{Re}(Z_1(s_{\rm a}))} = \frac{1}{6\text{Re}(Z_1(s_{\rm a}))}\left|\frac{C_1(s_{\rm a})}{C_3(s_{\rm b}, s_{\rm b}, -s_{\rm a})}\right|, \tag{IV.9}$$

where we used expression (II.19) for $A_{\text{IP3},2\omega_{\rm b}-\omega_{\rm a}}$.

To find the transfer functions of (IV.8), we will use the *harmonic input* method [10]. This method is based on probing the circuit with a multi-tone excitation and solving the Kirchhoff's law equations in frequency domain at the sum of all input frequencies. The frequencies should be incommensurable, and their number should be equal to the order of the nonlinear transfer function to be found. The procedure starts with a single-tone excitation to determine the linear transfer function and is continued to higher order functions by adding one more input tone at each step.

The derivation of the 1st and 3rd-order coefficients of the Volterra series (IV.8) for a narrow tone separation is shown in Appendix C. Substituting (C.15) into (IV.9) and expanding some of the shorthand notations, we get

$$\mathrm{IIP}_{3,2\omega_\mathrm{b}-\omega_\mathrm{a}} = \frac{1}{6\mathrm{Re}(Z_1(s))\,|H(s)|\,|A_1(s)|^3\,|\varepsilon(\Delta s, 2s)|}, \tag{IV.10}$$

where

$$H(s) = \frac{1 + sC_\mathrm{je}\left[Z_1(s) + Z_2(s)\right] + sC_\mu Z_1(s)\left(1 + 1/\beta_\mathrm{F} + s\tau_\mathrm{F}\right)}{g_1 - sC_\mu\left[1 + Z_2(s)\left(g_1 + g_1/\beta_\mathrm{F} + s\tau_\mathrm{F} g_1 + sC_\mathrm{je}\right)\right]}, \tag{IV.11a}$$

$$A_1(s) = \frac{1}{g_1 + g(s)} \cdot \frac{1 + sC_\mu Z_3(s)}{\left(1/\beta_\mathrm{F} + s\tau_\mathrm{F}\right)\left[Z_1(s) + Z(s)\right] + Z(s)}, \tag{IV.11b}$$

$$\varepsilon(\Delta s, 2s) = g_3 - \frac{2g_2^2}{3}\left[\frac{2}{g_1 + g(\Delta s)} + \frac{1}{g_1 + g(2s)}\right], \tag{IV.11c}$$

$$g(s) = \frac{1 + sC_\mathrm{je}\left[Z_1(s) + Z(s)\right] + sC_\mu\left[Z_1(s) + Z_3(s)\right]}{\left(1/\beta_\mathrm{F} + s\tau_\mathrm{F}\right)\left[Z_1(s) + Z(s)\right] + Z(s)}, \tag{IV.11d}$$

$$Z(s) = Z_2(s) + sC_\mu\left[Z_1(s)Z_2(s) + Z_1(s)Z_3(s) + Z_2(s)Z_3(s)\right], \tag{IV.11e}$$

$$s \approx s_\mathrm{a} \approx s_\mathrm{b}, \tag{IV.11f}$$

$$\Delta s = s_\mathrm{b} - s_\mathrm{a}. \tag{IV.11g}$$

The derived closed-form expression for IIP_3 differs from that derived in [129] by including the base-collector capacitance C_μ, which noticeably affects the distortion at high frequencies.

IV.3 Effect of Out-of-Band Terminations on IIP3

Equation (IV.10) shows that IIP_3 depends on the circuit *in-band* impedances, i.e., those at ω ($\approx \omega_\mathrm{a} \approx \omega_\mathrm{b}$) and *out-of-band* impedances, i.e., those at $\Delta\omega$ ($= \omega_\mathrm{b} - \omega_\mathrm{a}$) and 2ω. The dependence on the in-band impedances is introduced by $\mathrm{Re}(Z_1(s))$, $|H(s)|$, and $|A_1(s)|$ in the denominator of (IV.10). Since $|A_1(s)|$ is raised to power of three, it determines the IIP_3 dependence on the in-band impedances. Being a transfer function from v_x to v_π, $A_1(s)$ has to be reduced for a higher IIP_3. This is typically achieved by increasing the output impedance of the signal generator $Z_\mathrm{x}(s)$ or by increasing the emitter degeneration impedance $Z_\mathrm{e}(s)$ or both. These measures reduce the gain of a common-emitter stage. More often, the in-band impedances $Z_\mathrm{x}(s)$ and $Z_\mathrm{e}(s)$ are selected from gain, input matching, and NF considerations.

The dependence of IIP_3 on the out-of-band impedances is introduced by $|\varepsilon(\Delta s, 2s)|$, which shows how the collector current nonlinearities contribute to its IMD_3 response. The first term in (IV.11c) represents the contribution of the 3rd-order nonlinearity of i_c, and the terms in brackets come from the 2nd-order nonlinearity. Even though IMD_3 is the odd-order distortion, the 2nd-order nonlinearity still contributes to it by first generating the 2nd-order responses and then, after they are fed back to the input, mixing them with

the fundamental excitations. In the analyzed circuit of Fig. IV.1, the feedback paths are introduced by the emitter-degeneration network with impedance Z_2, the base-collector capacitance C_μ, and the i_b and i_Cd dependence on i_c (see (IV.5) and (IV.6)). If the operating frequency is low enough that the circuit reactances can be neglected up to the 2nd-harmonic frequency, $|\varepsilon(\Delta s, 2s)| \cong |g_3|$.

Examination of (IV.11d) and (IV.11e) shows that, if the terminal impedances $Z_1(s)$, $Z_2(s)$ and $Z_3(s)$ have positive real parts, which is usually the case, $\mathrm{Re}(g(s))$ is also positive. Therefore, for RF amplifiers, $|\varepsilon(\Delta s, 2s)|$ can be made less than $|g_3|$ provided that g_3 is positive, i.e., the device exhibits gain expansion for small signals. This is exactly the behavior of BJTs. Their out-of-band terminal impedances can be selectively tuned so that the IMD_3 responses of the self-interacting 2nd-order nonlinearity cancel those of the 3rd-order nonlinearity according to (IV.11c) [130]. The resulting IMD_3 can theoretically be zero regardless of the input power (neglecting the 5th and higher odd-order nonlinearities).

The optimum Z_x and Z_L at the difference and 2nd-harmonic frequencies $\Delta\omega$ and 2ω are found by setting $\varepsilon(\Delta s, 2s)$ to zero. To cancel IMD_3 for a wide range of the tone frequencies, $g(s)$, which is responsible for the frequency dependence of $\varepsilon(\Delta s, 2s)$, should be constant in the corresponding ranges of the 2nd-order mixing frequencies, i.e.,

$$g(\Delta s) = 1/r, \tag{IV.12a}$$

$$g(2s) = \left(\frac{3g_3}{2g_2^2} - \frac{2r}{1+g_1 r}\right)^{-1} - g_1, \tag{IV.12b}$$

where r is a constant in units of Ω, and the right side of (IV.12b) is derived to make $\varepsilon(\Delta s, 2s)$ zero. Equations (IV.12a) and (IV.12b) are under-determined and, therefore, have

many solutions for optimum out-of-band $Z_{\rm x}$ and $Z_{\rm L}$. Among them, only those with positive real parts are of interest.

Making $\varepsilon(\Delta s, 2s) = 0$ cancels the IMD$_3$ product at $2\omega_{\rm b} - \omega_{\rm a}$ but not necessarily at $2\omega_{\rm a} - \omega_{\rm b}$. The latter is proportional to $|\varepsilon(-\Delta s, 2s)|$, which is generally not equal to $|\varepsilon(\Delta s, 2s)|$ because $g(-\Delta s)$ is conjugate to $g(\Delta s)$ due to nonzero reactive parts of the terminating impedances at $\Delta\omega$. The phenomenon of unequal IMD$_3$ responses at $2\omega_{\rm a} - \omega_{\rm b}$ and $2\omega_{\rm b} - \omega_{\rm a}$ is known as the IMD$_3$ asymmetry and is usually attributed to the reactive parts of the terminating impedances at the difference frequency [57], [120], [131]-[133]. At larger $\Delta\omega$, this asymmetry can also be caused by different circuit impedances at $2\omega_{\rm a}$ and $2\omega_{\rm b}$ and, thus, by different contributions of the 2nd harmonics to the corresponding 3rd-order products, i.e., $g(2s_{\rm a}) \neq g(2s_{\rm b})$. The IMD$_3$ asymmetry is undesirable because the lower and upper-side IMD$_3$ responses can not be cancelled simultaneously. To make these responses equal at small $\Delta\omega$, $\mathrm{Im}(g(\Delta s))$ should be set to 0, i.e., r in (IV.12a) should be real.

The out-of-band load impedance affects IMD$_3$ due to the feedback through C_μ. For a typical narrow-band RF circuit, $Z_{\rm L}(\Delta s)$ is much smaller than $1/(\Delta s C_\mu)$. So, the feedback through C_μ and the effect of $Z_{\rm L}$ at $\Delta\omega$ can be neglected; $Z_{\rm x}(\Delta s)$ is then the only optimized difference-frequency termination, which can be found from (IV.12a). For an inductively degenerated common-emitter stage with $Z_2(s) = r_2 + sL_2$, the solution of (IV.12a) is very accurately approximated by

$$Z_{\rm x,opt}(\Delta s) \cong \beta_{\rm F}\,(r - r_2) - r_{\rm b} - \Delta s \beta_{\rm F}\left[L_2 + \beta_{\rm F}\,(\tau_{\rm F} - rC_{\rm je})\,(r - r_2)\right]. \qquad \text{(IV.13)}$$

For the power series coefficients given by (IV.4), $3g_3/(2g_2^2) = 1/g_1$, and (IV.12b) simplifies to

$$g(2s) = \frac{2g_1}{\dfrac{1}{g_1 r} - 1}. \tag{IV.14}$$

Three important observations can be made from (IV.13) and (IV.14):

1. According to (IV.14), for a given value of r, the optimum source and load impedances at 2ω depend on the BJT small-signal transconductance g_1, which is proportional to the collector dc current. This dependence is undesirable and can be minimized if r is chosen much smaller than $1/g_1$.

2. If $r < r_2 + r_\mathrm{b}/\beta_\mathrm{F}$, $\mathrm{Re}(Z_{\mathrm{x,opt}}(\Delta s))$ is negative and can not be implemented without making the circuit unstable. On the other hand, choosing r relatively large may force the solutions to (IV.14) to have negative real parts, which is not desirable either.

3. According to (IV.13), $Z_{\mathrm{x,opt}}(\Delta s)$ strongly depends on β_F, which varies by more than 50% over process and temperature for a typical bipolar process. This dependence may cause the IIP_3 of an optimally terminated circuit to vary by several dB.

The presented analysis of the distortion cancellation is based on zeroing the 3rd-order transfer function C_3. The contributions of the 5th and higher odd-order terms of v_3 were neglected. Generally, these terms are not cancelled by tuning Z_x and Z_L at the out-of-band frequencies that affect only C_3. As a result, it is impossible to achieve zero IMD_3. With the cancelled 3rd-order nonlinearity, the IMD_3 power should increase faster than 3dB

per 1dB of the input power due to nonzero contributions of the 5th and higher odd-order nonlinearities to IMD_3, making IIP_3 dependent on the input power.

IV.4 2GHz Si BJT LNA Design

A schematic diagram of the designed 2GHz LNA is shown in Fig. IV.2, where the dashed box marks the boundaries of a discrete bipolar transistor, and the inductances inside the box ($L_{\rm b}$, $L_{\rm e}$, and $L_{\rm c}$) model the bondwires. The components outside the dashed box are implemented on a printed-circuit (PC) board. The discrete transistor is biased at 5mA collector current from 2.7V supply. The operating frequency of the LNA was chosen outside the commercial frequency bands just to demonstrate the developed the optimum out-of-band tuning method. In a practical application, the impedances of an external source and load outside the operating frequency range are not well defined: for a CDMA LNA, they are set by the duplexer and the RF SAW filter shown in Fig. I.1, and their 2nd-harmonic values also depend on the trace lengths. To avoid the IIP_3 dependence on these impedances, they are decoupled from the transistor terminals by the shunt $\lambda/4$ microstrip lines ML_1 and ML_5. These lines are almost open circuits around 2GHz and do not affect the LNA in-band performance. For simplicity, only the out-of-band source impedance is optimally tuned for low IMD_3. The out-of-band load impedance is fixed by ML_5 such that $Z_{\rm L}(2\omega) \approx j2\omega L_{\rm c}$ and $Z_{\rm L}(\Delta\omega) \approx 0$.

With the signal generator shorted to ground at 2ω, a well controlled nonzero real part of $Z_{\rm x}(2\omega)$ can only be produced by a resistor in the input matching network. We found that

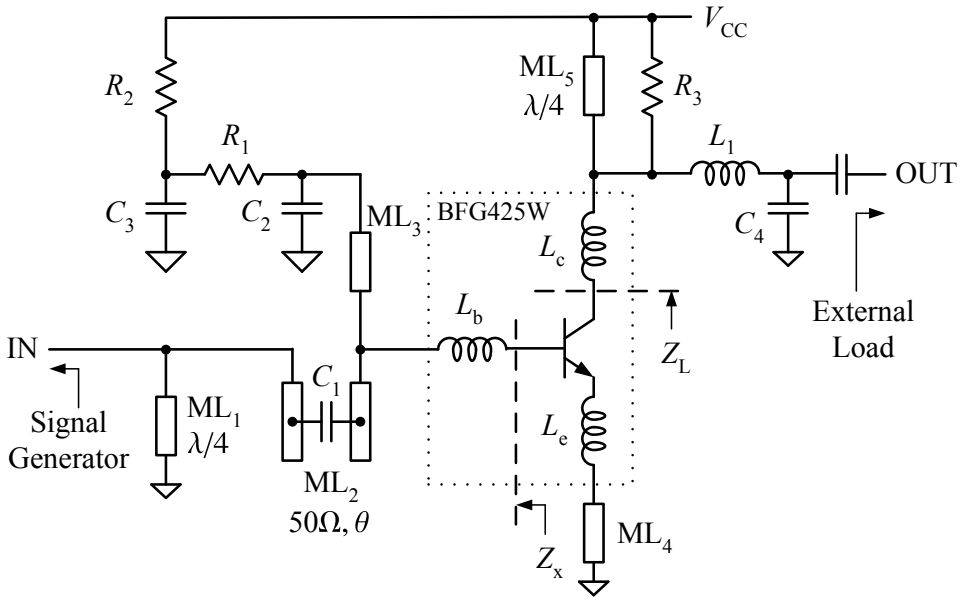

Figure IV.2: Schematic diagram of the 2GHz Si BJT LNA.

this resistor can not be well isolated from the LNA input in a wide-enough frequency range around 2GHz, and, as a result, it degrades the LNA NF. To avoid the need for this resistor, the optimized values of $Z_{\rm x}(2\omega)$ were limited to those with the real part close to zero. For given $Z_{\rm L}(2\omega)$, this restriction allowed us to solve (IV.14) for r and optimum $\mathrm{Im}(Z_{\rm x}(2\omega))$. Once r was defined, $Z_{\rm x,opt}(\Delta\omega)$ was found from (IV.13). $\mathrm{Im}(Z_{\rm x,opt}(\Delta\omega))/\Delta\omega$ turned out to be a negative constant in this frequency range.

The input matching network is designed to match the LNA input to 50Ω around 2GHz and to optimally terminate it at $2f$ of 4GHz and at $(f_{\rm b} - f_{\rm a})$ up to 50MHz. ML_3 ac-grounded by C_2 is used for in-band matching. $Z_{\rm x}(\Delta\omega)$ is set by tunable R_1 in parallel with C_2. The time constant of this RC network is selected much smaller than $1/\Delta\omega$ such that $Z_{\rm x}(\Delta\omega) \approx R_1 - j\Delta\omega C_2 R_1^2$, where $-C_2R_1^2$ is equal to the desired negative constant $\mathrm{Im}(Z_{\rm x,opt}(\Delta\omega))/\Delta\omega$. The value of C_2 is still large enough to provide a good ac ground

for ML_3 and to isolate R_1 from the LNA input at 2GHz. C_3 is the ac-ground for R_1. R_2 is used to set the BJT dc bias current. $Z_{\rm x}(2\omega)$ is defined by tunable ML_2 in parallel with ML_3. ML_2 is tuned by sliding the dc blocking capacitor C_1 along the parallel portions of ML_2. Because the characteristic impedance of ML_2 is 50Ω, and because ML_1 is an open circuit around 2GHz, the ML_2 tuning does not affect the LNA in-band input match. The computed optimum and implemented source impedances are plotted as functions of frequency in Fig. IV.3. As can be seen in the figure, the implemented impedance $Z_{\rm x}(\Delta\omega)$ follows the optimum one very closely for the tone separation frequencies below 20MHz. On the other hand, the implemented impedance $Z_{\rm x}(2\omega)$ is close to the optimum one only at 4GHz.

ML_4 in series with $L_{\rm e}$ is used to bring the conjugate input impedance of the transistor closer to the source impedance needed for the minimum NF. L_1 and C_4 form the output matching network. R_3 is used for LNA stabilization.

IV.5 Measured Results of 2GHz Si BJT LNA

The designed LNA was biased from 2.7V supply with 5mA collector current. Its measured power gain, NF, and input return loss at 2GHz are 16dB, 1.7dB, and -10dB, respectively. These values are not affected by the out-of-band source tuning. The measured S-parameters of the LNA are presented in Fig. IV.4.

Fig. IV.5 shows the LNA IIP_3 in dBm as a function of $\mathrm{Re}(Z_{\rm x}(\Delta\omega))$ and $\mathrm{Im}(Z_{\rm x}(2\omega))$ with two tones at 2GHz and 2.001GHz. The contours are computed from (IV.10), and the

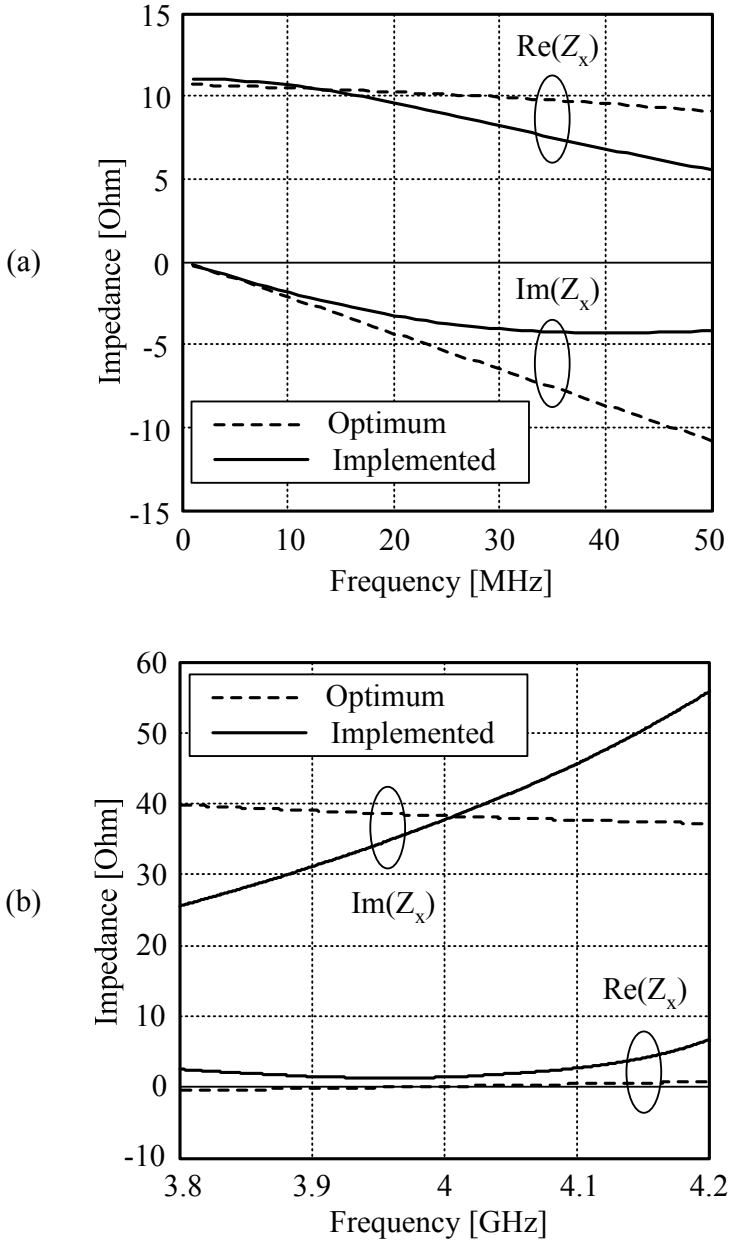

Figure IV.3: Implemented Z_{x} vs. desired $Z_{\mathrm{x,opt}}$ of the LNA in Fig. IV.2. (a) Near DC. (b) At the 2nd-harmonic frequency.

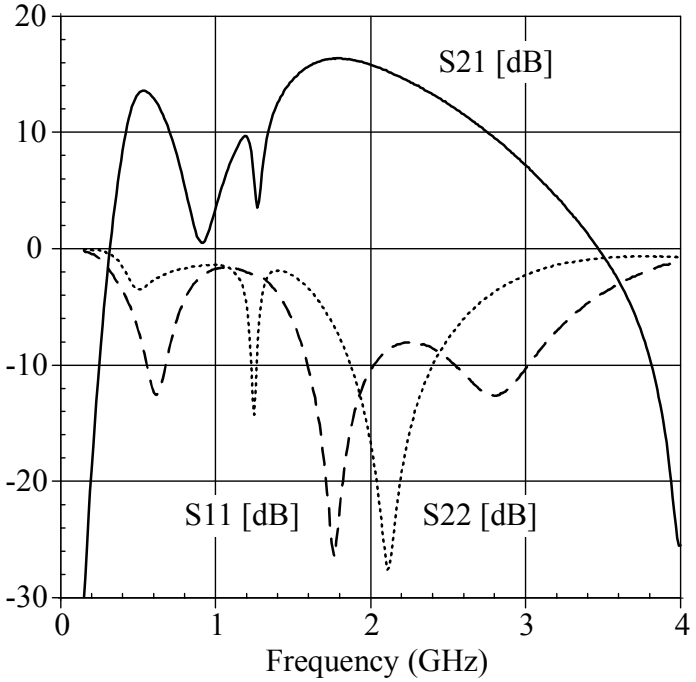

Figure IV.4: Measured S-parameters of the LNA in Fig. IV.2 vs. frequency.

discrete data points are the measured results. $\mathrm{Re}(Z_{\mathrm{x}}(\Delta\omega))$ was tuned by changing R_1, which also affected $\mathrm{Im}(Z_{\mathrm{x}}(\Delta\omega))$. Adjusting C_2 to tune $\mathrm{Im}(Z_{\mathrm{x}}(\Delta\omega))$ had a negligible impact on IIP_3 at Δf of 1MHz; therefore, C_2 was fixed. IIP_3 shown in Fig. IV.5 is the smaller of $\mathrm{IIP}_{3,2\omega_{\mathrm{a}}-\omega_{\mathrm{b}}}$ and $\mathrm{IIP}_{3,2\omega_{\mathrm{b}}-\omega_{\mathrm{a}}}$. The optimum combination of $\mathrm{Re}(Z_{\mathrm{x}}(\Delta\omega))$ and $\mathrm{Im}(Z_{\mathrm{x}}(2\omega))$ results in IIP_3 of approximately +16dBm, which is 14dB higher than IIP_3 of the same device biased at 5mA and terminated by non-optimum out-of-band impedances [43].

Figures IV.6 and IV.7 demonstrate the IIP_3 dependence on the two-tone spacing and center frequency with fixed matching networks. The tone spacing is varied in such a way that f_{a} is kept constant at 2GHz and f_{b} is changed. As can be seen, $\mathrm{IIP}_{3,2\omega_{\mathrm{a}}-\omega_{\mathrm{b}}}$ stays relatively constant with changing f_{b}, because the frequency of the 2nd harmonic responses contributing to $\mathrm{IIP}_{3,2\omega_{\mathrm{a}}-\omega_{\mathrm{b}}}$ does not change, and because, even though Δf changes, $Z_{\mathrm{x}}(\Delta\omega)$

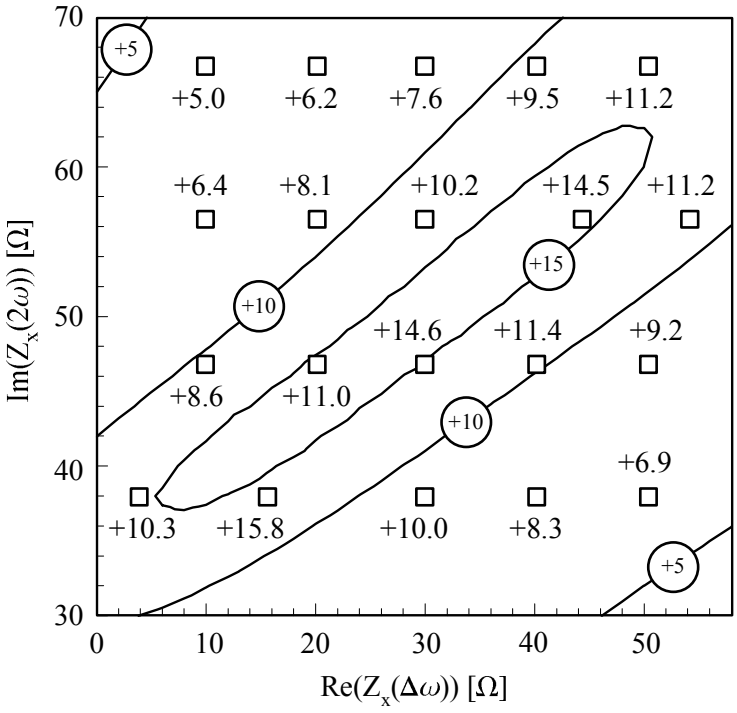

Figure IV.5: IIP_3 (in dBm) of the LNA in Fig. IV.2 vs. $\mathrm{Re}(Z_{\mathrm{x}}(\Delta\omega))$ and $\mathrm{Im}(Z_{\mathrm{x}}(2\omega))$. The contours are computed from (IV.10), and the discrete data points are measured.

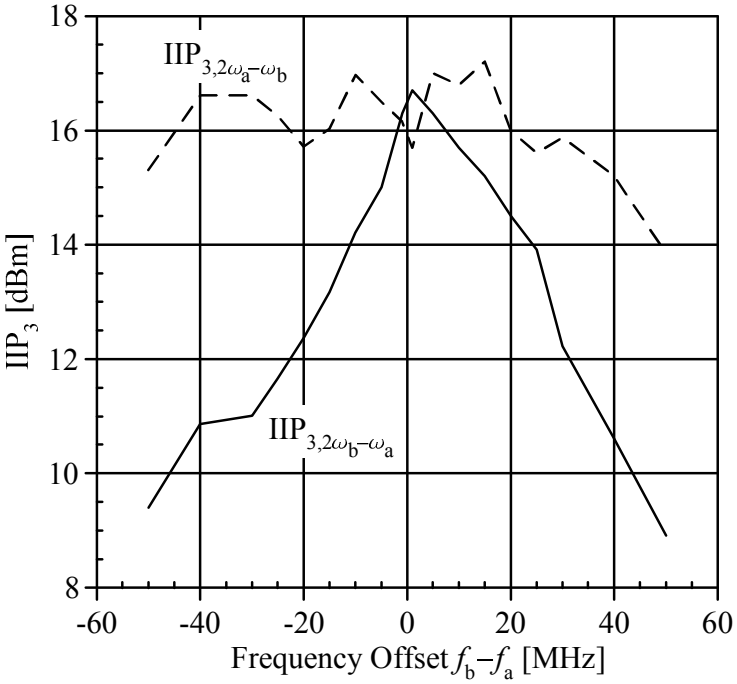

Figure IV.6: IIP_3 of the LNA in Fig. IV.2 as a function of the two-tone frequency spacing (f_a is fixed at 2GHz, and f_b is varied).

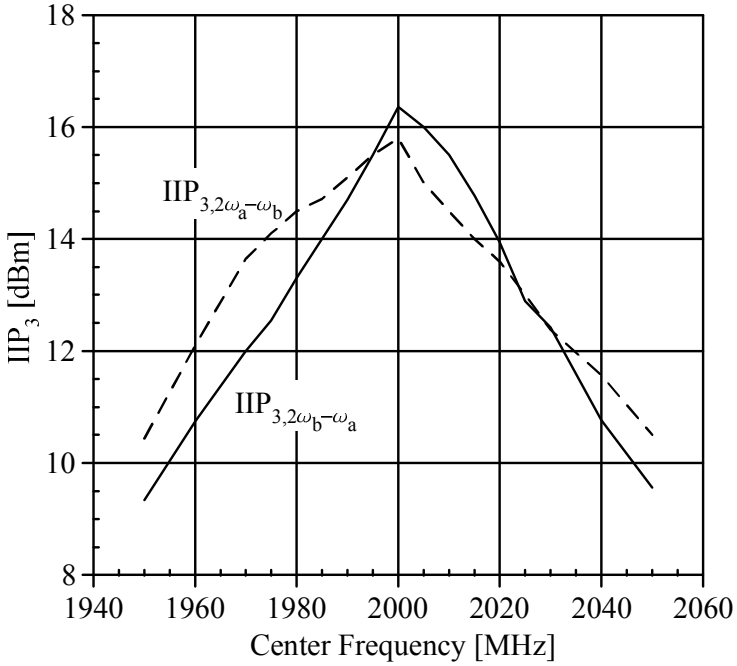

Figure IV.7: IIP_3 of the LNA in Fig. IV.2 as a function of the center frequency f_a ($f_\mathrm{b} = f_\mathrm{a} + 1\mathrm{MHz}$).

stays optimum. On the other hand, $\mathrm{IIP}_{3,2\omega_\mathrm{b}-\omega_\mathrm{a}}$ degrades noticeably at higher $|\Delta f|$, because, as the tone separation increases, f_b moves away from 2GHz and $Z_\mathrm{x}(2\omega_\mathrm{b})$ changes from optimum (see Fig. IV.3(b)). The corresponding 2nd-harmonic contribution to $\mathrm{IMD}_{3,2\omega_\mathrm{b}-\omega_\mathrm{a}}$ no longer cancels the remaining IMD_3 terms, resulting in lower $\mathrm{IIP}_{3,2\omega_\mathrm{b}-\omega_\mathrm{a}}$. For the same reason, IIP_3 drops as the center frequency of the two tones moves away from 2GHz as shown in Fig. IV.7. All presented IIP_3 values were measured at -24.5dBm input power per tone.

Measuring XMD is complicated by the somewhat high noise floor of a CDMA source, the phase noise of a jammer source, and the distortion introduced by a spectrum analyzer. Fig. IV.8 shows the test setup developed to overcome these difficulties. The combined CDMA and jammer signals are applied to the DUT input and subtracted from its output. The variable attenuator connected to the DUT output and the phase delay of the feed-forward network are tuned to cancel the jammer and the noise from the sources around it. The jammer cancellation allows the use of a high-linearity test LNA to bring the DUT XMD response above the spectrum analyzer noise floor without additional XMD in the test LNA and the spectrum analyzer. The feed-forward network is well isolated from the DUT signal path to prevent the XMD produced at the DUT input from coupling to the output through the feed-forward network, and to prevent the DUT output signal from coupling back to the input.

Fig. IV.9 shows two overlapped output spectra of the LNA driven by a jammer with P_j=-23dBm and a 1.23MHz-wide OQPSK CDMA signal with P_TX=-23dBm. The solid line is the output spectrum with the source impedance tuned according to Fig. IV.3, and

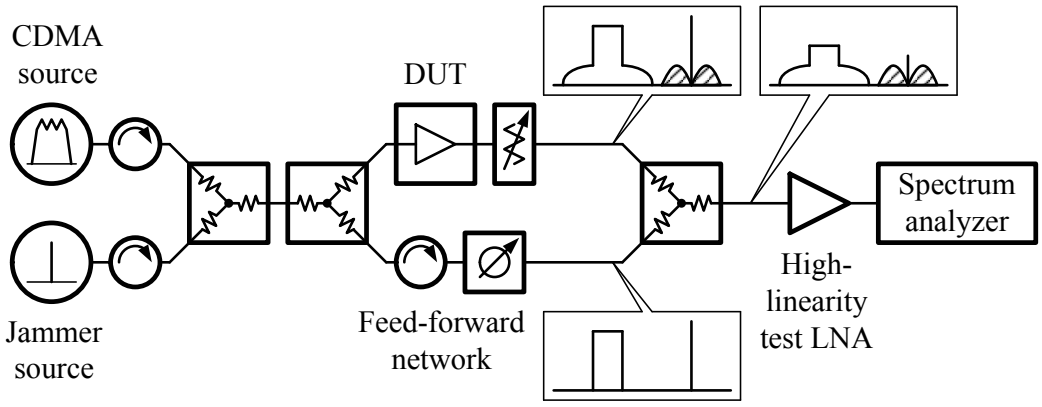

Figure IV.8: High-dynamic range test setup for measuring cross modulation distortion.

the dashed line is the output spectrum of the same LNA with R_1=10kΩ and R_2 adjusted such that the dc current is the same in both cases. As can be seen, the optimum out-of-band source tuning reduces XMD by almost 30dB for the given power levels. It also significantly reduces the spectral regrowth of the CDMA signal.

Fig. IV.10 shows the dependence of the output XMD power ($P_{\mathrm{XMD\_OUT}}$) on the input powers of the jammer and the CDMA signal. $P_{\mathrm{XMD\_OUT}}$ was measured 600kHz away from the jammer in a 10kHz band. With a non-optimum out-of-band source impedance, $P_{\mathrm{XMD\_OUT}}$ varies by 1dB per 1dB of the jammer power and by 2dB per 1dB of the CDMA signal power at low power levels. These slopes are due to the dominating 3rd-order nonlinearity. The described optimum out-of-band source tuning cancels this nonlinearity, and the resulting XMD is produced by higher odd-order nonlinearities. That is why the slopes of the XMD power in this case are steeper.

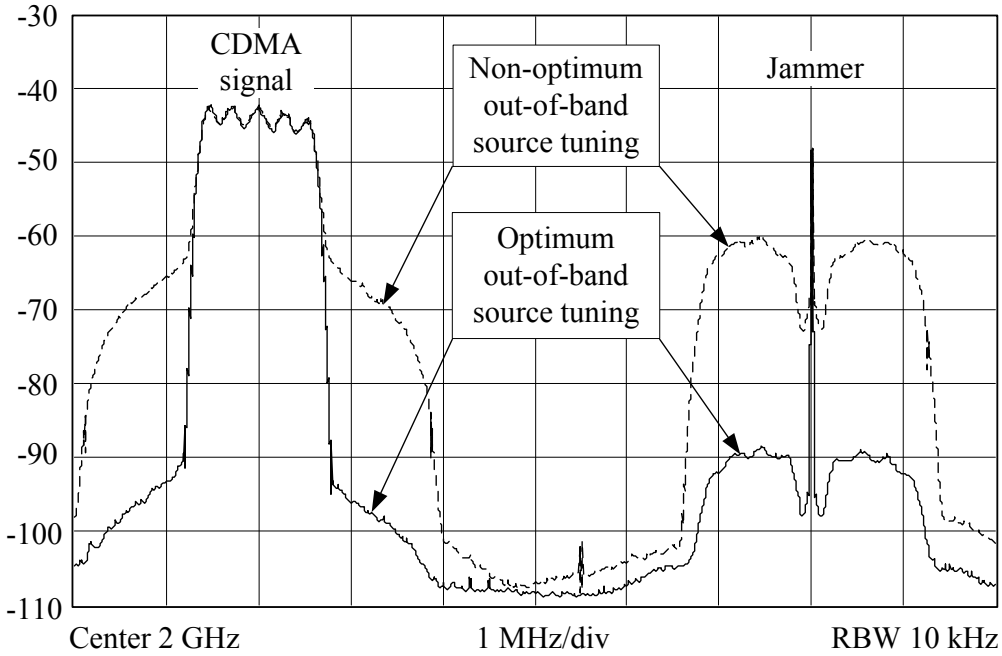

Figure IV.9: Measured output spectra of the LNA in Fig. IV.2 ($P_{\rm j} = P_{\rm TX} = -23$dBm). Note that the jammer is partially cancelled by the feedforward network.

IV.6 Theory of Low-Frequency Low-Impedance Input Termination Technique

Neglecting the base-collector capacitance C_μ, it can be shown that, if a BJT

1. is strongly degenerated such that

$$|Z_2(2\omega)| \gg \frac{1}{g_1}, \tag{IV.15}$$

2. its $f_{\rm T}$ is much larger than the 2nd-harmonic frequency of the input excitation, i.e.,

$$\frac{g_1}{C_{\rm je} + g_1\tau_{\rm F}} \gg 2\omega, \tag{IV.16}$$

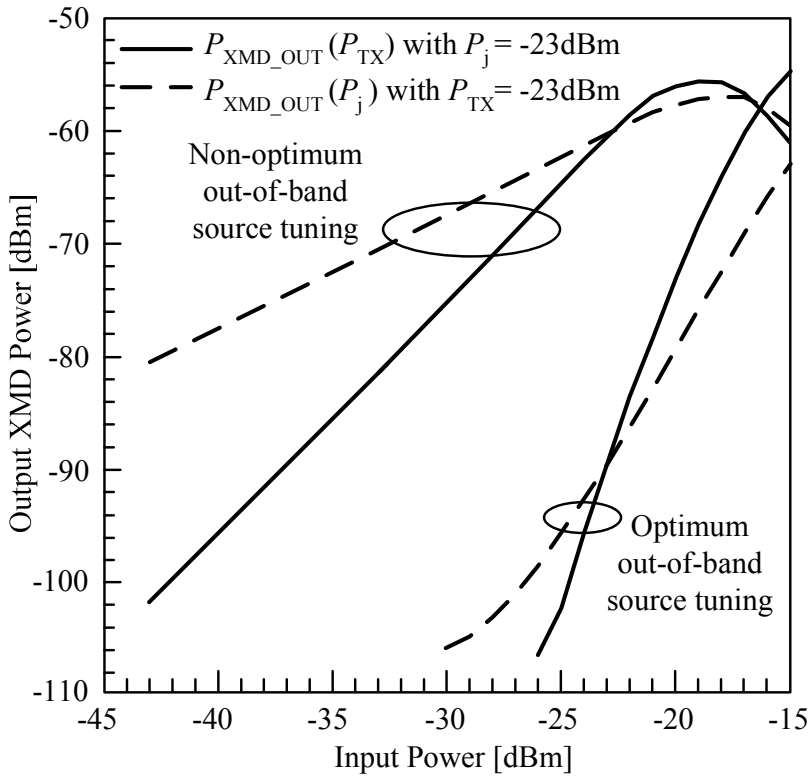

Figure IV.10: Output XMD power of the LNA in Fig. IV.2 ($P_{\mathrm{XMD\_OUT}}$) vs. input powers of the jammer (P_{j}) and the CDMA signal (P_{TX}).

3. and the driving impedance at the 2nd-harmonic frequency is fairly small such that

$$|Z_1(2\omega)| \ll |Z_2(2\omega)| \min\left(\beta_{\mathrm{F}}, \frac{\omega_{\mathrm{T}}}{2\omega}\right), \tag{IV.17}$$

then

$$|g(2\omega)| \ll g_1. \tag{IV.18}$$

The physical meaning of $g(2\omega)$ can be understood from equation (C.2a). At the 2nd-harmonic frequency 2ω, $v_{\mathrm{x}} = 0$ (no 2nd harmonics in the signal generator), and the equation simplifies to

$$v_\pi = -\frac{i_{\mathrm{c}}}{g(2\omega)}. \tag{IV.19}$$

Therefore, $g(2\omega)$ is equivalent to a negative transconductance, which relates the 2nd harmonic responses in v_π and i_{c}. Since the 2nd-harmonic responses originate in i_{c} (they are generated by the $g_2 v_\pi^2$ term of (IV.1)), $-1/g(2\omega)$ is a transfer function of the collector current at the 2nd-harmonic frequency to v_π.

With approximation (IV.18), (IV.11c) simplifies to

$$\varepsilon(\Delta\omega, 2\omega) \cong g_3 - \frac{4g_2^2}{3}\frac{1}{g_1 + g(\Delta\omega)} - \frac{2g_2^2}{3g_1}. \tag{IV.20}$$

Substituting (IV.4) into (IV.20), we find that the first and the last terms of (IV.20) cancel each other, resulting in

$$\varepsilon(\Delta\omega, 2\omega) = -\frac{I_{\mathrm{C}}^2}{3\phi_{\mathrm{t}}^4} \cdot \frac{1}{g_1 + g(\Delta\omega)}. \tag{IV.21}$$

Therefore, IMD_3 of a BJT satisfying conditions (IV.15)-(IV.17) is generated by the bias modulation at $\Delta\omega$. In the case of an inductive emitter degeneration, commonly used in

LNAs, assuming that the circuit reactances are negligible at $\Delta\omega$, we get

$$g(\Delta\omega) \approx \frac{1}{\left[Z_{\mathrm{x}}(\Delta\omega) + r_{\mathrm{b}}\right]/\beta_{\mathrm{F}} + r_2}, \tag{IV.22}$$

where r_2 is the real part of $Z_2(\Delta\omega)$. Substituting (IV.22) into (IV.21) and (IV.21) into (IV.10), we obtain

$$\mathrm{IIP}_3 \approx \frac{\dfrac{\phi_{\mathrm{t}}^4}{I_{\mathrm{C}}^2}\left|g_1 + \dfrac{1}{\left[Z_{\mathrm{x}}(\Delta\omega) + r_{\mathrm{b}}\right]/\beta_{\mathrm{F}} + r_2}\right|}{2\mathrm{Re}(Z_1(\omega))\left|H(\omega)\right|\left|A_1(\omega)\right|^3}. \tag{IV.23}$$

According to (IV.23), the IIP_3 of a common-emitter BJT depends on the source impedance at the difference frequency in such a way that reducing $Z_{\mathrm{x}}(\Delta\omega)$ results in a higher IIP_3. Since negative real values of $Z_{\mathrm{x}}(\Delta\omega)$ make the BJT unstable, the minimum useful value of $Z_{\mathrm{x}}(\Delta\omega)$ is 0Ω, in which case IIP_3 is maximum. Minimizing the base termination impedance of an inductively degenerated common-emitter stage at the tone separation frequency $\Delta\omega$ is the essence of the low-frequency low-impedance input termination technique. Minimizing r_{b} and r_2 also results in a higher IIP_3. In the case of $Z_{\mathrm{x}}(\Delta\omega) = r_{\mathrm{b}} = r_2 = 0$, there are no difference-frequency responses in the base and emitter voltages; thus, there is no bias modulation at $\Delta\omega$, and IMD_3 is zero.

According to (IV.23), to prevent $Z_{\mathrm{x}}(\Delta\omega)$ from being a limiting factor of IIP_3, its target value should be much less than r_{b} or $\beta_{\mathrm{F}} r_2$, whichever is larger. BJTs used in LNAs are designed to have very low r_{b}'s (typically in the range 5-10Ω) to reduce their noise contribution. Resistance r_2 includes the intrinsic emitter resistance r_{e}, which is typically of the order of 0.2Ω, and the extrinsic dc resistance of a degeneration inductor. The latter resistance depends on the implementation of the degeneration inductor and can range from 0.1Ω for a bondwire or microstrip inductor to approximately 1Ω for a 2nH on-chip inductor.

Therefore, with a typical $\beta_{\rm F}$ of about 100 and on-chip inductive degeneration, $\beta_{\rm F} r_2$ can be as high as 120Ω, making r_2 a limiting factor of IIP$_3$. The target value of $Z_{\rm x}(\Delta\omega)$ should then be of the order of $r_{\rm b}$, i.e., less than 10Ω.

There are several techniques to reduce the BJT intrinsic base and emitter resistances to achieve a higher IIP$_3$. The simplest ones are to select a larger total emitter length and to use two base fingers for each emitter finger in an interdigitated multi-finger BJT. The latter technique is often called double-sided base contact and is used to reduce the base spreading resistance. The device technology can also be optimized. For example, adding Ge to the p-Si base of a transistor reduces the bandgap across the base, offering a lower barrier for electron injection into the base and, thus, a higher $\beta_{\rm F}$. The latter can be traded off against a lower $r_{\rm b}$ by increasing the base doping. Grading the Ge doping profile creates a strong electric field between the emitter and collector junctions, which reduces the base transit time and, thus, increases $f_{\rm T}$. A higher $f_{\rm T}$ makes the conditions (IV.16) and (IV.17) more easily satisfied.

It should be emphasized that (IV.23) was derived in this section for a strongly-degenerated BJT operating at a frequency well below its $f_{\rm T}$ and terminated at the input with a relatively small impedance at the 2nd-harmonic frequency. Under these conditions, the contribution of the 3rd-order nonlinearity to IMD$_3$ cancels that due to mixing of the 2nd harmonics with the fundamental responses, and IMD$_3$ is generated entirely by the bias modulation at $\Delta\omega$. The resulting IIP$_3$ is then fairly insensitive to the 2nd-harmonic termination impedance as long as the latter is relatively low. This impedance can be forced to

be close to zero by connecting a shunt LC trap with a resonant frequency of 2ω [55]. In a more general case, $Z_{\rm x}(2\omega)$ can be optimally tuned together with $Z_{\rm x}(\Delta\omega)$ to achieve a precise cancellation of the distortions generated by the 2nd and 3rd-order $i_{\rm c}$ nonlinearities, resulting in a much higher IIP_3, as was shown in the previous section.

IV.7 Methods for Generating Low-Frequency Low-Impedance Input Termination

There are three commonly-used methods to generate a low-frequency low-impedance input termination. They are summarized in Fig. IV.11. In the LC traps shown in Fig. IV.11(a), (b), and (c), the low impedance is presented to the base of a BJT at Δf thanks to a large-value capacitor C. The inductor L can be either an RF choke or a matching inductor. The capacitor value should be large enough to generate the desired low impedance at the lowest frequency affecting XMD (285kHz in cellular-band receivers and 635kHz in PCS-band receivers). Such a capacitor increases the LNA gain switching time, which is critical in CDMA applications. For example, 10Ω at 285kHz is generated by a 56nF capacitor. If the bias resistor is 1kΩ (an even higher value resistor is preferred to reduce its noise contribution), the time constant of charging or discharging C is 56μs. Therefore, the LNA gain switching time is expected to be at least 168μs, i.e., approximately three times the time constant. For voice communications, the LNA gain switching time should be at most 100μs, whereas high-data rate applications require this time to be less than 10μs. There-

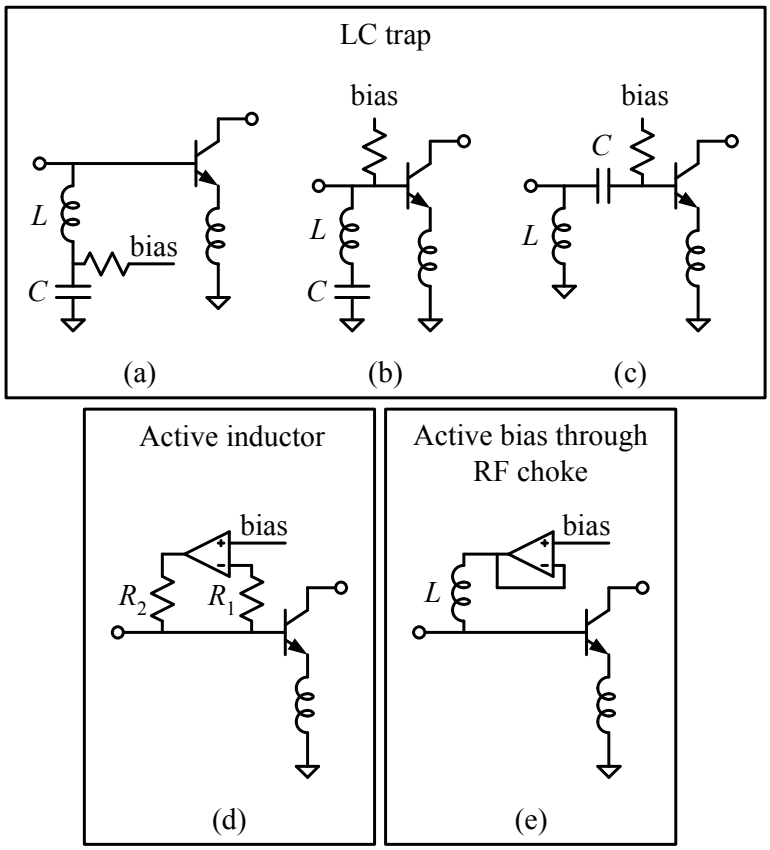

Figure IV.11: Methods for generating a low-frequency low-impedance input termination.

fore, the requirement of the LNA gain switching time forces the selection of C with a value lower than needed for the low-frequency termination, resulting in a higher XMD. If the gain switching speed is not critical, the LC trap is a very attractive and commonly-used method due to its simplicity and negligible effect on the LNA gain, NF, and stability [43], [46]-[48].

The gain switching time can be reduced without increasing the low-frequency terminating impedance by using an active inductor bias shown in Fig. IV.11(d) [44], [49], [55]. The bias circuit uses an operational amplifier with a negative resistive feedback and can generate a very low impedance down to dc. The feedback resistors R_1 and R_2 isolate the

opamp input and output from the LNA input at the fundamental frequency. The major challenge of the active inductor design is to ensure that the opamp has a high enough gain at the highest frequency affecting the LNA XMD (the separation frequency of the TX and RX channels) to provide a low-impedance termination at that frequency and has a low enough gain at the fundamental frequency to prevent it from shorting the LNA input. Mathematically, this challenge can be explained as follows. Assuming that the open-loop opamp has a zero output impedance, the output impedance of the closed-loop opamp in Fig. IV.11(d), looking from the LNA input, is given by

$$Z_{\mathrm{out}}(\omega) = \frac{R_2}{1 + A(\omega)}, \tag{IV.24}$$

where $A(\omega)$ is the open-loop gain of the opamp. It should be noted that, if the input matching circuit presents a much higher impedance at $\Delta\omega$ than $Z_{\mathrm{out}}(\Delta\omega)$, which is usually the case, then $Z_{\mathrm{x}}(\Delta\omega) \approx Z_{\mathrm{out}}(\Delta\omega)$, i.e., the low-frequency low-impedance input termination is set entirely by the opamp.

Assuming that $|A(\Delta\omega)| \gg 1$ and $|A(\omega_0)| \ll 1$, where ω_0 is the operating (fundamental) frequency of the LNA, we get

$$Z_{\mathrm{out}}(\Delta\omega) \approx \frac{R_2}{A(\Delta\omega)}, \tag{IV.25a}$$

$$Z_{\mathrm{out}}(\omega_0) \approx R_2. \tag{IV.25b}$$

The condition $|A(\omega_0)| \ll 1$ is necessary for the opamp to have a high output impedance at the operating frequency. Let the target value of $|Z_{\mathrm{out}}(\Delta\omega)|$ to be at most 10Ω to provide a sufficiently low-impedance termination for a high IIP_3. And let $Z_{\mathrm{out}}(\omega_0)$ to be at least

1kΩ to prevent it from shunting the RF signal path and from producing an excessive noise. Then,

$$\frac{|Z_{\rm out}(\omega_0)|}{|Z_{\rm out}(\Delta\omega)|} \approx |A(\Delta\omega)| > 100. \tag{IV.26}$$

To satisfy the condition $|A(\omega_0)| \ll 1$, we will require $|A(\omega_0)|$ to be at most 0.1. Then,

$$\frac{|A(\Delta\omega)|}{|A(\omega_0)|} > 1000. \tag{IV.27}$$

If the open-loop gain of the opamp slopes down between Δf and f_0 at the rate of 20dB per decade, then the maximum Δf at which $Z_{\rm out}$ is less than the targeted 10Ω is $f_0/1000$ or approximately 0.9MHz for f_0 in the cellular band and 2MHz for f_0 in the PCS band. To extend Δf to the separation frequency of the TX and RX channels, $f_{\rm TX-RX}$ ($f_{\rm TX-RX}$=45MHz for a cellular transceiver and $f_{\rm TX-RX}$=80MHz for a PCS transceiver), which also affects XMD, the opamp open-loop gain at $f_{\rm TX-RX}$ must be increased to 40dB without reducing its attenuation at the operating frequency f_0. This can only be done by moving the 2nd pole of the opamp below f_0 to increase the slope of $|A(\omega)|$ to 40dB/decade. However, even if the gain slope from $f_{\rm TX-RX}$ to f_0 is 40dB/decade and $|A(\omega_0)| = 0.1$, the gain at $f_{\rm TX-RX}$ is only 31.7dB for the cellular operating frequency band and 35.6dB for the PCS operating frequency band. Besides, the 2nd pole located below the unity gain frequency of the opamp results in its instability with the closed loop. Therefore, the active inductor termination method requires a compromise between the bandwidth of the low-frequency low-impedance termination, NF, gain, and stability of the LNA. Since NF, gain, and stability are critical, the bandwidth of the low-frequency low-impedance termination is typically sacrificed, resulting in a higher XMD.

To increase the bandwidth of the low-frequency low-impedance termination, an RF choke can be added between the closed-loop opamp output and the LNA input as shown in Fig. IV.11(e) [52], [53], [121], [134]. In this case, the output impedance of the closed-loop opamp can be made as low as possible in a very wide frequency range without restrictions on its value at the operating frequency f_0, provided that the RF choke gives enough isolation at this frequency. Assuming that the output impedance of the closed-loop opamp is much smaller than the impedance of the RF choke L, we can write

$$Z_{\text{out}}(\Delta\omega) \approx j\Delta\omega L, \tag{IV.28a}$$

$$Z_{\text{out}}(\omega_0) \approx j\omega_0 L. \tag{IV.28b}$$

Therefore,

$$\frac{Z_{\text{out}}(\omega_0)}{Z_{\text{out}}(\Delta\omega)} \approx \frac{\omega_0}{\Delta\omega} > 100, \tag{IV.29}$$

i.e., the maximum Δf, at which the desired low-impedance termination is generated, is 10 times higher than in the case of the active inductor bias. It can further be increased if the RF choke is chosen such that its self-resonant frequency is close to f_0.

Using an RF choke in combination with a closed-loop opamp to bias the LNA input as shown in Fig. IV.11(d) provides the widest bandwidth of the low-frequency low-impedance termination without affecting the LNA gain, NF, and stability. Since there is no need for a large value capacitor in the input matching circuit, the gain can be switched very fast. This is the approach we used to design a cellular-band SiGe HBT LNA.

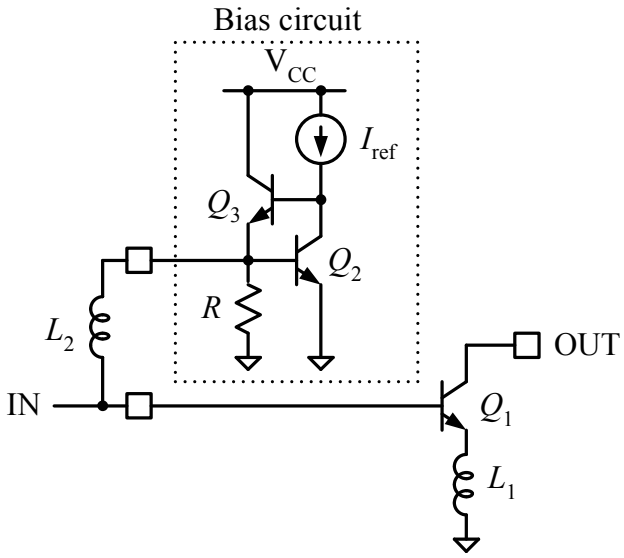

Figure IV.12: Simplified schematic diagram of the cellular-band SiGe HBT LNA.

IV.8 Cellular-Band SiGe HBT LNA Design and Measured Results

A simplified schematic diagram of the designed cellular-band LNA is shown in Fig. IV.12. The LNA was manufactured in a 0.5um SiGe BiCMOS technology. Q_1 is the main amplifying transistor, degenerated by the on-chip inductor L_1. The bias circuit consists of a current mirror Q_2 with a beta helper Q_3. It is connected to the LNA input through an external RF choke L_2. Due to the negative feedback through Q_3 and a high dc voltage gain of Q_2, the output impedance of the bias circuit is very low within the 3dB bandwidth of Q_2. At these frequencies, L_2 is almost a dc short, and the LNA input is terminated by the bias circuit output impedance and the output impedance of the antenna duplexer. For many ceramic and SAW cellular duplexers, their RX port impedance below 500MHz can

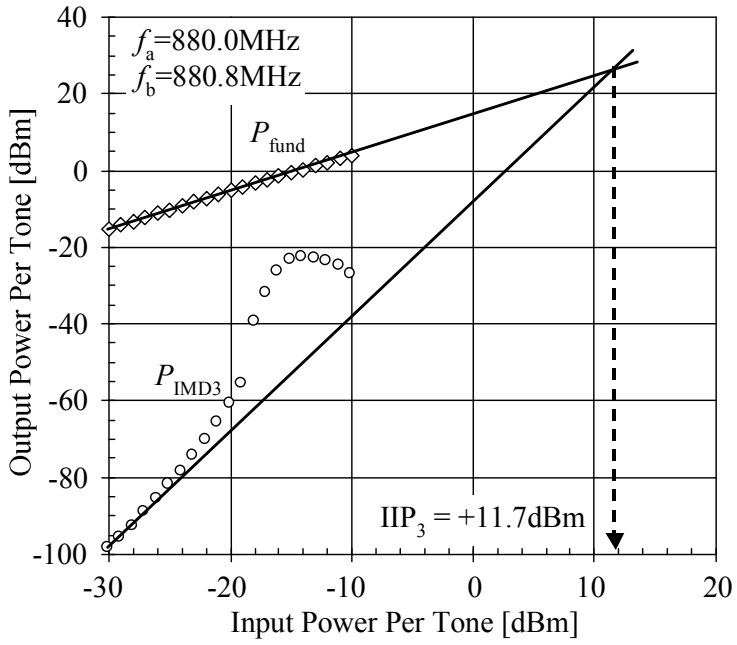

Figure IV.13: Measured 2-tone transfer characteristics of the LNA in Fig. IV.12.

be accurately modeled by a shunt 8-10pF capacitance. This capacitance controls the location of the non-dominant pole of the bias circuit. To make the bias circuit as broadband as possible (to cover 45MHz) without reducing its phase margin, the non-dominant pole is pushed to higher frequencies by selecting a fairly large dc current through Q_3. The LNA also has a low gain mode implemented by bypassing Q_2 through a FET switch, which is not shown in Fig. IV.12.

The measured LNA gain and NF are 15.7dB and 1.4dB, respectively, and the current consumption is 3.9mA without the bias circuit and 5.4mA with the bias circuit from 3V supply. The gain switching time is less than 1us. The measured fundamental and IMD$_3$ output powers as functions of the input power are plotted in Fig. IV.13. As can be seen, the LNA achieves +11.7dBm IIP$_3$ for the input power levels below -25dBm.

To compare the LNAs in Figures IV.2 and IV.12 with other state-of-the-art LNAs using bipolar transistors, we will use the dynamic range figure of merit (FOM) defined as [135]

$$\mathrm{FOM} = \frac{G \cdot \mathrm{IIP}_3}{(F-1)P_{\mathrm{dc}}}, \tag{IV.30}$$

where G is the power gain ($G \cdot \mathrm{IIP}_3 = \mathrm{OIP}_3$), F is the noise factor ($F = 10^{\mathrm{NF}/10}$), and P_{dc} is the dc power consumption. Table IV.1 summarizes the performances of our and other state-of-the-art BJT LNAs. As can be seen, the LNA in Fig. IV.2 has the highest FOM.

Table IV.1: Comparison of state-of-the-art linear BJT LNAs

LNA	Technology	Freq GHz	S21 dB	NF dB	IIP_3 dBm	P_{dc} mA@V	FOM
LNA in Fig. IV.2	Discrete Si BJT	2	16	1.7	+16	5@2.7	245
LNA in Fig. IV.12	0.5μm SiGe HBT	0.9	15.7	1.4	+11.7	3.9@3	123
[136]	0.18μm SiGe HBT	0.9	15.4	0.95	+10.5	6@2.78	95.4
[135]	0.5μm SiGe HBT	0.9	15	1.4	+12	8@3	54.9
[56]	0.25μm Si BJT	0.9	15.5	1	+9	7.7@2.7	52.4
[136]	0.18μm SiGe HBT	1.9	16.5	1.1	+8.5	7.6@2.78	51.9
[48]	Discrete SiGe HBT	1.9	14.7	1	+10.3	8.9@3	43.8
[54]	SiGe HBT	2.1	16	1.2	+8.4	8@3	36.1
[135]	0.5μm SiGe HBT	1.9	12.5	1.3	+10	7.5@3	22.6
[47]	0.5μm SiGe HBT	1.9	15.3	1.9	+7.6	6.5@2.7	20.2
[137]	0.25μm Si BJT	0.9	13	1.4	+9.3	12.9@3	11.5
[138]	0.5μm SiGe HBT	2.5	12	1.6	+8	7.5@2.75	10.9
[49]	0.4μm Si BJT	1.9	9.4	2.5	+12.5	12.8@2.7	5.8

IV.9 Conclusions

We have shown that the difference-frequency and 2nd harmonic terminations significantly affect IMD_3 of common-emitter circuits due to the contribution of the 2nd-order nonlinearity to IMD_3. These terminations can be optimized simultaneously to achieve a precise cancellation of the distortions generated by the 2nd and 3rd-order nonlinearities, resulting in a very high IIP_3. To the author's knowledge, from the point of view of the dynamic-range FOM, the reported discrete Si BJT LNA has the best performance among the state-of-the-art LNAs utilizing bipolar transistors. However, the measured IIP_3 is very sensitive to variations in the tone frequencies. It is feasible to achieve a very high IIP_3 for a wide range of these frequencies by designing the out-of-band terminations to maintain their optimum values for a wide range of the corresponding difference and 2nd-harmonic frequencies.

We have also shown that, for a strongly-degenerated BJT operating at a frequency well below its f_{T} and terminated at the input with a relatively small impedance at the 2nd-harmonic frequency, IMD_3 is generated entirely by the bias modulation at the difference frequency. In this case, IIP_3 can be effectively increased by terminating the base with a low-impedance at low frequencies. We reviewed several known methods to generate a low-frequency low-impedance input termination and concluded that only the combination of the low-impedance bias circuit with an RF choke can meet the CDMA LNA requirements to the bandwidth of the termination and to the gain switching time. The demonstrated SiGe HBT LNA performance is inferior only to our discrete Si BJT LNA performance, but

still meets the derived IIP_3 and NF requirements. The low-frequency low-impedance input termination technique is well suited for high-volume production because it does not rely on the optimum 2nd-harmonic tuning, which causes the sensitivity to the tone frequencies.

Chapter V

Optimum Gate Biasing

V.1 Introduction

As was shown in the previous chapter, the linearity of a Si BJT or a SiGe HBT can be reliably improved by terminating the base with a low impedance at low frequencies. Unfortunately, this technique is not suitable for linearizing FETs because they have a negative 3rd-order derivative of the transfer characteristic at typical biases. Nevertheless, there is a strong interest in implementing CDMA RX front ends in Si CMOS technology due to its lower cost than Si or SiGe BiCMOS technologies. Si CMOS already proved its capability to deliver a low NF and a high gain with low dc current consumption at RF [139]. However, without special techniques, the linearity of CMOS LNAs is unsuitable for CDMA applications unless a large dc current is consumed [24].

As was mentioned in Chapter I, a FET can be linearized by biasing it at a gate-source voltage ($V_{\rm GS}$) at which the 3rd-order derivative of its dc transfer characteristic $I_{\rm D}(V_{\rm GS})$ is zero. One of the major drawbacks of this technique is that a significant $\rm IIP_3$ improvement occurs in a very narrow $V_{\rm GS}$ range (about 10-20mV) around the optimum voltage, and there are no known bias means to automatically generate this voltage. Therefore, a bias

circuit has to be manually tuned to this voltage, which makes IIP_3 to vary significantly with process and temperature variations.

This chapter first explains the dc theory of the optimum gate biasing technique. A novel bias circuit is proposed to automatically generate the gate bias voltage at which $\partial^3 I_{\rm D}/\partial {V_{\rm GS}}^3$ is zero. Its sensitivity to mismatches between FETs is analyzed. Then, the Volterra Series analysis of a common-source FET is used to explain the effect of the circuit reactances on the IMD_3 null at RF. An approach to increase the peak IIP_3 in the presence of these reactances is proposed. A 0.25μm CMOS LNA using this approach is described. The effect of the optimum gate bias on the LNA gain and NF is explained. The LNA measured results are presented to confirm the developed theory.

V.2 DC Theory of Optimum Gate Biasing

Consider a common-source FET biased in saturation. Its small-signal output current can be expanded into the following power series in terms of the small-signal gate-source voltage $v_{\rm gs}$ around the bias point

$$i_{\rm d}(v_{\rm gs}) = g_1 v_{\rm gs} + g_2 v_{\rm gs}^2 + g_3 v_{\rm gs}^3 + \cdots \ , \tag{V.1}$$

where g_1 is the small-signal transconductance and the higher-order coefficients (g_2, g_3 etc.) define the strengths of the corresponding nonlinearities. Among these coefficients, g_3 is particularly important because it controls IMD_3 at low signal levels and, thus, determines

IIP_3. The input tone amplitude at the intercept point is given by [35]

$$A_{\text{IP3}} = \sqrt{\frac{4}{3}\left|\frac{g_1}{g_3}\right|} \quad [\text{V}]. \tag{V.2}$$

The power series coefficients generally depend on the dc gate-source and drain-source voltages V_{GS} and V_{DS}. However, the dependence on V_{DS} for a FET in saturation can be neglected. Then the coefficients of (V.1) can be found as

$$g_1(V_{\text{GS}}) = \frac{\partial I_{\text{D}}}{\partial V_{\text{GS}}}, \tag{V.3a}$$

$$g_2(V_{\text{GS}}) = \frac{1}{2}\frac{\partial^2 I_{\text{D}}}{\partial V_{\text{GS}}^2} = \frac{1}{2}\frac{\partial g_1(V_{\text{GS}})}{\partial V_{\text{GS}}}, \tag{V.3b}$$

$$g_3(V_{\text{GS}}) = \frac{1}{6}\frac{\partial^3 I_{\text{D}}}{\partial V_{\text{GS}}^3} = \frac{1}{3}\frac{\partial g_2(V_{\text{GS}})}{\partial V_{\text{GS}}}. \tag{V.3c}$$

To demonstrate the dependence of the power series coefficients on V_{GS}, they were extracted from the measured $I_{\text{D}}(V_{\text{GS}})$ characteristic of the 350μm/0.25μm n-channel FET (NFET) used in the LNA described later in this chapter. Fig. V.1(a) plots the square root of the measured I_{D} as a function of V_{GS} with $V_{\text{DS}} = 1.2$V. The straight dashed line fitted to the curve in the strong inversion region is used to find the boundaries between different regions of the transistor operation. Computing g_2 and g_3 directly from the measured discrete data points results in unacceptably large errors. Instead, the following highly-accurate semi-empirical continuous model was fitted to the measured transfer characteristic first

$$I_{\text{D}}(V_{\text{GS}}) = \frac{K}{2}\frac{f^2(V_{\text{GS}})}{1 + \theta f(V_{\text{GS}}) + \vartheta f^2(V_{\text{GS}})}, \tag{V.4}$$

where $f(V_{\text{GS}})$ is the binding function of the subthreshold and strong inversion regions, given by [28]

$$f(V_{\text{GS}}) = 2\eta\phi_{\text{t}} \ln\left(1 + e^{(V_{\text{GS}} - V_{\text{TH}})/(2\eta\phi_{\text{t}})}\right). \tag{V.5}$$

Above, K is the transconductance parameter, $V_{\rm TH}$ is the threshold voltage, $\phi_{\rm t}$ is the thermal voltage kT/q, and η is the subthreshold slope factor. Parameters θ and ϑ model the source series resistance, mobility degradation due to the vertical field, and short-channel effects such as velocity saturation. The extracted parameters are summarized in Table V.1. After

Table V.1: Extracted $I_{\rm D}(V_{\rm GS})$ model parameters

Parameter	Value	Units
K	0.414248760	A/V^2
$V_{\rm TH}$	0.557108490	V
$2\eta\phi_{\rm t}$	0.070651626	V
θ	1.398562014	1/V
ϑ	0.632848540	1/V^2

the above model was fitted to the measured data, the power series coefficients were computed as its derivatives, and $A_{\rm IP3}$ was calculated using (V.2). The results are presented in Fig. V.1(b) and (c), respectively. As expected, in the strong inversion region, the FET operates close to an ideal square-law device with the current dominated by drift. The mobility reduction due to the vertical field and velocity saturation deviates the dc transfer characteristic from a square-law behavior (the effect of the denominator in (V.4)), causing gain compression, which is indicated by negative g_3. In the weak inversion region, the current is mainly due to diffusion, which leads to its exponential dependence on $V_{\rm GS}$. As a result, g_3 is positive in this region, causing gain expansion. In the moderate inversion region, both drift and diffusion comparably contribute to the current. At some bias voltage, the gain expansion due to the diffusion component of the current cancels the gain compression due to the mobility reduction on the drift component, and FET behaves as an ideal square-law device with $g_3 = 0$ and $A_{\rm IP3} = \infty$ (in reality, however, the contribution of the 5th and

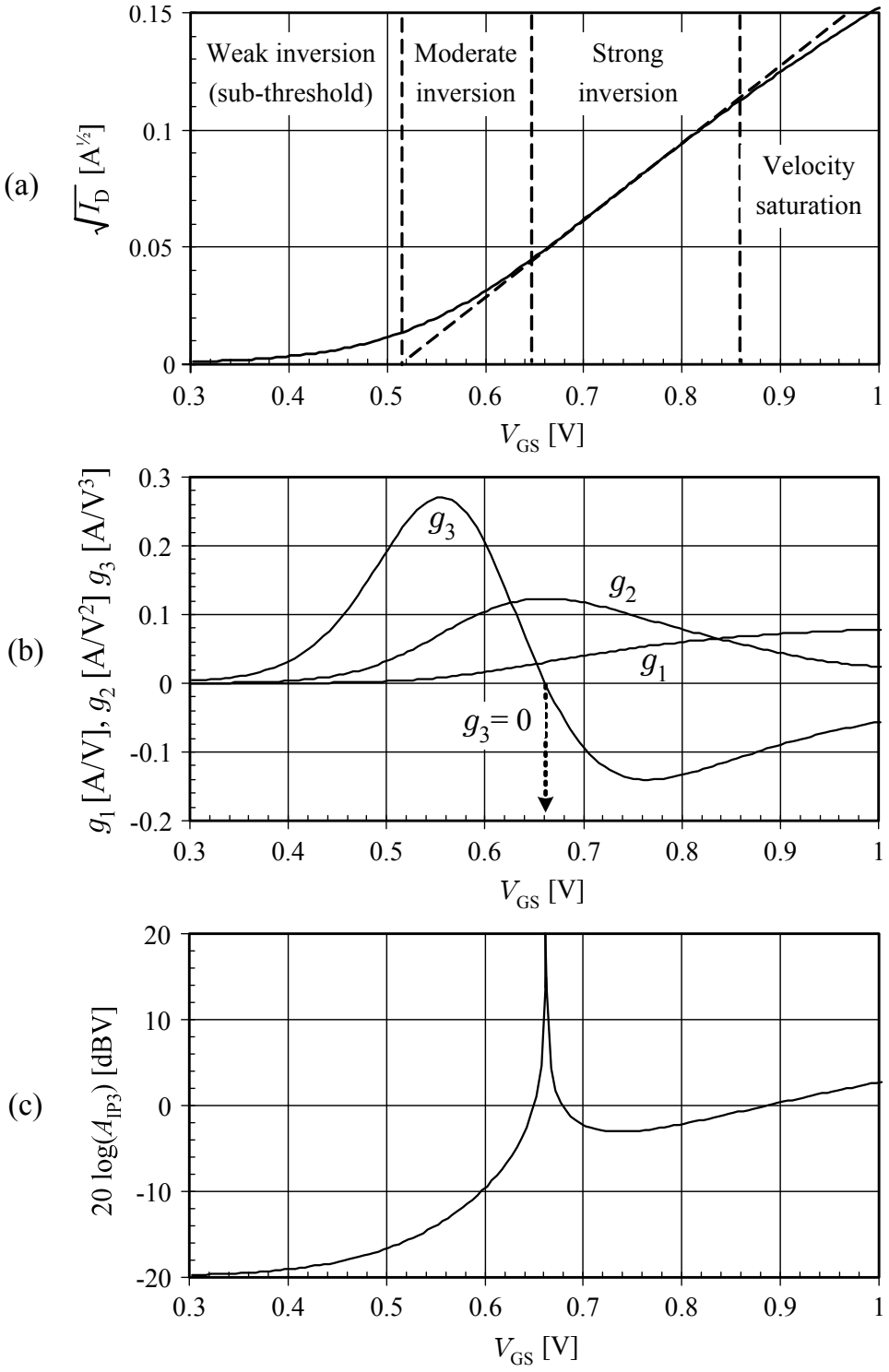

Figure V.1: 350μm/0.25μm NFET. (a) Measured dc transfer characteristic ($V_{\rm DS} = 1.2$V). (b) Power series coefficients computed from the fitting model (V.4). (c) Theoretical $A_{\rm IP3}$ computed using (V.2).

higher odd-order nonlinearities to IMD_3 limit A_{IP3}). This cancellation happens for only one specific voltage, making the peak in A_{IP3} very narrow and, thus, requiring an accurate gate bias within ± 10mV of the optimum voltage. Manually tuned bias circuits are not capable of such precision in the presence of process and temperature variations.

V.3 Bias Circuit for Zero g_3

In order for a bias circuit to generate and automatically maintain the bias voltage for zero g_3, it should produce a dc voltage or current proportional to g_3 and have a dc feedback to set it to zero. The insight into how to design such a bias circuit can be gained if equations (V.3a)-(V.3c) are rewritten in terms of small deviations of the dc voltages and currents:

$$g_1(V_{\text{GS}}) = \frac{I_{\text{D}}(V_{\text{GS}} + \Delta V/2) - I_{\text{D}}(V_{\text{GS}} - \Delta V/2)}{\Delta V}, \tag{V.6a}$$

$$\begin{aligned} g_2(V_{\text{GS}}) &= \frac{g_1(V_{\text{GS}} + \Delta V/2) - g_1(V_{\text{GS}} - \Delta V/2)}{2\Delta V} \\ &= \frac{I_{\text{D}}(V_{\text{GS}} + \Delta V) + I_{\text{D}}(V_{\text{GS}} - \Delta V) - 2I_{\text{D}}(V_{\text{GS}})}{2\Delta V^2}, \end{aligned} \tag{V.6b}$$

$$\begin{aligned} g_3(V_{\text{GS}}) &= \frac{g_2(V_{\text{GS}} + \Delta V/2) - g_2(V_{\text{GS}} - \Delta V/2)}{3\Delta V} \\ &= \frac{1}{6\Delta V^3}\left[I_{\text{D}}(V_{\text{GS}} + 3\Delta V/2) + 3I_{\text{D}}(V_{\text{GS}} - \Delta V/2)\right. \\ &\qquad \left. -3I_{\text{D}}(V_{\text{GS}} + \Delta V/2) - I_{\text{D}}(V_{\text{GS}} - 3\Delta V/2)\right]. \end{aligned} \tag{V.6c}$$

If the term in the brackets of (V.6c) is zero, then g_3=0. The bias circuit that generates this term and automatically tunes V_{GS} for zero g_3 is shown in Fig. V.2 [140]. NFETs M_1-M_4 are scaled versions of the main transistor (not shown). They are built of the same unit cells. M_2 and M_3 have three times more unit cells than M_1 and M_4. M_1 generates the first current in

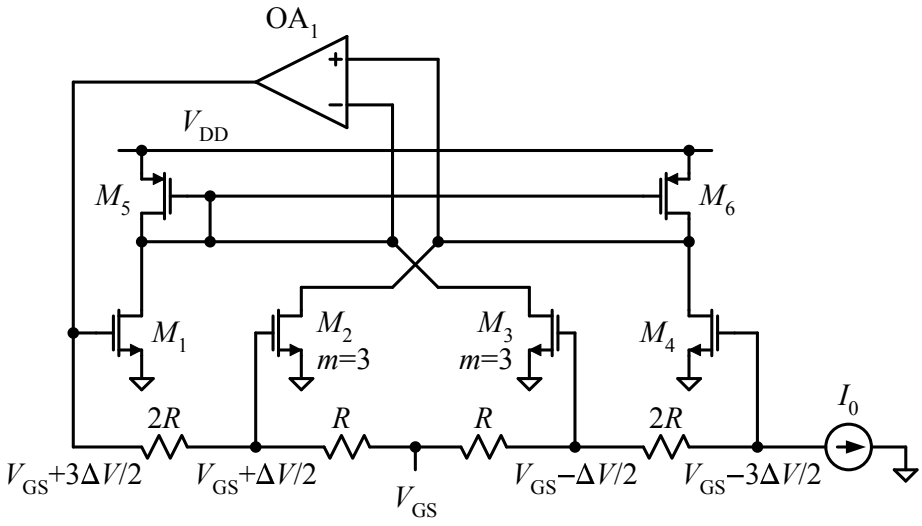

Figure V.2: Bias circuit for zero g_3.

the brackets of (V.6c). M_2 generates three times the third current. M_3 generates three times the second current, and M_4 generates the fourth current. The currents of M_1 and M_3 (as well as M_2 and M_4) are added by connecting their drains together. The common drains are biased through the current mirror M_5/M_6, where M_5 and M_6 are p-channel FETs of equal size. If the drain voltages of M_5 and M_6 are equal, their currents are equal, and the term in the brackets of (V.6c) is zero. This balance is ensured by the operational amplifier OA_1, which senses the difference between the drain voltages and generates the input voltage for the resistor chain $2R/R/R/2R$, creating a feedback loop. The generated bias voltage for the main NFET is tapped at the center of the resistor chain.

The polarity of the OA_1 input connections has to be chosen correctly to ensure that the bias circuit settles to the desired optimum bias voltage. If the combined drain current of NFETs M_1 and M_3 is higher than that of M_2 and M_4, g_3 is positive according to (V.6c). The positive g_3 means that V_{GS} is below the optimum bias voltage for zero g_3 and has to be

increased to reach this voltage, according to Fig. V.1(b). Therefore, the common drain of M_1 and M_3 has to be connected to the inverting input of OA_1, as shown in Fig. V.2.

If the described bias circuit starts up with M_1-M_4 in the triode region, it can latch up in a wrong state. This latching is possible because a FET has another zero crossing in $g_3(V_{\rm GS})$ at $V_{\rm GS}$ exceeding $V_{\rm DS} + V_{\rm TH}$ as shown in Fig. V.3. If, at the start up, the generated $V_{\rm GS}$ is above the second zero crossing, the output voltage of OA_1 will keep increasing until the latter saturates. To prevent this latching, the bias circuit can be modified as shown in Fig. V.4, where the gate of M_5 is disconnected from its drain and operational amplifier OA_2 is added to generate the gate bias of M_5 and M_6 such that the common drain of M_1 and M_3 is at a reference voltage $V_{\rm ref}$. To prevent M_1 and M_3 from going into the triode region, the maximum output voltage of OA_1 must be limited to the values close to $V_{\rm ref}$.

V.4 Precision of the Bias Circuit for Zero g_3

The deviation of $V_{\rm GS}$ produced by the bias circuit in Fig. V.4 from the target optimum voltage for zero g_3 is a function of mismatches between M_1-M_4 and the approximation error of (V.6c) due to nonzero ΔV (=$2I_0R$). The generated $V_{\rm GS}$ is fairly insensitive to the value of ΔV as indicated in Fig. V.5. However, it is very sensitive to mismatches between M_1-M_4. Its deviation from the optimum bias is maximum if the currents of M_1 and M_3 shift together in one direction and those of M_2 and M_4 shift together in the opposite direction. For simplicity, we will assume that M_1 is matched to M_3 and M_2 to M_4, which is the worst case scenario. Then, (V.6c) can be modified to take into account the transconductance

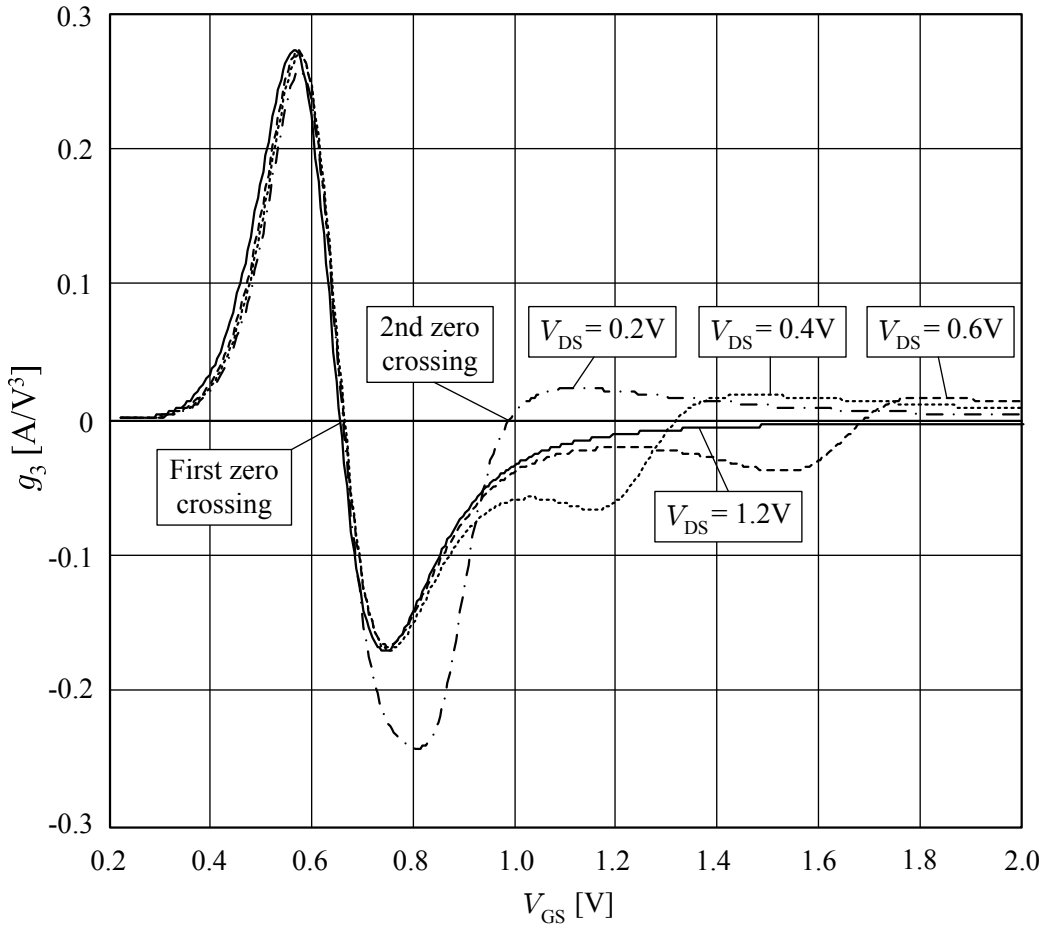

Figure V.3: Simulated g_3 versus V_{GS} for different V_{DS}. Note the presence of the second zero crossing.

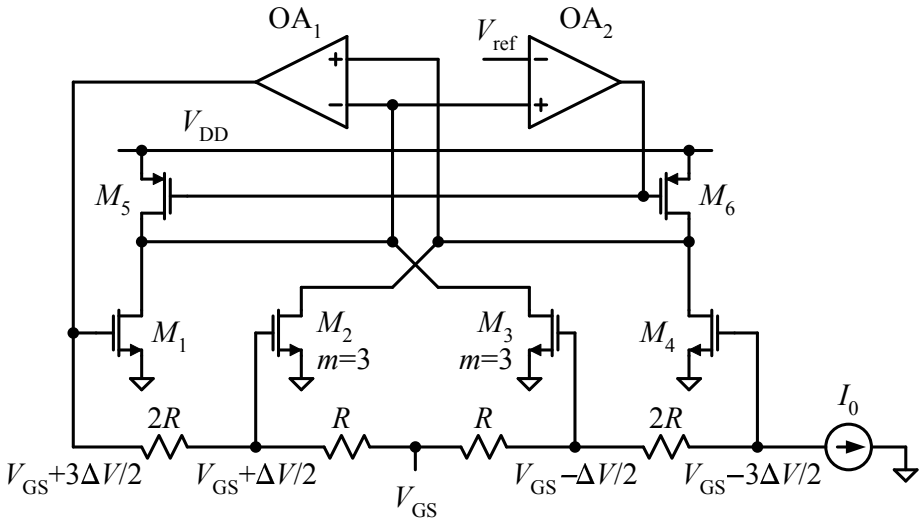

Figure V.4: Bias circuit for zero g_3 with an improved tolerance to latching.

parameter and threshold voltage mismatches between M_1/M_3 and M_2/M_4 as follows

$$g_3(V_{\rm GS}) = \frac{1}{6\Delta V^3}\left\{\left(1+\frac{\Delta K}{2K}\right)\left[I_{\rm D}\left(V_{\rm GS}+\frac{3\Delta V}{2}+\frac{\Delta V_{\rm TH}}{2}\right)\right.\right.$$
$$\left.+3I_{\rm D}\left(V_{\rm GS}-\frac{\Delta V}{2}+\frac{\Delta V_{\rm TH}}{2}\right)\right]$$
$$-\left(1-\frac{\Delta K}{2K}\right)\left[3I_{\rm D}\left(V_{\rm GS}+\frac{\Delta V}{2}-\frac{\Delta V_{\rm TH}}{2}\right)\right.$$
$$\left.\left.+I_{\rm D}\left(V_{\rm GS}-\frac{3\Delta V}{2}-\frac{\Delta V_{\rm TH}}{2}\right)\right]\right\}, \qquad \text{(V.7)}$$

where ΔK and $\Delta V_{\rm TH}$ are the transconductance parameter and threshold voltage mismatches, respectively. Using the fitting model (V.4)-(V.5) for $I_{\rm D}(V_{\rm GS})$, the above equation can be numerically solved for $V_{\rm GS}$ that gives $g_3 = 0$. This $V_{\rm GS}$ is equal to 0.66V. The deviation of $V_{\rm GS}$ generated by the bias circuit in Fig. V.4 from the target 0.66V as a function of the transconductance parameter and threshold voltage mismatches is plotted in Fig. V.6. Positive $\Delta K/K$ and $\Delta V_{\rm TH}$ correspond to a higher current of M_1/M_3 than that of M_2/M_4. As can be seen, a lower current of M_1/M_3 compensates for the systematic error in $V_{\rm GS}$ due

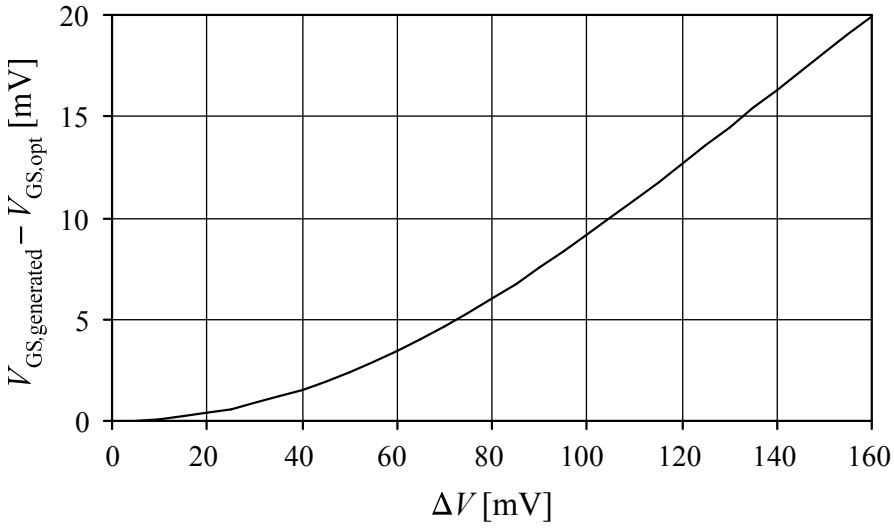

Figure V.5: Predicted deviation of the generated V_{GS} in Fig. V.4 from the optimum voltage for zero g_3 as a function of ΔV.

to ΔV.

Assuming that the FETs are adjacent to each other, the dependence of their mismatch on distance can be neglected. Then, the standard deviations of the differences in the transconductance parameters and the threshold voltages between M_1/M_3 and M_2/M_4 can be respectively estimated as [141]

$$\sigma_{\Delta K/K} \approx \frac{A_K}{\sqrt{W L_{\mathrm{g}} n_{\mathrm{f}}}} \quad [\%] \tag{V.8}$$

and

$$\sigma_{\Delta V_{\mathrm{TH}}} \approx \frac{A_{V_{\mathrm{TH}}}}{\sqrt{W L_{\mathrm{g}} n_{\mathrm{f}}}} \quad [\mathrm{mV}], \tag{V.9}$$

where A_K and $A_{V_{\mathrm{TH}}}$ are the proportionality constants in units of %μm and mV$\cdot\mu$m, respectively, W is the gate finger width in μm, L_{g} is the gate length in μm, and n_{f} is the total number of gate fingers in M_1 and M_3 (or M_2 and M_4). The constant A_K is fairly independent of process scaling and is approximately 2%μm for NFETs [142], and the benchmark

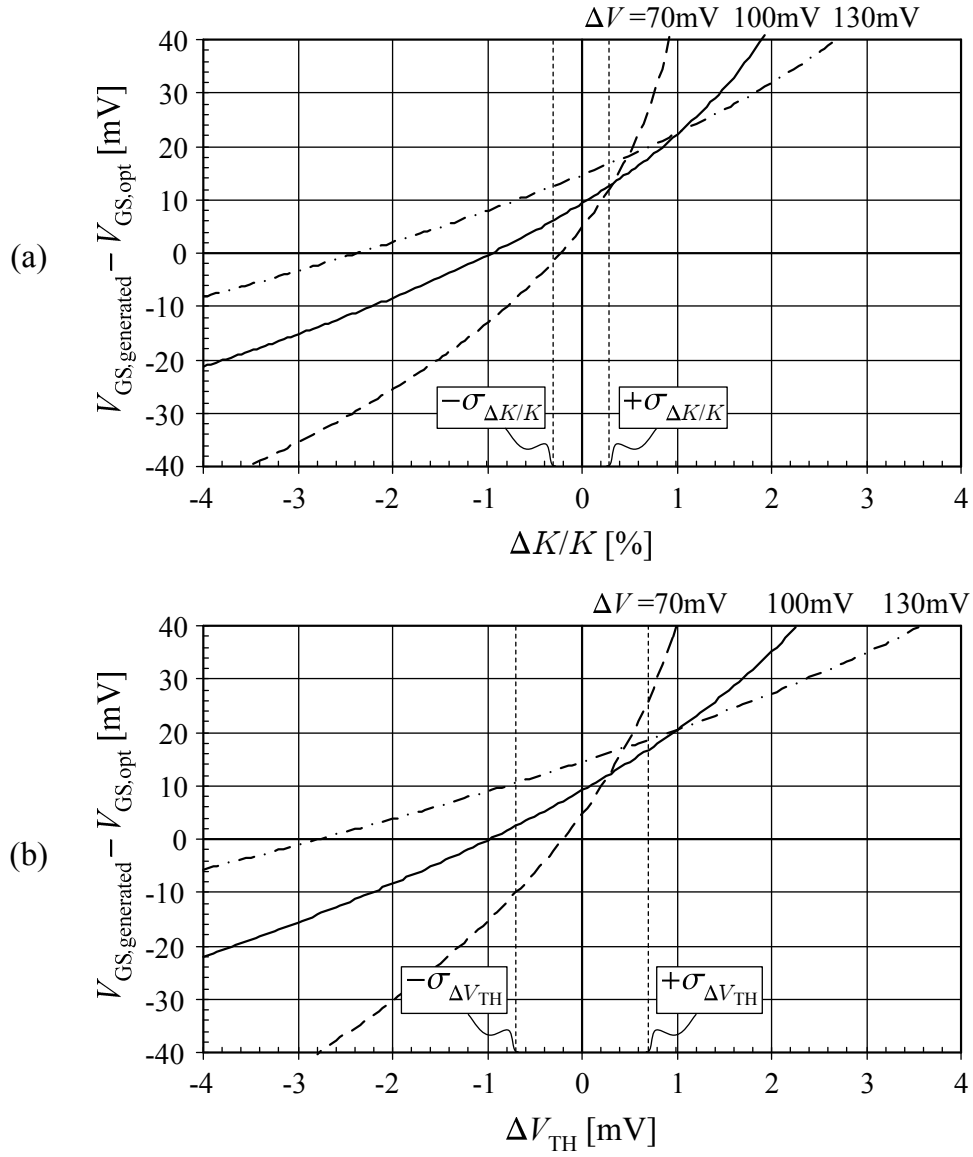

Figure V.6: Predicted deviation of the generated V_{GS} from the optimum bias voltage for zero g_3. (a) As a function of $\Delta K/K$ with ΔV_{TH}=0mV. (b) As a function of ΔV_{TH} with $\Delta K/K$=0%.

value for $A_{V_{\rm TH}}$ is 1mVμm per 1nm of the gate oxide thickness [143]. For the 0.25μm CMOS process used to manufacture the LNA described later in this chapter, the gate oxide thickness is 5nm, and, therefore, $A_{V_{\rm TH}} = 5$mVμm. With $W = 10\mu$m, $L_{\rm g} = 0.25\mu$m, and $n_{\rm f} = 20$, we get $\sigma_{\Delta K/K} = 0.28\%$ and $\sigma_{\Delta V_{\rm TH}} = 0.71$mV. As can be seen from Fig. V.6, to minimize the $V_{\rm GS}$ error within 2-3 times the calculated standard deviations, ΔV should be approximately 100mV. This error is still larger than the $V_{\rm GS}$ range within which a significant $\rm IIP_3$ improvement occurs (see Fig. V.1(c)). The $V_{\rm GS}$ error can further be reduced by increasing the total gate area of M_1-M_4 or by selecting a process with thinner gate oxide or both.

V.5 RF Theory of Optimum Gate Biasing

Consider a small-signal nonlinear equivalent circuit of a common-source FET in saturation shown in Fig. V.7, where $Z_{\rm x}$ is the output impedance of the signal generator, Z_1 is the impedance presented to the FET gate following the $Z_{\rm x}$ transformation by the matching circuit and package parasitics, Z_3 is the drain load impedance, and L is the source degeneration inductance. In this equivalent circuit, we made the following simplifying assumptions:

1. The body effect is negligible, i.e., $g_{\rm mb} \approx 0$.

2. The FET gate-drain and source-bulk capacitances, $C_{\rm gd}$ and $C_{\rm sb}$, are zero, and the gate-bulk capacitance $C_{\rm gb}$ is absorbed into Z_1. Neglecting $C_{\rm gd}$ is the crudest as-

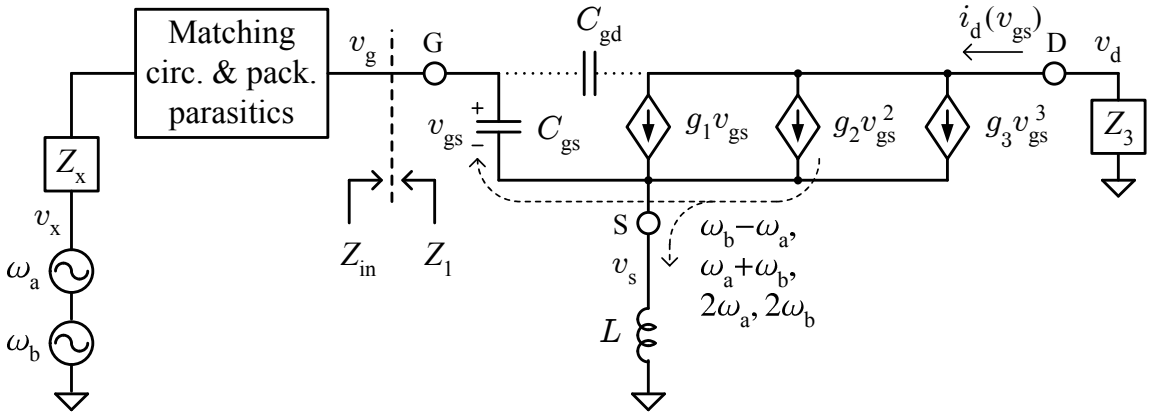

Figure V.7: Small-signal nonlinear equivalent circuit of a common-source FET.

sumption here, because, as indicated in Fig. V.8, $C_{\rm gd}$ is only 1.8 times smaller than $C_{\rm gs}$, while other capacitances are more than 7 times smaller than $C_{\rm gs}$ in the strong inversion and velocity saturation regions.

3. $C_{\rm gs}$ is bias independent, i.e., linear. This assumption is only valid in the strong inversion and velocity saturation regions. As can be seen from Fig. V.8, $C_{\rm gs}$ strongly depends on $V_{\rm GS}$ in the moderate inversion region.

4. The FET gate and source series resistances and the dc resistance of the degeneration inductor are zero. However, the effect of the total dc source resistance on the dc drain current can be included in the power series coefficients g_1, g_2, and g_3.

5. The FET output conductance is infinite, i.e., there is no channel length modulation.

6. The input signal is very weak such that the drain current nonlinearities of the order higher than three are negligible. This assumption is typical for low noise amplifiers because they operate far below their 1dB compression point.

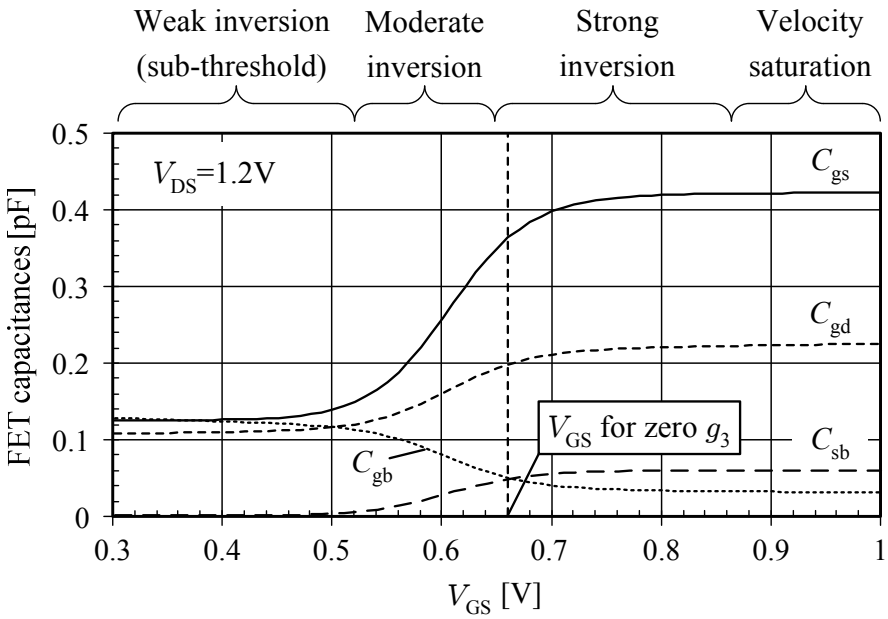

Figure V.8: Simulated capacitances of a 350μm/0.25μm NFET.

In this *weakly nonlinear* case, IMD_3 would be generated entirely by the $g_3 v_{\text{gs}}^3$ component of the drain current if L was zero. The source degeneration inductance creates a feedback path for the drain current to v_{gs}. This feedback is particularly strong for high frequency spectral components of i_{d}. For example, the 2nd harmonics generated by $g_2 v_{\text{gs}}^2$ are fed back across the gate and source, adding to the fundamental components of v_{gs}. These spectral components are then mixed in $g_2 v_{\text{gs}}^2$ to produce the responses at $2\omega_{\text{a}} \pm \omega_{\text{b}}$ and $2\omega_{\text{b}} \pm \omega_{\text{a}}$. This is one of mechanisms by which the 2nd-order nonlinearity of i_{d} contributes to IMD_3.

The Volterra Series result for IIP_3 (IV.10), derived for a common-emitter BJT driven by two tones at ω_{a} and ω_{b}, can be reused for the circuit in Fig. V.7 if β_{F} is made infinite, τ_F and C_μ are made zero, C_{je} is replaced with C_{gs}, and $Z_2(\omega)$ is replaced with $j\omega L$. To simplify these results further, we will assume that

- the tone separation $\Delta\omega$ ($= \omega_{\rm b} - \omega_{\rm a}$) is much smaller than the tone frequencies $\omega_{\rm a}$ and $\omega_{\rm b}$ such that $\omega_{\rm a} \approx \omega_{\rm b} \approx \omega$ and $j\Delta\omega L \approx 0$, and

- the signal generator is conjugately matched to the FET input at the fundamental frequency of the input tones, i.e.,

$$Z_1(\omega) = Z_{\rm in}^*(\omega) = g_1\frac{L}{C_{\rm gs}} - j\omega L - \frac{1}{j\omega C_{\rm gs}}. \tag{V.10}$$

With these substitutions and assumptions, we get

$$\mathrm{IIP}_3 = \frac{4g_1^2\omega^2 L C_{\rm gs}}{3|\varepsilon(2\omega)|}, \tag{V.11}$$

where

$$\varepsilon(2\omega) = g_3 - \frac{2g_2^2/3}{g_1 + \dfrac{1}{j2\omega L} + j2\omega C_{\rm gs} + Z_1(2\omega)\dfrac{C_{\rm gs}}{L}}. \tag{V.12}$$

As can be seen from (V.11) and (V.12), making g_3 zero by biasing a FET at the optimum $V_{\rm GS}$ does not result in an infinite IIP_3 as it did at low frequencies (see Fig. V.1) due to the second term in (V.12). This term represents the contribution of the 2nd-order nonlinearity to IMD_3. As expected, this contribution depends on the degeneration inductance L and becomes zero with $L \to 0$. It also depends on the impedance presented to the gate at the 2nd harmonic frequency, $Z_1(2\omega)$, since the latter determines the amount of the 2nd-harmonic current flowing through $C_{\rm gs}$. Making $Z_1(2\omega)$ infinite reduces this current to zero and eliminates the 2nd-order contribution to IMD_3 within the made assumption that $C_{\rm gd} = 0$. The presence of $C_{\rm gd}$ however still allows the 2nd-harmonic current flow through $C_{\rm gs}$.

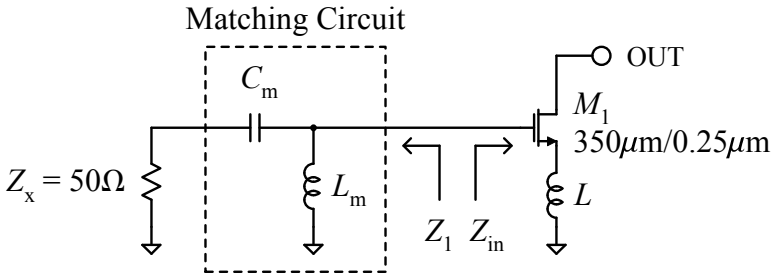

Figure V.9: Input matching used to evaluate (V.11).

To quantify the effect of the 2nd-order contribution on IIP_3, we have to assume a certain input matching circuit topology, which affects $Z_1(2\omega)$. We will neglect the package parasitics and C_{gb}, which was earlier assumed to be lumped into Z_1. For a wide range of FET biases and degeneration inductances, the matching circuit in Fig. V.9 would always provide a power match of the LNA input (however, for NF considerations other matching topologies may be preferred). Defining the normalized real and imaginary parts of $Z_1(\omega)$, given by (V.10), as

$$r_1 = \frac{1}{50}\mathrm{Re}(Z_1(\omega)) = \frac{1}{50} g_1 \frac{L}{C_{\mathrm{gs}}}, \tag{V.13a}$$

$$x_1 = \frac{1}{50}\mathrm{Im}(Z_1(\omega)) = \frac{1}{50}\left(-\omega L + \frac{1}{\omega C_{\mathrm{gs}}}\right), \tag{V.13b}$$

we get the following expressions for the matching components in Fig. V.9:

$$C_{\mathrm{m}} = \frac{1}{50\omega}\sqrt{\frac{r_1}{r_1^2 + x_1^2 - r_1}}, \tag{V.14a}$$

$$L_{\mathrm{m}} = 50\,\frac{x_1 - \sqrt{r_1(r_1^2 + x_1^2 - r_1)}}{\omega(1 - r_1)}. \tag{V.14b}$$

Then, $Z_1(2\omega)$ can be computed as

$$Z_1(2\omega) = \left[\left(50 + \frac{1}{j2\omega C_{\mathrm{m}}}\right)^{-1} + \frac{1}{j2\omega L_{\mathrm{m}}}\right]^{-1}. \tag{V.15}$$

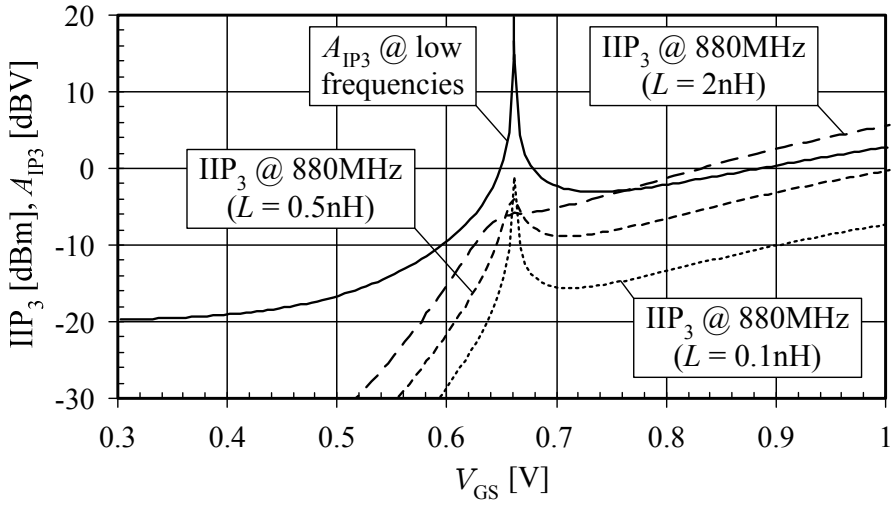

Figure V.10: Theoretical IIP_3 of the matched FET in Fig. V.9 with the neglected C_{gd}.

Substituting (V.15) into (V.12) and the latter into (V.11), we can compute IIP_3 as a function of the gate bias voltage and the source degeneration inductance. The results are presented in Fig. V.10. As can be seen, the 2nd-order contribution to IMD_3 due to the source degeneration inductance L significantly suppresses the high-frequency IIP_3 peaking at the optimum V_{GS}. In fact, for realistic values of the degeneration inductance (≥ 0.5nH), biasing at this voltage provides almost no IIP_3 improvement over the higher voltage biases.

V.6 Reducing Second Order Contribution

In order to understand how to cancel the 2nd-order contribution and achieve a significant IIP_3 improvement at the optimum bias, we need to include C_{gd} into our analysis. Reusing the Volterra Series result (IV.10) for the case $\beta_{\mathrm{F}} = \infty$, $\tau_{\mathrm{F}} = 0$, $C_{\mathrm{je}} = C_{\mathrm{gs}}$, and $C_{\mu} = C_{\mathrm{gd}}$, we get the following expression for IIP_3 of a common-source FET, represented

by the equivalent circuit in Fig. V.7:

$$\mathrm{IIP}_3 = \frac{1}{6\mathrm{Re}(Z_1(\omega))|H(\omega)||A_1(\omega)|^3|\varepsilon(2\omega)|}, \tag{V.16a}$$

where

$$H(\omega) = \frac{1 + j\omega C_{\mathrm{gs}}[Z_1(\omega) + j\omega L] + j\omega C_{\mathrm{gd}} Z_1(\omega)}{g_1 - j\omega C_{\mathrm{gd}}\left[1 + j\omega L(g_1 + j\omega C_{\mathrm{gs}})\right]}, \tag{V.16b}$$

$$A_1(\omega) = \frac{1}{g_1 + g(\omega)} \cdot \frac{1 + j\omega C_{\mathrm{gd}} Z_3(\omega)}{Z(\omega)}, \tag{V.16c}$$

$$\varepsilon(2\omega) = g_3 - \frac{2g_2^2/3}{g_1 + g(2\omega)}, \tag{V.16d}$$

$$g(\omega) = \frac{1 + j\omega C_{\mathrm{gs}}[Z_1(\omega) + Z(\omega)] + j\omega C_{\mathrm{gd}}[Z_1(\omega) + Z_3(\omega)]}{Z(\omega)}, \tag{V.16e}$$

$$Z(\omega) = j\omega L + j\omega C_{\mathrm{gd}}\left\{j\omega L[Z_1(\omega) + Z_3(\omega)] + Z_1(\omega)Z_3(\omega)\right\}. \tag{V.16f}$$

Here, as before, we neglected the dependence of IIP_3 on $\Delta\omega$ ($\Delta\omega = \omega_{\mathrm{b}} - \omega_{\mathrm{a}}$) assuming that the latter is much smaller than ω ($\omega \approx \omega_{\mathrm{a}} \approx \omega_{\mathrm{b}}$).

The equation of interest here is (V.16d). To cancel the 2nd-order contribution, the second term of (V.16d) should be set to zero. This requires $g(2\omega)$ to be infinite, which can only happen if $Z(2\omega) = 0$ according to (V.16e). If C_{gd} were zero as one of the assumption in the last section called for, making $L = 0$ would have resulted in zero $Z(2\omega)$ according to (V.16f), and the 2nd-order contribution would have been cancelled. It is no longer the case in the presence of C_{gd}.

The second term of (V.16d) can be zeroed by tuning the FET terminal impedances Z_1 and Z_3 at the 2nd-harmonic frequency. To find their optimum values, we will set the right

side of (V.16f) to zero at the 2nd-harmonic frequency and solve it for $Z_3(2\omega)$. The result is

$$R_{3,\mathrm{opt}} = -\frac{L}{C_{\mathrm{gd}}}\frac{R_1(1+4\omega^2 LC_{\mathrm{gd}})}{R_1^2+(X_1+2\omega L)^2}, \tag{V.17a}$$

$$X_{3,\mathrm{opt}} = \frac{L}{C_{\mathrm{gd}}}\frac{(X_1+2\omega L)(1-2\omega C_{\mathrm{gd}}X_1)-2\omega C_{\mathrm{gd}}R_1^2}{R_1^2+(X_1+2\omega L)^2}, \tag{V.17b}$$

where R and X with subscripts respectively denote the real and imaginary parts of the corresponding impedances at the 2nd-harmonic frequency. Equation (V.17a) shows that, for a finite $Z_1(2\omega)$ with a positive real part, the real part of $Z_3(2\omega)$ must be negative for $Z(2\omega)$ to be zero and the 2nd-order contribution to be cancelled. Such a value of $Z_3(2\omega)$ will result in potential instability of the amplifier and, therefore, must be avoided. However, if the input matching circuit is designed such that $|Z_1(2\omega)| = \infty$, then

$$Z_{3,\mathrm{opt}}(2\omega) = -j2\omega L. \tag{V.18}$$

Such a value for $Z_{3,\mathrm{opt}}(2\omega)$ is expected. With an infinite $Z_1(2\omega)$, the 2nd-harmonic current does not flow through C_{gs} and C_{gd} if the drain and source voltages have the same amplitude and phase at the 2nd-harmonic frequency. Because the source is terminated with $j2\omega L$, and because the current into the drain termination $Z_3(2\omega)$ is 180° apart from the current into the source termination, the optimum $Z_3(2\omega)$ must be equal to $-j2\omega L$.

In practice, it is impossible to generate infinite $Z_1(2\omega)$ due to limited Q-factors of reactive components. To estimate the effect of a finite $Z_1(2\omega)$ on IIP_3 of a FET with $Z_3(2\omega) = -j2\omega L$, we will assume that $Z_1(2\omega)$ is generated by a parallel RLC tank with a resonant frequency of 2ω. This tank is connected in series with the signal generator such that $Z_1(2\omega) \approx R_1$, where R_1 is the equivalent parallel resistance of the tank, representing

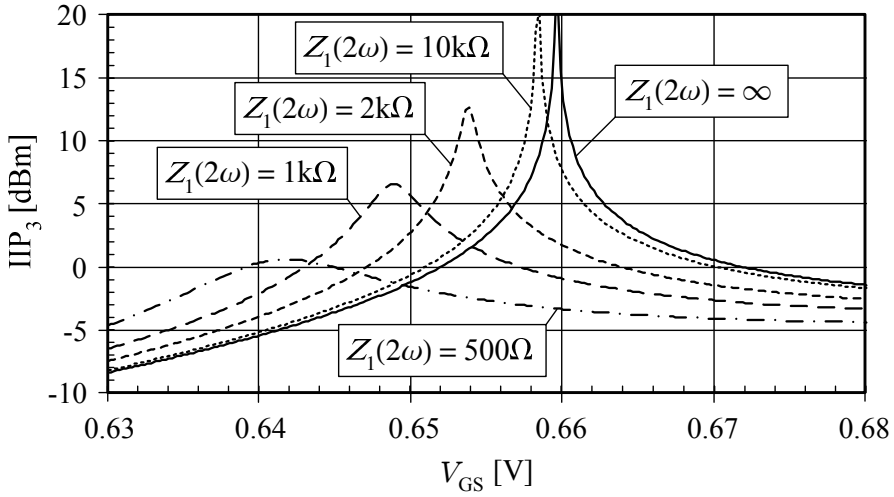

Figure V.11: Theoretical IIP_3 of a matched 350μm/0.25μm FET at 880MHz with C_{gd} taken into account and $Z_3(2\omega) = -j2\omega L$ (L=2nH).

its losses. For simplicity, we will neglect the effect of C_{gd} at the fundamental frequency ω but will include it at 2ω. Then, IIP_3 can be computed using (V.11) with $\varepsilon(2\omega)$ given by (V.16d). The results are presented in Fig. V.11. As can be seen, with $Z_1(2\omega) \geq 1\text{k}\Omega$, IIP_3 peaks by more than 10dB at a certain bias voltage. This voltage is offset from the optimum V_{GS} for zero g_3 (0.66V) due to the fact that, with a finite $Z_1(2\omega)$, the second term in (V.16d) is not cancelled completely. A peak in IIP_3 occurs when g_3 is equal to the real part of this term. It can be shown that this real part is positive; therefore, g_3 must be positive as well for the real part of $\varepsilon(2\omega)$ to be zero. As a result, the peak in IIP_3 occurs below the optimum bias voltage for zero g_3. The imaginary part of $\varepsilon(2\omega)$ limits the magnitude of this peak.

V.7 Effect of Optimum Gate Biasing on Gain and Noise Figure

In order to quantify the effect of the optimum gate biasing on the gain of a common-source amplifier, we will derive its effective transconductance defined as

$$g_{\mathrm{m,eff}} = \left| \frac{i_{\mathrm{d}}}{v_{\mathrm{x}}} \right|, \tag{V.19}$$

where i_{d} is the FET output current and v_{x} is the open-circuit voltage of the signal generator. We will use the equivalent circuit in Fig. V.7 and neglect C_{gd} and set $g_2 = g_3 = 0$. We will assume that Z_{x} at the fundamental frequency has only the real part equal to R_{x}, the FET input is conjugately matched to the transformed signal generator impedance [i.e., (V.10) holds], and the matching circuit is lossless. Then, the input power is given by

$$P_{\mathrm{in}} = \frac{(v_{\mathrm{x}}/2)^2}{2R_{\mathrm{x}}} = \frac{v_{\mathrm{g}}^2}{2}\mathrm{Re}(1/Z_{\mathrm{in}}). \tag{V.20}$$

From the last equation, we can derive the following expression

$$v_{\mathrm{g}} = \frac{v_{\mathrm{x}}}{2\sqrt{R_{\mathrm{x}}\mathrm{Re}(1/Z_{\mathrm{in}})}}, \tag{V.21}$$

which shows the voltage gain/loss due to the impedance transformation by the matching circuit. The transfer function from v_{g} to i_{d} can be easily found as

$$i_{\mathrm{d}} = \frac{v_{\mathrm{g}}}{j\omega C_{\mathrm{gs}}\left(g_1 \dfrac{L}{C_{\mathrm{gs}}} + j\omega L + \dfrac{1}{j\omega C_{\mathrm{gs}}}\right)}. \tag{V.22}$$

Substituting $Z_{\rm in}$ from (V.10) into (V.21), (V.21) into (V.22), and the latter into (V.19), we will find

$$g_{\rm m,eff} = \frac{1}{2\omega}\sqrt{\frac{\omega_{\rm T}}{R_{\rm x}L}}, \tag{V.23}$$

where $\omega_{\rm T} = g_1/C_{\rm gs}$ is the FET cut-off angular frequency. Even though (V.23) was derived without taking into account all parasitic capacitances of a FET, we will assume that it holds with all these capacitances present but with the following, more accurate expression for the cut-off frequency

$$f_{\rm T} = \frac{\omega_{\rm T}}{2\pi} = \frac{g_1}{2\pi(C_{\rm gs}+C_{\rm gd}+C_{\rm gb})}. \tag{V.24}$$

Fig. V.12 shows $f_{\rm T}$ of a 350μm/0.25μm NFET as a function of $V_{\rm GS}$. At the gate bias for zero g_3, $f_{\rm T}$ is only 8.1GHz, which is 2.4 times less than the peak cut-off frequency reached at $V_{\rm GS} = 1.2$V. Therefore, the LNA gain is expected to be 3.8dB lower if the input FET is biased at the peak-IIP$_3$ voltage versus the peak-$f_{\rm T}$ voltage. According to (V.23), to keep the gain high, the degeneration inductance of the input FET, L, must be reduced.

Fig. V.13 shows the measured minimum noise figure $\rm NF_{min}$ of a 960μm/0.25μm NFET at 5GHz as a function of the gate bias. As can be seen, $\rm NF_{min}$ in the optimum gate bias range (0.63-0.66V) is approximately 0.4dB higher than $\rm NF_{min}$ at $V_{\rm GS} > 0.8$V. Therefore, the optimum gate biasing degrades NF.

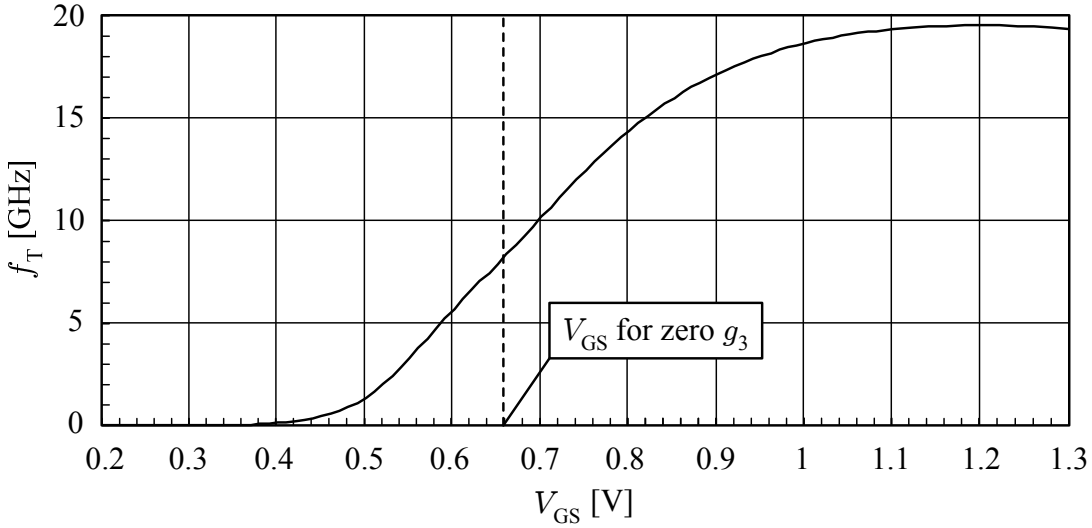

Figure V.12: Cut-off frequency of a 350μm/0.25μm NFET as a function of the gate bias.

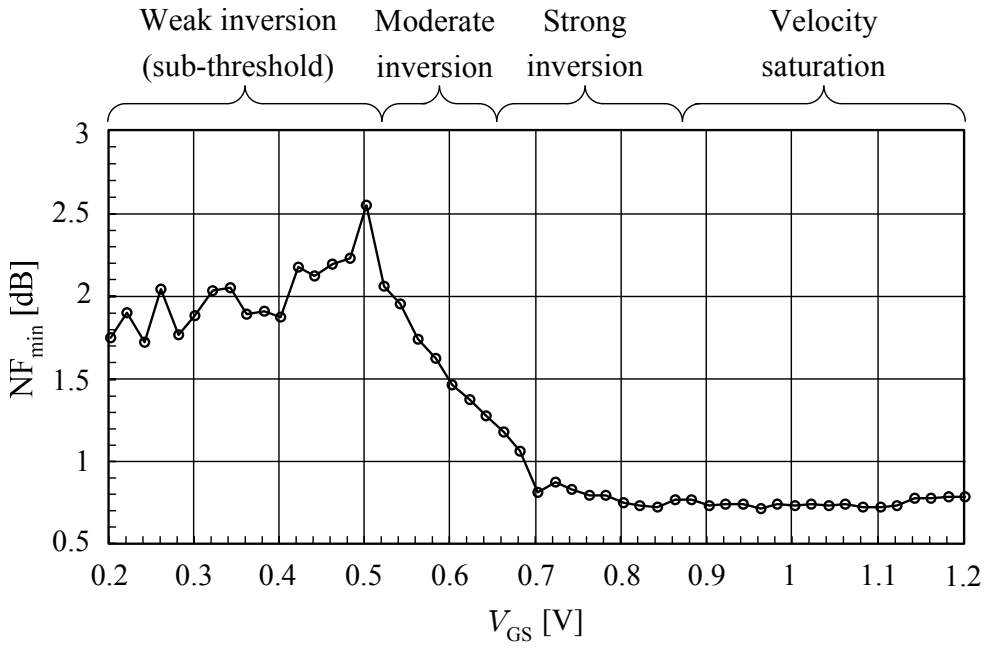

Figure V.13: Minimum noise figure of a 960μm/0.25μm NFET at 5GHz as a function of the gate bias.

V.8 Cellular-Band CMOS LNA Design

Since the peak IIP_3 in the optimum gate biasing method is limited by the imaginary part of the second term of (V.16d), the drain load impedance of the LNA input transistor at the 2nd-harmonic frequency, $Z_3(2\omega)$, has to be optimized to zero this imaginary part. Since g_1 is real, the equation that has to be solved is $\mathrm{Im}(g(2\omega)) = 0$. There are multiple $Z_3(2\omega)$ solutions to this equation. Their choice is determined by how easy they can be implemented. We selected a cascode LNA topology with $Z_3(2\omega)$ set by the cascode transistor. The simplified schematic of the LNA is shown in Fig. V.14, where the dashed box indicates the chip boundaries. Both FETs have the same dimensions of 350μm/0.25μm. To achieve a high LNA gain at low gate biases of M_1, the degeneration inductance was limited to the downbond inductance only ($L \approx 0.5$nH). The input matching circuit is just a series inductor of 19nH. Together with the package parasitics, it transforms the 50Ω output impedance of the signal generator to $Z_1(2\omega) = (142.8 - j730.4)\Omega$. For these values of L and $Z_1(2\omega)$, the possible solutions to the $\mathrm{Im}(g(2\omega)) = 0$ equation are plotted in Fig. V.15 as $\mathrm{Im}(Z_{3,\mathrm{opt}}(2\omega))$, with the x-axis being the real part. The impedance generated by the cascode FET M_2 is a function of C_c. Its possible theoretical values at the 2nd-harmonic frequency are also plotted in Fig. V.15 as $\mathrm{Im}(Z_{3,\mathrm{poss}}(2\omega))$. The intersection point of the two curves gives the real and imaginary parts of the desired optimum $Z_3(2\omega)$ that can be generated by M_2. The analytically derived value of C_c that results in this optimum 2nd-harmonic termination is 0.1pF. The final value of C_c was adjusted to 0.3pF after running more accurate Spectre simulations. The parallel feedback circuit with $R_\mathrm{f} = 3\mathrm{k}\Omega$ and $C_\mathrm{f} = 2.75$pF is

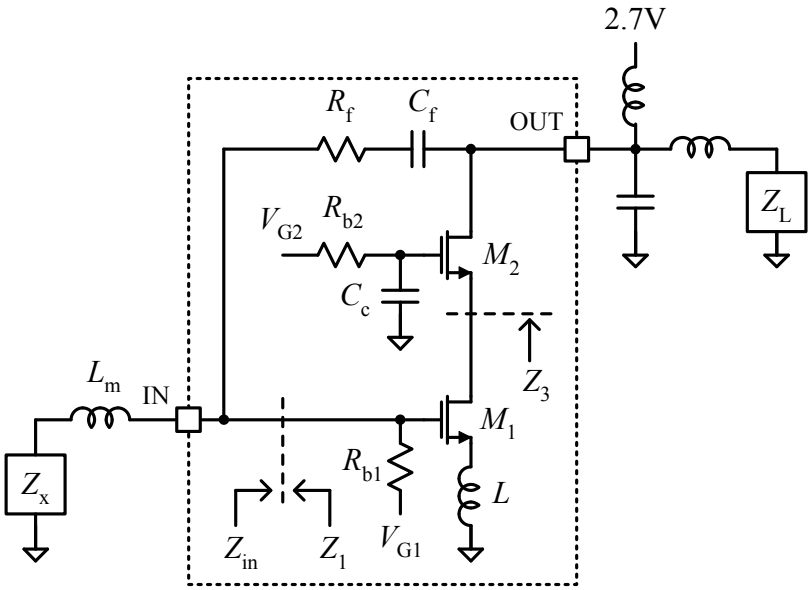

Figure V.14: Simplified schematic diagram of the CMOS LNA using the optimum gate biasing.

used to make the amplifier unconditionally stable.

V.9 Measured Results

The measured LNA performance at 880MHz as a function of the gate bias voltage of M_1 is shown in Fig. V.16. IIP_3 was measured with two tones separated by 1MHz. As can be seen, at V_{G1} of approximately 0.64V, IIP_3 exhibits a sharp peak of +10.5dBm with the gain of 14.4dB, NF of 1.8dB, and the dc current of 2mA from 2.7V. Above 0.64V, IIP_3 stays in a narrow range from 2 to 3.7dBm while the current increases to 20mA. The gain and NF improve to 19.4dB and 1.4dB, respectively.

A zoomed-in plot of IIP_3 and extracted g_3 of M_1 as functions of V_{G1} near the peak are shown in Fig. V.17. It can be seen that the peak occurs at a voltage that is approximately

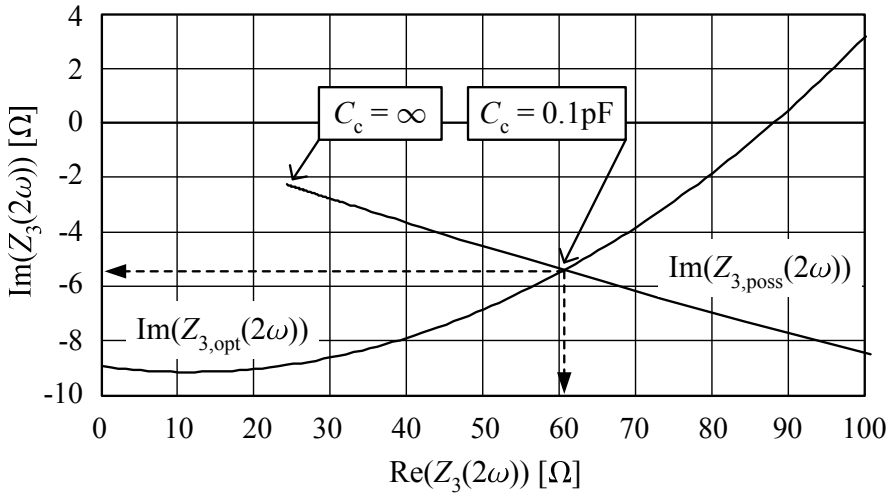

Figure V.15: Optimum and possible $Z_3(2\omega)$ values for the cellular-band CMOS LNA.

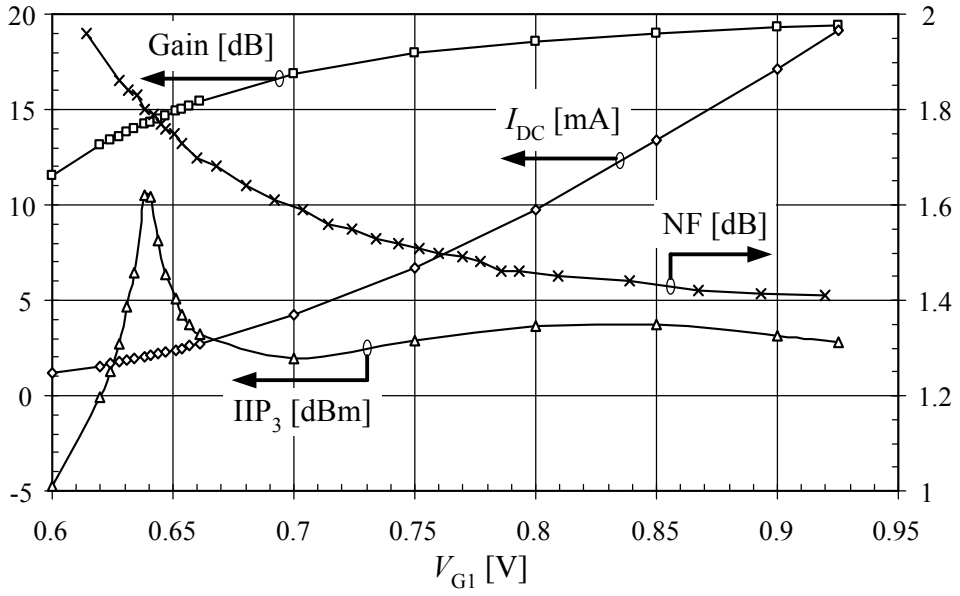

Figure V.16: Measured LNA performance at 880MHz as a function of the gate bias voltage of M_1.

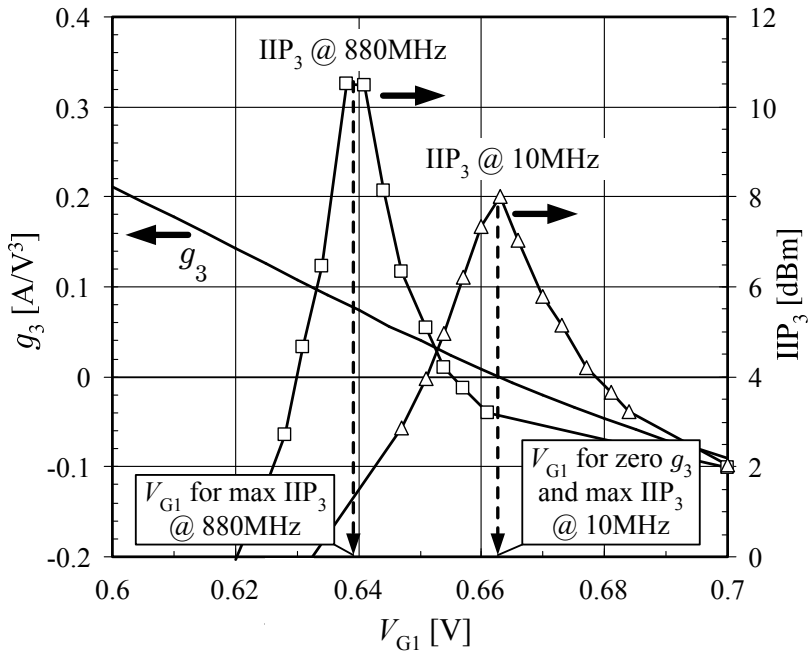

Figure V.17: Measured LNA IIP_3 and extracted g_3 of M_1 as functions of the M_1 gate bias.

20mV below V_{G1} at which g_3 is zero. The latter gives IIP_3 of only +3.2dBm. To verify that the offset between V_{G1} for peak IIP_3 and V_{G1} for zero g_3 is due to the LNA reactances, IIP_3 of the same LNA was also measured with the two tones centered at 10MHz, and its dependence on V_{G1} is plotted in Fig. V.17. As can be seen, IIP_3 in this case peaks exactly at V_{G1} at which g_3=0.

Fig. V.18 shows the measured fundamental and IMD_3 output powers of the LNA at the peak-IIP_3 bias as functions of the input power per tone with the input tones centered at 880MHz. As can be seen, the IMD_3 power rises by 3dB per 1dB of the input power up to -26dBm. Above this input power level, the 5th and higher odd-order nonlinearities become significant changing the slope of $P_{IMD3}(P_{in})$.

Since the present LNA design achieves a high IIP_3 by optimally terminating M_1 at

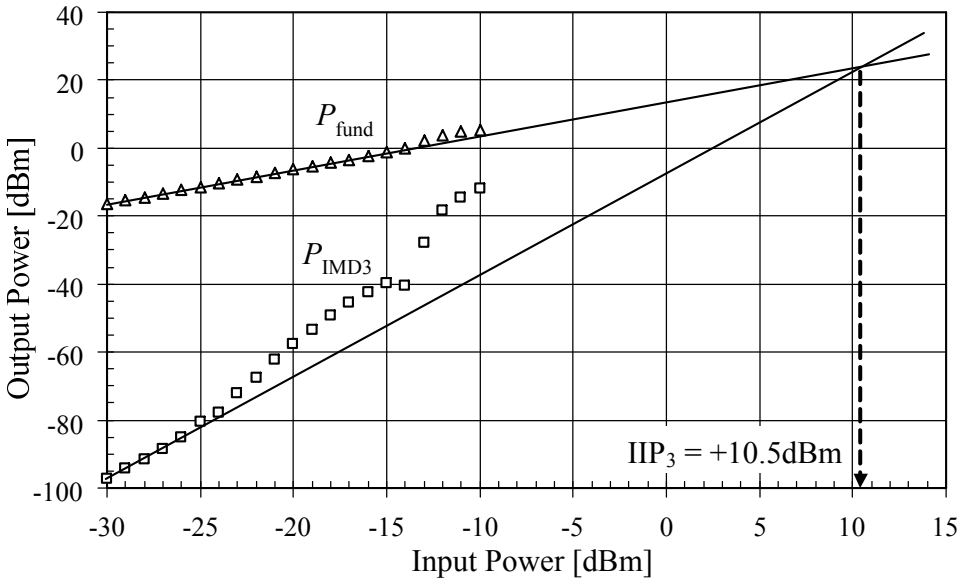

Figure V.18: Measured two-tone transfer characteristics at the peak-IIP_3 bias with two input tones centered at 880MHz.

the 2nd-harmonic frequency such that the 2nd and 3rd-order contributions to IMD_3 cancel each other at some bias point, the resulting IIP_3 should be sensitive to the signal source impedance at the 2nd-harmonic frequency, $Z_{\rm x}(2\omega)$, which can affect the out-of-phase balance of the IMD_3 contributors. To measure this sensitivity, we tuned $Z_{\rm x}(2\omega)$ independently of the signal source impedance at the fundamental frequency using a diplexer separating the cellular band frequencies from their 2nd harmonics. The results are presented in Fig. V.19, which shows the Smith chart for $Z_{\rm x}(2\omega)$ with IIP_3 contours (the values are in dBm) and the boxes mapping the signal source impedances for which IIP_3 was measured. We could not synthesize $Z_{\rm x}(2\omega)$ close to the Smith chart edge due to the non-zero insertion loss through the high-band path of the diplexer and the tuner. The results indicate that IIP_3 is fairly insensitive to $Z_{\rm x}(2\omega)$ along the constant reactance circles and changes from +7dBm to +13dBm along the constant resistance circles. In the case of a CDMA LNA, the sig-

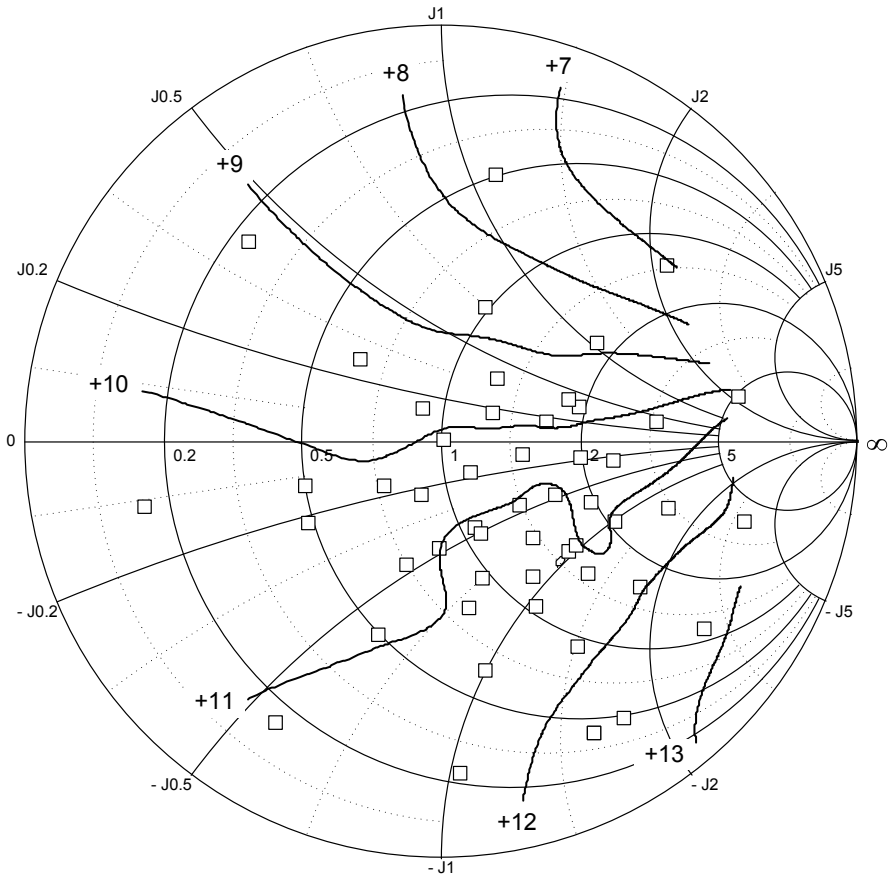

Figure V.19: Second harmonic source pull results for IIP_3.

nal source impedance at the 2nd-harmonic frequency is typically close to the edge of the Smith chart and is defined by the output impedance of the antenna duplexer and the electrical length of the transmission line connecting the duplexer to the LNA input matching circuit. An attention should be paid to this length to make sure that its phase delay moves the duplexer output impedance to the Smith chart area where IIP_3 is maximum.

To demonstrate the sensitivity of the LNA IIP_3 to bias, we measured ten parts mounted on different PC boards. The results are presented in Fig. V.20. It can be seen that biasing M_1 at a fixed gate voltage results in the largest deviations of IIP_3 from part to part. Bias-

ing M_1 at a fixed current, on the other hand, results in a tighter IIP_3 distribution with the minimum value of +9dBm at $I_{DC} \approx 2.05$mA.

V.10 Conclusions

We have shown that biasing a common-source FET at V_{GS} for zero g_3 causes a significant improvement in IIP_3 at low frequencies. We proposed a bias circuit that automatically generates this optimum voltage and showed that its precision can be satisfactory, provided that the mismatch between the reference FETs is reduced by increasing their total gate area and/or selecting a process with a thin gate oxide. We analyzed the effect of the optimum gate biasing on IIP_3 at RF and showed that the circuit reactances that introduce feedback paths can shift the peak in IIP_3 away from the bias voltage for zero g_3 and reduce the magnitude of this peak. We proposed a method based on tuning the drain load impedance to cancel the effect of the reactances on the maximum IIP_3. However, the offset between V_{GS} at which IIP_3 is maximum and V_{GS} at which $g_3 = 0$ can not be cancelled. Thus, a manual bias tuning is required to achieve a significant IIP_3 improvement at RF. We showed that a current-derived bias of a linearized FET results in less IIP_3 variations from part to part than a voltage-derived bias. Despite the fact the LNA input termination impedance at the 2nd-harmonic frequency affects the the out-of-phase balance between the 2nd and 3rd-order contributions to IMD_3 in our proposed method, the measured results demonstrated that IIP_3 is fairly insensitive to this impedance. The measured LNA gain and NF would not pass the requirements derived in Chapter III due to a low f_T at the optimum bias. However,

(a)

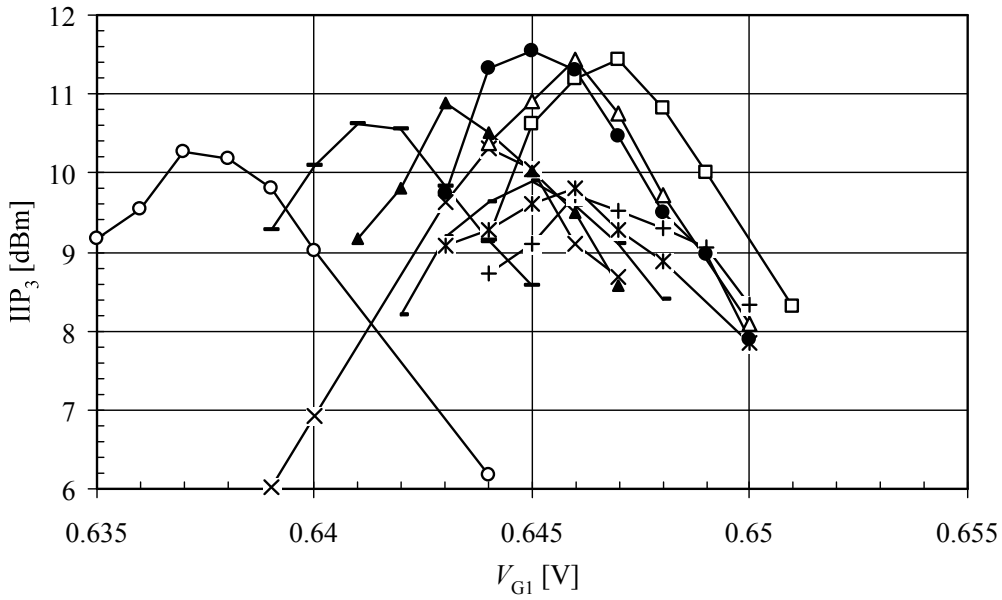

(b)

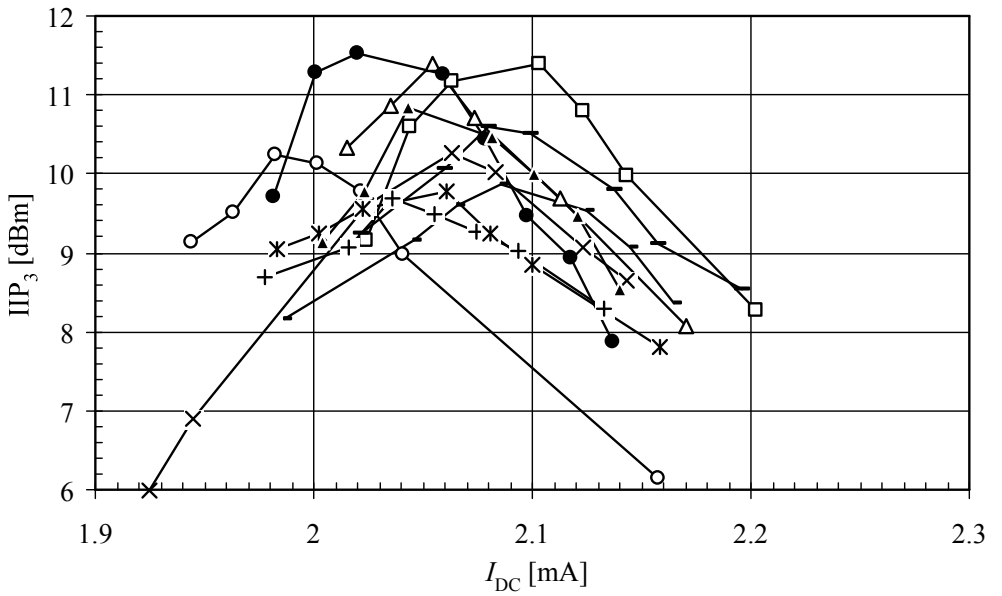

Figure V.20: Measured IIP_3 at 880MHz on ten boards. (a) As a function of the gate bias voltage of M_1. (b) As a function of the dc current of M_1.

as reported in [29] and [31], with shorter channels, the location of the optimum bias shifts to higher currents per μm of width, resulting in better gain and NF.

Chapter VI

Derivative Superposition Method

VI.1 Introduction

As was shown in the previous chapter, the optimum gate biasing method results in a very narrow IIP_3 peak, which is offset from the bias for zero g_3 at RF. This offset requires a manual bias adjustment, which makes it difficult to achieve a high IIP_3 in the presence of process and temperature variations. To reduce the IIP_3 sensitivity to the bias, the derivative superposition (DS) method was proposed in [112]. It uses two or more parallel FETs of different widths and gate biases to achieve a composite dc transfer characteristic with an extended V_{GS} range in which the 3rd-order derivative is close to zero. However, the IIP_3 improvement in this method is only modest at RF (3dB as reported in [113]). Reducing the source degeneration inductance and the drain load impedance at the 2nd-harmonic frequency of the composite input transistor allowed the authors of [114] to boost IIP_3 in the DS method by as much as 10dB. However, a small source degeneration inductance prevents a simultaneous noise-power input match leading to a higher NF. This NF increase comes in addition to an intrinsically higher NF of a composite FET in comparison with a single FET (higher by 0.6dB as reported in [114]).

This chapter first gives the dc theory of the conventional DS method and explains its poor performance at RF using the Volterra Series analysis results of the previous chapter. Then, based on the van der Ziel noise theory, we explain the higher NF resulting from the use of this method. We propose a modified DS method to achieve a very high IIP_3 at RF. Its principle of operation is explained based on the Volterra series analysis. A cellular CDMA 0.25μm CMOS LNA using this method is described. The measured data is presented to confirm the analytical results.

VI.2 DC and RF Theories of DS Method

As was shown in the previous chapter (see Fig. V.1(b)), the dependence of g_3 on $V_{\rm GS}$ is such that g_3 changes from positive to negative when $V_{\rm GS}$ transitions from the weak and moderate inversion regions to the strong inversion region. If a positive g_3 with a certain $g_3(V_{\rm GS})$ curvature of one FET is aligned with a negative g_3 with a similar but mirror-image curvature of another FET by offsetting their gate biases, and the g_3 magnitudes are equalized through a relative FET scaling, the resulting composite g_3 will be close to zero, and the theoretical $A_{\rm IP3}$ will be significantly improved in a wide range of the gate biases as shown in Fig. VI.1. At the optimum gate biases, FET $M_{\rm A}$ operates in the weak inversion region, near the peak in its positive g_3, and FET $M_{\rm B}$ operates in the strong inversion region, near the dip in its negative g_3.

The achieved $A_{\rm IP3}$ improvement due to zero composite g_3 happens only at very low frequencies, at which the effect of circuit reactances is negligible. As was shown in the pre-

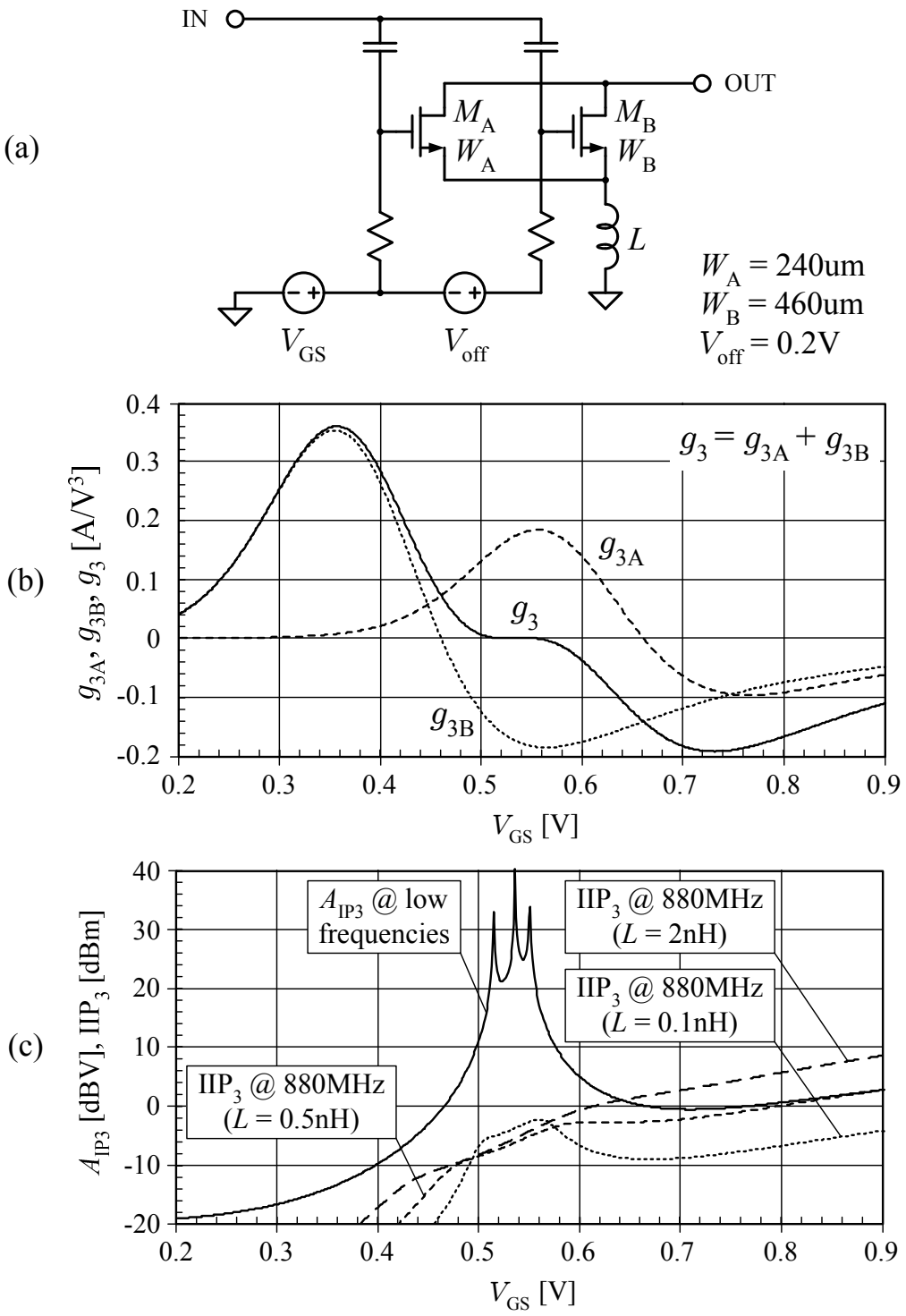

Figure VI.1: Derivative superposition method. (a) Composite FET. (b) 3rd-order power series coefficients. (c) Theoretical A_{IP3} at dc and IIP_3 at 880MHz. Note that the bondwire inductance reduces the improvement in IIP_3 at the optimum gate biases at high frequencies.

vious chapter, at high frequencies, the source degeneration inductance L creates a feedback path, which allows the 2nd-order nonlinearity of the FET transconductance to contribute to the 3rd-order distortion. Fig. VI.1(c) shows IIP_3 calculated at 880MHz using (V.11) and (V.12) for the composite FET in Fig. VI.1(a) with an input matching circuit consisting of a series capacitor and shunt inductor. As can be seen, the source degeneration inductance significantly suppresses the high-frequency IIP_3 peaking at V_{GS} where g_3 is close to zero. In fact, for realistic values of L, which are limited by the downbond inductance (≥ 0.5nH), the conventional DS method provides no IIP_3 improvement at all.

Replacing a common-source configuration with a symmetrically driven differential pair does not eliminate the 2nd-order contribution to IMD_3, because the 2nd harmonic currents generated by the FET pair are in phase and create a common-mode voltage at the common source if the impedance from this node to ground is not zero at the 2nd-harmonic frequency. As a result, the gate-source voltages of both FETs contain nonzero 2nd harmonic responses, which are mixed with the differential fundamental responses by the 2nd-order nonlinearities of the FETs, producing the differential IMD_3 responses in the drain currents.

According to (V.12), to minimize the 2nd-order contribution to IMD_3 of a common-source FET with a nonzero L, $Z_1(2\omega)$ must be increased. However, then the feedback through the neglected C_{gd} becomes significant, which also leads to the 2nd-order contribution to IMD_3. To completely eliminate this contribution and achieve a significant IIP_3 improvement in the DS method, the gate and drain terminations of the composite FET

at the 2nd-harmonic frequency must be optimized. Our analysis in the previous chapter shows that one of these terminations must have a negative real part, which would result in potential instability of the amplifier. The authors of [114] achieved a noticeable IIP_3 improvement using the conventional DS method by simply minimizing the source degeneration inductance and the drain load impedance. However, with a very small L, it is difficult to simultaneously achieve a good VSWR and NF. The gain and NF of the LNA in [114] are respectively 10dB and 2.85dB at 900MHz.

VI.3 Noise Issues in DS Method

The DS method in general uses two FETs, one of which is biased in the weak inversion (WI) region ($M_{\rm A}$ in Fig. VI.1(a)) and the other in the strong inversion (SI) region ($M_{\rm B}$ in Fig. VI.1(a)). Intuitively, the overall NF of the composite FET should be dominated by the FET in SI because it draws 20-40 times more current than the FET in WI. This assumption is confirmed by simulations using BSIM3v3 models. However, it disagrees with our measured data. To explain this disagreement, we will analyze the noise performance of the composite FET.

The most significant MOSFET noise sources at RF are the drain current noise and the induced gate noise. These noise sources for the composite FET in the DS method are shown in Fig. VI.2, where the dc blocking capacitors and the bias resistors are neglected for simplicity. As can be seen, the drain and induced gate noise currents of the two FETs appear in parallel. These noise currents are given by [144]

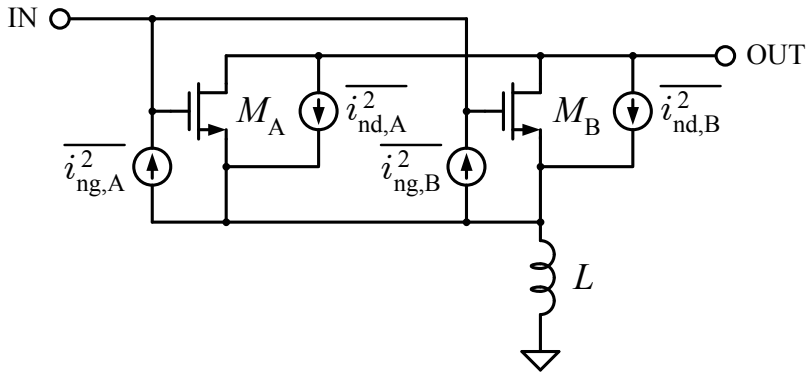

Figure VI.2: Simplified schematic of the composite FET in the DS method with major noise sources. The dc blocking capacitors and the bias resistors are neglected for simplicity.

$$\overline{i^2_{\mathrm{nd,X}}} = 4kT\Delta f \gamma_{\mathrm{X}} g_{\mathrm{d0,X}}, \tag{VI.1}$$

$$\overline{i^2_{\mathrm{ng,X}}} = 4kT\Delta f \delta_{\mathrm{X}} g_{\mathrm{g,X}}, \tag{VI.2}$$

where

$$g_{\mathrm{g,X}} = \frac{4\omega^2 (C_{\mathrm{ox}} W_{\mathrm{X}} L_{\mathrm{eff}})^2}{45 g_{\mathrm{d0,X}}}. \tag{VI.3}$$

Above, k is the Boltzmann's constant, T is the absolute temperature, γ_{X} and δ_{X} are the bias-dependent noise coefficients, $g_{\mathrm{d0,X}}$ is the drain-source conductance at zero V_{DS}, C_{ox} is the gate oxide capacitance per unit area, W_{X} is the channel width, and L_{eff} is the channel length, assumed to be the same for both FETs. The letter "X" in the subscripts of the above notations denotes either "A" or "B". The two noise currents are partially correlated, with a correlation coefficient defined as

$$c_{\mathrm{X}} = \frac{\overline{i_{\mathrm{ng,X}} \cdot i^*_{\mathrm{nd,X}}}}{\sqrt{\overline{i^2_{\mathrm{ng,X}}} \cdot \overline{i^2_{\mathrm{nd,X}}}}}. \tag{VI.4}$$

For simplicity, we will neglect the short-channel effects here. According to van der Ziel [144], if M_{B} is a saturated long channel FET, biased in SI, then $\gamma_{\mathrm{B}} = 2/3$, $\delta_{\mathrm{B}} = 4/3$,

$c_{\rm B} = j0.395$, and

$$g_{\rm d0,B} = \sqrt{2\mu C_{\rm ox}\frac{W_{\rm B}}{L_{\rm eff}}I_{\rm D,B}}, \tag{VI.5}$$

where μ is the electron mobility and $I_{\rm D,B}$ is the drain saturation current of $M_{\rm B}$. The van der Ziel noise model can also be extended for a FET in WI. As shown in Appendix D, if $M_{\rm A}$ is a saturated long channel FET, biased in WI, then $\gamma_{\rm A} = 1/2$, $\delta_{\rm A} = 45/16$, $c_{\rm A} = j0.707$, and

$$g_{\rm d0,A} = \frac{I_{\rm D,A}}{\phi_{\rm t}}, \tag{VI.6}$$

where $I_{\rm D,A}$ is the drain saturation current of $M_{\rm A}$, and $\phi_{\rm t}$ is the thermal voltage kT/q. Substituting (VI.6) into (VI.3) and the latter into (VI.2), we can make an interesting observation. While $M_{\rm A}$ draws a negligible drain current, its induced gate noise is inversely proportional to the drain current and, thus, can be quite significant. It adds to the induced gate noise current of $M_{\rm B}$, degrading the overall NF in the DS method. Simulations using BSIM3V3 models do not predict this NF degradation because they do not take into account the induced gate noise.

To quantitatively estimate the NF degradation in the DS method due to the WI operation of $M_{\rm A}$, we will reuse the result for the minimum noise factor of a common-source amplifier without degeneration from [148], but we will rewrite it in a more general way as follows

$$F_{\rm min} = 1 + \frac{2}{g_{\rm m}}\sqrt{\gamma g_{\rm d0}\delta g_{\rm g}\left(1 - |c|^2\right)}. \tag{VI.7}$$

We will neglect the drain noise current of $M_{\rm A}$ due to the fact that $I_{\rm D,A} \ll I_{\rm D,B}$. Then, we

can write

$$g_{\mathrm{m}} \approx g_{\mathrm{m,B}}, \tag{VI.8a}$$

$$g_{\mathrm{d0}} \approx g_{\mathrm{d0,B}}, \tag{VI.8b}$$

$$\gamma \approx \gamma_{\mathrm{B}}. \tag{VI.8c}$$

The induced gate noise of M_{A} increases the portion of the total induced gate noise current that is uncorrelated to $i_{\mathrm{nd,B}}$. This uncorrelated portion is given by

$$\begin{aligned}\overline{i_{\mathrm{ngu}}^2} &= 4kT\Delta f\delta g_{\mathrm{g}}\left(1-|c|^2\right)\\ &= 4kT\Delta f\delta_{\mathrm{A}} g_{\mathrm{g,A}} + 4kT\Delta f\delta_{\mathrm{B}} g_{\mathrm{g,B}}\left(1-|c_{\mathrm{B}}|^2\right).\end{aligned} \tag{VI.9}$$

From the last equation we get

$$\delta g_{\mathrm{g}}\left(1-|c|^2\right) = \delta_{\mathrm{A}} g_{\mathrm{g,A}} + \delta_{\mathrm{B}} g_{\mathrm{g,B}}\left(1-|c_{\mathrm{B}}|^2\right). \tag{VI.10}$$

Substituting (VI.10) and (VI.8) into (VI.7), we get

$$F_{\mathrm{min}} \approx 1 + \frac{2}{g_{\mathrm{m,B}}}\sqrt{\gamma_{\mathrm{B}} g_{\mathrm{d0,B}}\left[\delta_{\mathrm{A}} g_{\mathrm{g,A}} + \delta_{\mathrm{B}} g_{\mathrm{g,B}}\left(1-|c_{\mathrm{B}}|^2\right)\right]}. \tag{VI.11}$$

The plot of F_{min} of the circuit in Fig. VI.1(a) with $L = 0$, computed using (VI.11), versus the gate bias of M_{A} is shown in Fig. VI.3 (the gate bias of M_{B} is kept constant). As can be seen, F_{min} rapidly increases with $V_{\mathrm{GS,A}}$ falling below the threshold voltage (0.58V in this process) due to the increasing contribution of the induced gate noise of M_{A}. It should be noted that (VI.11) was derived using the van der Ziel's first-order approximation of the induced gate noise, and, therefore, it may correctly show the trend of F_{min} versus gate bias but it may not be accurate for predicting the absolute values of F_{min} [149].

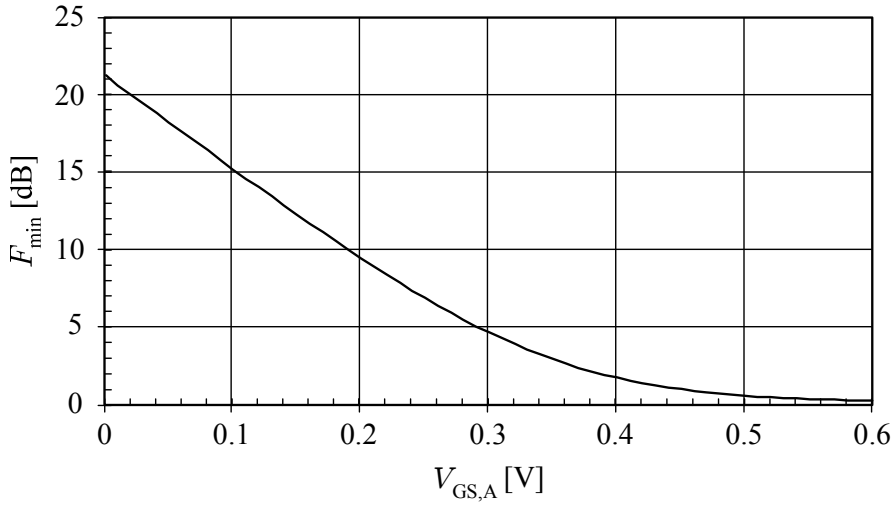

Figure VI.3: Theoretical $F_{\min}$ of the circuit in Fig. VI.1(a) with $L = 0$ vs. the gate bias of M_{A}. The gate bias of M_{B} is kept constant.

VI.4 Modified DS Method

For the DS method to significantly boost IIP_3 at RF, it is not necessary to completely eliminate the 2nd-order contribution to IMD_3. It is enough to make it the same magnitude and opposite phase with the 3rd-order contribution. Instead of optimally scaling and rotating the 2nd-order contribution by tuning the 2nd-harmonic terminations of the composite FET, here we propose a method shown in Fig. VI.4, which is similar to the conventional DS method but uses two source-degeneration inductors in series, with the FET sources connected to different nodes of the inductor chain to adjust the magnitude and phase of the composite 3rd-order contribution. M_{A} is biased in WI with a positive $g_{3\mathrm{A}}$, and M_{B} is biased in SI with a negative $g_{3\mathrm{B}}$. It can be shown that the contributions of $g_{1\mathrm{A}}$ and $g_{2\mathrm{A}}$ to the overall response are negligible. The purpose of connecting the M_{A} source to the common node of the two inductors is to change the magnitude and phase of its $g_{3\mathrm{A}}$ contribution to

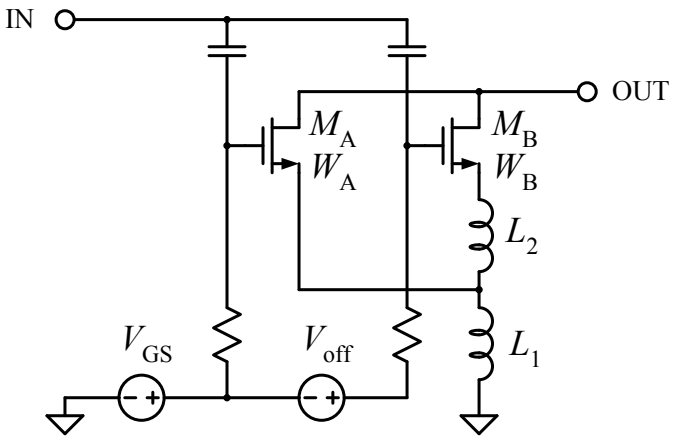

Figure VI.4: Modified derivative superposition method.

IMD_3 relative to the g_{2B} and g_{3B} contributions of M_B.

To explain how the composite FET in Fig. VI.4 achieves a high IIP_3 at RF, we will analyze its simplified equivalent circuit shown in Fig. VI.5, where the signal generator is modeled by a Thevenin equivalent circuit with an open-circuit voltage v_x and a transformed output impedance Z_1 as before, C_A and C_B are the gate-source capacitances of M_A and M_B, respectively, v_A and v_B are the small-signal gate-source voltages of M_A and M_B, respectively, and i_A and i_B are the small-signal drain currents of M_A and M_B, respectively. Here we used the same assumptions as those made for the equivalent circuit in Fig. V.7. To simplify derivations further, we also neglected the linear and 2nd-order responses of M_A, i.e., assumed that $g_{1A} \approx 0$ and $g_{2A} \approx 0$.

The combined output current can be represented as the following truncated Volterra series in terms of the excitation voltage v_x in the time domain

$$i(v_x) = C_1(s) \circ v_x + C_2(s_1, s_2) \circ v_x^2 + C_3(s_1, s_2, s_3) \circ v_x^3, \qquad \text{(VI.12)}$$

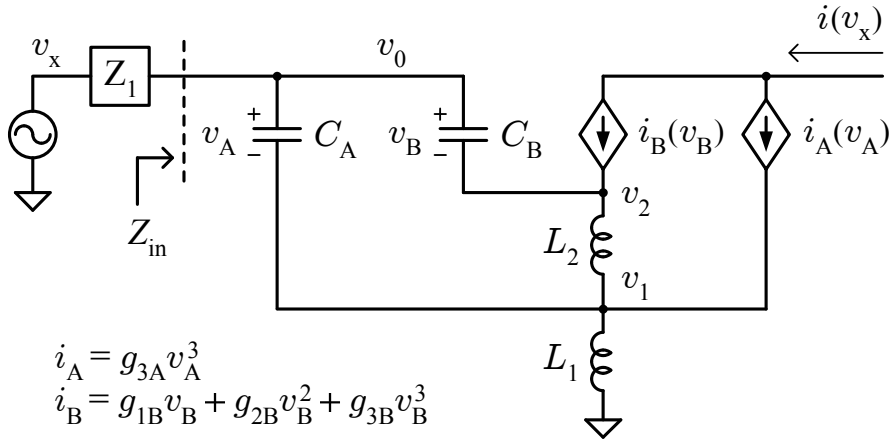

Figure VI.5: Simplified equivalent circuit of the composite FET in Fig. VI.4.

where $C_n(s_1, s_2, \cdots, s_n)$ is the nth-order nonlinear transfer function. For a two-tone excitation

$$v_x = A\left[\cos(\omega_a t) + \cos(\omega_b t)\right], \tag{VI.13}$$

IIP_3 is given by

$$\text{IIP}_{3,2\omega_b-\omega_a} = \frac{1}{6\text{Re}(Z_1(s_a))}\left|\frac{C_1(s_a)}{C_3(s_b, s_b, -s_a)}\right|. \tag{VI.14}$$

The derivations of $C_1(s_a)$ and $C_3(s_b, s_b, -s_a)$ for a narrow tone separation, the conjugate input match at the fundamental frequency, and a low-impedance input termination at the 2nd-harmonic frequency are shown in Appendix E. Substituting (E.3a) and (E.21) into (VI.14) and taking into account (E.22), we get

$$\text{IIP}_3 \approx \frac{4g_{1B}^2\omega^2[L_1(C_A + C_B) + L_2C_B]}{3|\varepsilon|}, \tag{VI.15}$$

where

$$\varepsilon = g_{3\mathrm{A}}(1 + j\omega L_2 g_{1\mathrm{B}})\left[1 + (\omega L_2 g_{1\mathrm{B}})^2\right]\left[1 + \frac{L_2 C_{\mathrm{B}}}{L_1(C_{\mathrm{A}} + C_{\mathrm{B}}) + L_2 C_{\mathrm{B}}}\right] + g_{3\mathrm{B}} - \frac{2g_{2\mathrm{B}}^2}{3g_{1\mathrm{B}}}\frac{1}{1 + \dfrac{1}{j2\omega(L_1 + L_2)g_{1\mathrm{B}}}}, \tag{VI.16}$$

and $\omega \approx \omega_{\mathrm{a}} \approx \omega_{\mathrm{b}}$. The above expression does not show IIP_3 dependence on the intermodulation frequency (i.e., $2\omega_{\mathrm{b}} - \omega_{\mathrm{a}}$ vs. $2\omega_{\mathrm{a}} - \omega_{\mathrm{b}}$) because the contribution of the difference-frequency mixing terms to IMD_3 is negligible at small $\Delta\omega$ ($= \omega_{\mathrm{b}} - \omega_{\mathrm{a}}$) due to the absence of a dc source resistance in the analyzed circuit (see Fig. VI.5).

Parameter ε shows how different nonlinearities of the circuit in Fig. VI.5 contribute to IMD_3. The first two terms in (VI.16) represent the contributions of the 3rd-order nonlinearities of M_{A} and M_{B}, respectively, and the last term represents the contribution of the 2nd-order nonlinearity of M_{B}. The phase of the composite 3rd-order contribution of M_{A} and M_{B} is dependent on L_2. If L_2 were zero, the imaginary part of the first term in (VI.16) would be zero, and the vector of the composite 3rd-order contribution, described by the first two terms, could never be made collinear with the vector of the 2nd-order contribution, described by the last term, because the latter has a nonzero imaginary part. Therefore, the distortion cancellation would be impossible as in the case of the conventional DS method. Graphically, this is explained by the vector diagram in Fig. VI.6(a).

The idea of the modified DS method is to use the L_2 portion of the total degeneration inductance to rotate the phase of the $g_{3\mathrm{A}}$ contribution to IMD_3 relative to that of the $g_{3\mathrm{B}}$ contribution, such that their sum is out-of-phase with the 2nd-order contribution. Graphically,

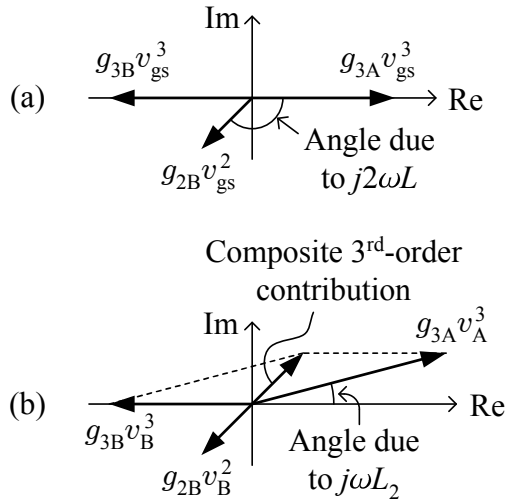

Figure VI.6: Vector diagram for the IMD_3 components. (a) Conventional DS method. (b) Modified DS method.

this is explained by the vector diagram in Fig. VI.6(b). In order for IMD_3 to be zero, both the real and imaginary parts of ε must be zero. The equations $\mathrm{Re}(\varepsilon) = 0$ and $\mathrm{Im}(\varepsilon) = 0$ can be solved for L_1 and L_2. Using the FET sizes and bias offset from Fig. VI.1(a) as an example, the solutions at $V_{\mathrm{GS}} = 0.57$V are $L_1 = 0.83$nH and $L_2 = 0.61$nH. The plot of IIP_3 at 880MHz computed using (VI.15) versus V_{GS} is shown in Fig. VI.7. As can be seen, with the total degeneration inductance of 1.44nH, a significant IIP_3 improvement is achieved in a wide range of biases in comparison with the conventional DS method, used at the same frequency (see Fig. VI.1(c)). The fact that the proposed modified DS method does not require the degeneration inductance to be minimized as in [114] makes the simultaneous noise-power match possible.

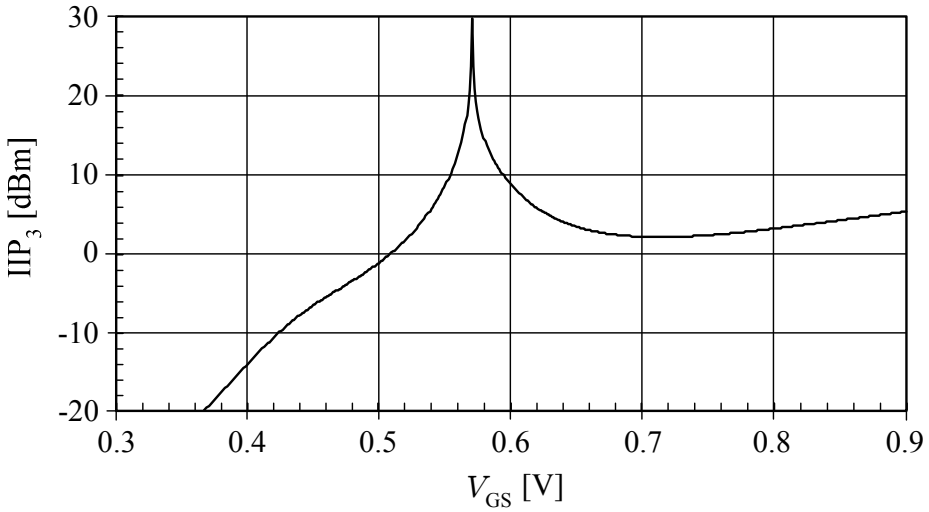

Figure VI.7: Theoretical IIP_3 at 880MHz of the circuit in Fig. VI.4 ($W_{\rm A} = 240\mu$m, $W_{\rm B} = 460\mu$m, $L_1 = 0.83$nH, $L_2 = 0.61$nH, $V_{\rm off} = 0.2$V).

VI.5 LNA Design and Measured Results

The proposed modified DS method was used in a cellular-band CDMA LNA, whose schematic is shown in Fig. VI.8. Instead of two degeneration inductors in series, the LNA uses a single tapped inductor to save die area. The input FETs $M_{\rm A}$ and $M_{\rm B}$ are interdigitated for better mutual matching and to reduce their combined drain-bulk capacitance and, thus, the noise contribution of the cascode FET $M_{\rm C}$. FET $M_{\rm A}$ is biased in WI, and FET $M_{\rm B}$ is biased in SI. Their gate bias voltages are generated by the diode-connected FETs $M_{\rm RA}$ and $M_{\rm RB}$, respectively, whose drain currents $I_{\rm RA}$ and $I_{\rm RB}$ are independently programmable. We used the current-derived bias because it results in less IIP_3 variations from part to part than a voltage-derived bias, as was shown in the previous chapter. A constant-g_m bias circuit was used to minimize the gain and IIP_3 variations over temperature. The ratios $W_{\rm B}/W_{\rm A}$, $I_{\rm RB}/I_{\rm RA}$, and L_2/L_1 were optimized for the highest IIP_3, using a commer-

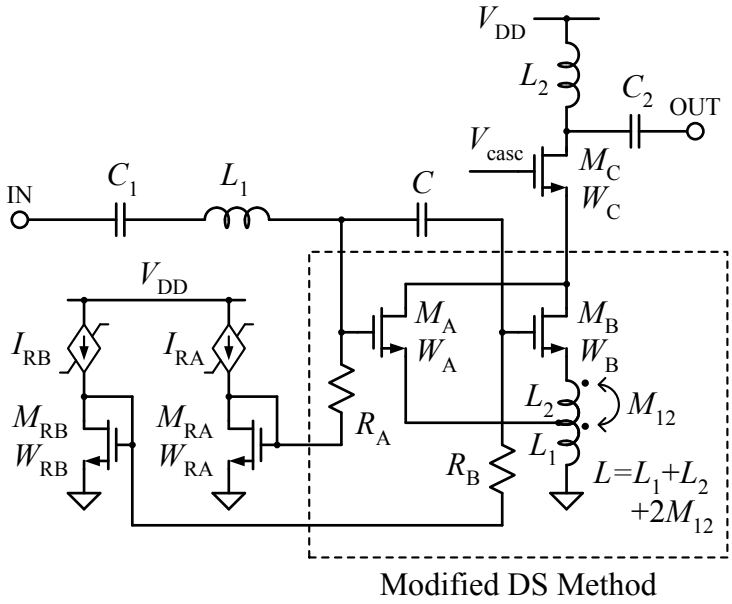

Figure VI.8: Simplified schematic diagram of the CMOS LNA using the modified DS method.

cial circuit simulator. Because of the interdigitation of $M_{\rm A}$ and $M_{\rm B}$, the evaluated values of $W_{\rm B}/W_{\rm A}$ were limited to ratios of small integers, e.g., 1/1, 2/1, 3/2, etc. The evaluated values of $I_{\rm RB}/I_{\rm RA}$ were also limited to the ratios of integers, whose sum was kept constant (equal to 40) to ensure a constant total dc current. At each optimization step, the total degeneration inductance was adjusted to keep the LNA gain constant. We found that the optimum ratios were $W_{\rm B}/W_{\rm A} = 3/2$, $I_{\rm RB}/I_{\rm RA} = 39/1$, and $L_2/L_1 = 0.85$, with the total degeneration inductance L of 2.7nH including the bondwire.

The LNA was manufactured in a 0.25μm Si CMOS technology as part of a cellular-band CDMA zero-IF receiver and packaged in a QFN 32-pin package. Its measured power gain and NF are 15.5dB and 1.65dB, respectively, with the current consumption of 9.3mA from 2.6V, excluding the bias circuit. The input and output return losses are lower than

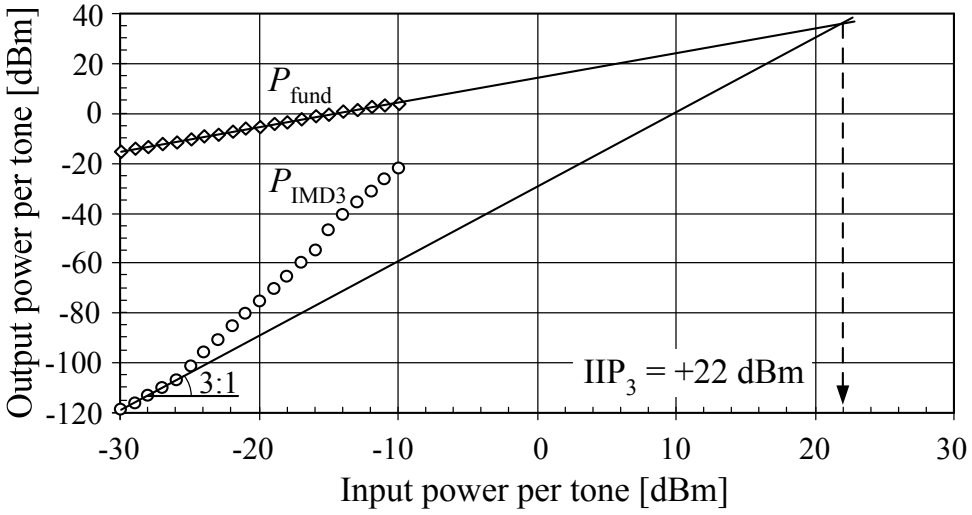

Figure VI.9: Measured CMOS LNA 2-tone transfer characteristics.

-11dB. The LNA IIP_3 was tested with two tones at 880MHz and 880.5MHz and was found to be insensitive to the tone separation. The measured output powers of the fundamental and IMD_3 responses as functions of the input power per tone are plotted in Fig. VI.9. As can be seen, below $P_{\rm in}$ of -25dBm per tone, the $P_{\rm IMD3}(P_{\rm in})$ curve rises with a slope 3:1, and $\rm IIP_3 = +22dBm$. At higher input power levels, the slope is steeper than 3:1 indicating that IMD_3 is dominated by the 5th and higher odd-order nonlinearities. If the 3rd-order nonlinearity was completely cancelled, the slope 3:1 would not exist, and IIP_3 would be meaningless. In this case, the 5th or higher order intercept points could be used to estimate the distortion levels at particular input power levels. We also measured IIP_3 for different values of the master reference current, with the ratio $I_{\rm RB}/I_{\rm RA}$ kept constant. Fig. VI.10 shows that the LNA maintains high IIP_3 in a wide range of the dc current through the composite FET. The achieved IIP_3 was found to be insensitive to the input and output harmonic terminations.

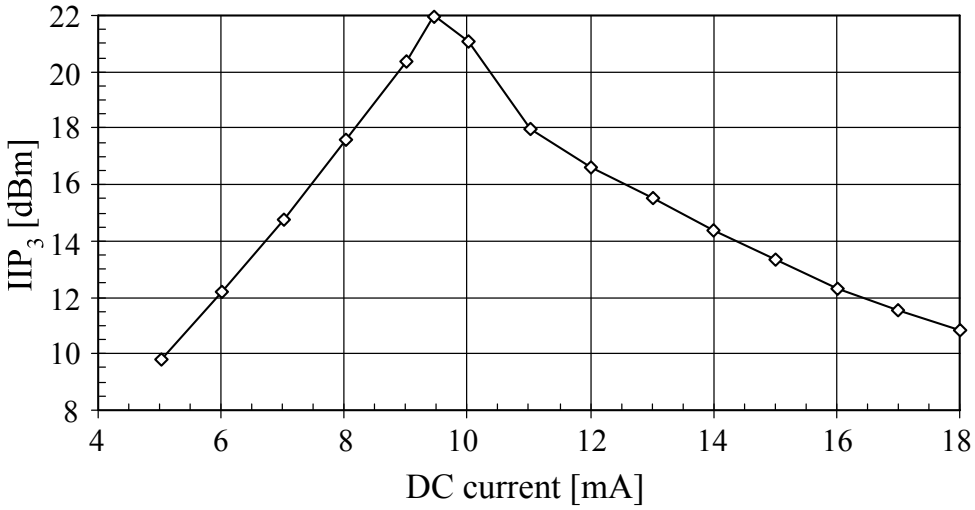

Figure VI.10: Measured IIP_3 at $P_{\mathrm{in}} = -30$dBm as a function of the combined dc current of the input FETs. The ratio $I_{\mathrm{RB}}/I_{\mathrm{RA}}$ is kept constant.

To investigate the effect of the gate bias of M_{A} on the LNA performance, we measured the LNA IIP_3, gain, NF, and dc current as functions of $V_{\mathrm{GS,A}}$, with $V_{\mathrm{GS,B}}$ kept constant. The results are presented in Fig. VI.11. As can be seen, the peak in IIP_3 is fairly broad and centered around $V_{\mathrm{GS,A}} = 0.55$V. As predicted by the theory, reducing $V_{\mathrm{GS,A}}$ increases the LNA NF due to the increasing induced gate noise current of M_{A}. The rate at which the NF increases with the falling $V_{\mathrm{GS,A}}$ is much lower than the theoretical one shown in Fig. VI.3, indicating the deficiency of the van der Ziel's first-order approximation of the induced gate noise at subthreshold biases (see also [149]).

We also manufactured an LNA with a single input FET. It achieved 16dB gain, +2dBm IIP_3, and 1.4dB NF with 9mA dc current. So, the proposed modified DS method boosted IIP_3 by about 20dB but degraded NF by 0.25dB due to the induced gate noise of the FET biased in WI (M_{A} in Fig. VI.8).

We compared our CMOS LNAs with other state-of-the-art FET LNAs using the dy-

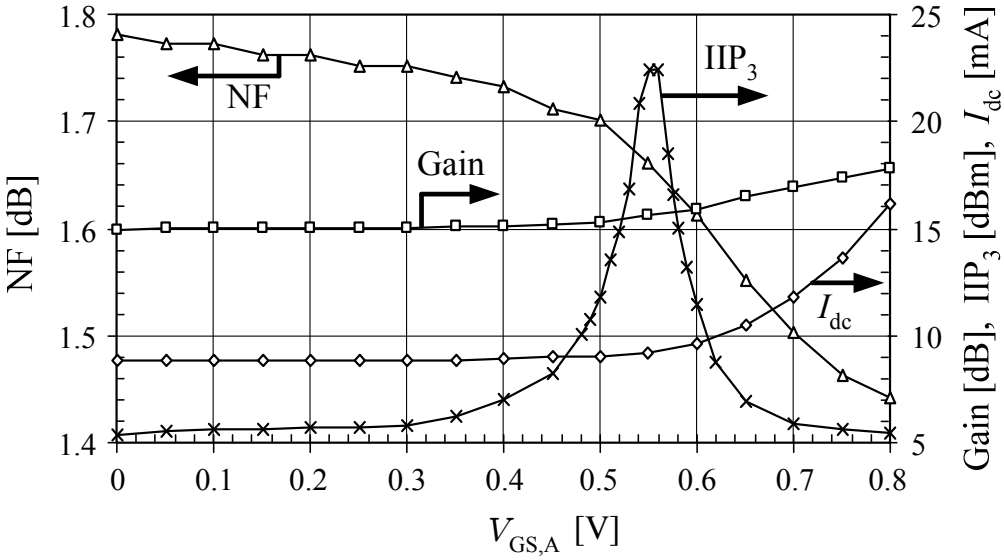

Figure VI.11: Measured IIP_3, gain, NF, and combined dc current versus the gate bias voltage of M_{A}. The gate bias of M_{B} is kept constant ($V_{\mathrm{GS,B}} \approx 0.75$V).

namic range FOM defined by (IV.30), and the results are presented in Table VI.1. As can be seen, our LNA using the modified DS method has the highest FOM. This FOM is also the highest among LNAs using bipolar transistors (see Table IV.1).

VI.6 Conclusions

We have shown that the conventional DS method does not provide a significant IIP_3 improvement at RF due to the contribution of the 2nd-order nonlinearity to IMD_3. In general, the vector of this contribution is not collinear with the vector of the 3rd-order contribution, and, therefore, they can not cancel each other. To give these contributions opposite phases, we proposed a modified DS method, which uses two inductors in series (or a tapped inductor) for source degeneration of the composite FET. This method boosted the

Table VI.1: Comparison of state-of-the-art linear FET LNAs

LNA	Technology	Freq GHz	S21 dB	NF dB	IIP_3 dBm	P_{dc} mA@V	FOM
LNA in Fig. VI.8	0.25μm Si CMOS	0.9	15.5	1.65	+22	9.3@2.6	503
LNA in Fig. V.14	0.25μm Si CMOS	0.9	14.6	1.8	+10.5	2@2.7	117
[115]	0.6μm GaAs MESFET	0.9	17	1.6	+8.5	4.7@2.7	62.8
[118]	0.25μm Si CMOS	2.2	14.9	3	+16.1	9.4@2.5	53.8
[150]	0.4μm GaAs PHEMT	0.9	12.5	1	+8	5@3	28.9
[151]	0.5μm GaAs PHEMT	2.1	15	1	+7.3	8.5@3	25.7
[114]	0.35μm Si CMOS	0.9	10	2.8	+15.6	7.8@2.7	19
[100]	0.2μm GaAs PHEMT	2	9	3	+19	22@5	5.8
[111]	0.35μm Si CMOS	0.9	2.5	2.8	+18	15@3	3

IIP_3 of the designed CMOS LNA by 20dB. This LNA has the highest dynamic range FOM among known state-of-the-art LNAs. We also explained the reason why the composite FET in the DS method exhibits a higher NF than a single FET. Our analysis showed that the FET biased in the subthreshold region is responsible for this NF degradation due to its high induced gate noise, which is inversely proportional to the drain current. We found that the van der Ziel noise theory overestimates this NF degradation, which indicates the deficiency of its first-order approximation of the induced gate noise at subthreshold biases.

Chapter VII

Conclusions

VII.1 Research Summary

XMD generated by a CDMA LNA significantly degrades the RX sensitivity. It must be accurately estimated from the TX leakage statistics and the circuit transfer function in order to derive the LNA linearity requirement. The latter in combination with other design objectives such as low NF, high gain, low dc current, and low-cost, high integration-level implementation can be met by using linearization techniques.

In this dissertation, different methods to quantify XMD in a CDMA LNA are reviewed. Because of their simplicity and speed, behavioral modeling methods are found to be more suitable for the final task of deriving the LNA linearity requirement. However, their accuracy depends on the circuit and signal models. It was shown that, even though a power series model of a circuit transfer function is considered to be suitable for memoryless circuits only, it can still accurately take into account the circuit reactances if its expansion coefficients are expressed through the appropriate intercept points, such as TBIP or IIP_3. An analysis using such a power series yields the same results as the one using a Volterra series but with much less complexity. Modeling a CDMA signal is another part of the be-

havioral modeling of XMD. A commonly-used Gaussian approximation makes the XMD analysis very simple, but it yields the results that do not agree with simulated and measured data. A new CDMA signal model is proposed based on a mathematical description of a CDMA reverse-link modulator. Using this model and the power series representation of the LNA transfer function, a closed-form expression of XMD of a narrow-band jammer is derived. It agrees well with the measured results. This XMD expression is then used to derive IIP_3 requirements of CDMA LNAs to meet the single-tone desensitization requirement of the IS-98 standard. For a typical SAW duplexer, the minimum IIP_3 should be +8.2dBm for a cellular LNA and +6.9dBm for a PCS LNA. Such a high linearity should be achieved in combination with the maximum NF of 1.8dB and the power gain of 16 ± 1dB.

Among different linearization techniques that can meet the above design challenge at low cost, this dissertation investigated the optimum out-of-band tuning, optimum gate biasing, and the DS method. Although the optimum tuning of either a difference-frequency or 2nd-harmonic termination has been previously known to reduce IMD_3, it is shown here that both terminations must be optimized simultaneously to achieve the lowest distortion possible. Simply reducing the bias circuit impedance to reduce IMD_3, as it is proposed in many publications, works only for a strongly-degenerated BJT operating well below its cut-off frequency and terminated at the input with a relatively small impedance at the 2nd-harmonic frequency. Two LNA designs are presented to prove the theoretical results: a 2GHz BJT LNA with optimized difference-frequency and 2nd-harmonic terminations and a cellular-band SiGe HBT LNA with a low impedance input bias. The former achieves a

higher IIP_3, but at the expense of high IIP_3 sensitivity to the frequencies of the input two tones. The second LNA still meets the IIP_3 requirement and with much less frequency sensitivity, which makes the low-frequency low-impedance input termination method more suitable for high volume production. Different techniques for generating the low-frequency low-impedance input termination are reviewed. Among them, only the combination of the low-impedance bias circuit with an RF choke can meet the CDMA LNA requirements to the bandwidth of the termination and to the gain switching time.

Although a very simple and reliable method, the low-frequency low-impedance input termination can only be used for BJTs or HBTs, but not FETs. And the latter are the only active devices available in CMOS technology, which offers a low cost: one of the key goals of the CDMA RX design. Among the linearization techniques suitable for FET LNAs, the optimum gate biasing is the simplest. It is based on biasing a FET at the gate-source voltage at which the 3rd-order derivative of its dc transfer characteristic is zero. Such biasing causes an IMD_3 null. However, this null is very narrow and, thus, requires precise biasing at the mentioned voltage. A novel bias circuit is proposed here to automatically generate this voltage in the presence of process and temperature variations. Its precision can be satisfactory, provided that the dc input offsets are reduced. In addition to being narrow, the IMD_3 null is shown to shift at RF from the bias voltage for zero 3rd-order derivative and become shallow, causing a lower IIP_3 peak. This behavior is theoretically attributed to the effect of the 2nd-order interaction, which becomes stronger at RF due to stronger parasitic feedbacks around a FET. An approach based on tuning the drain load

impedance is proposed to cancel the effect of the 2nd-order interaction on IIP_3 at RF. It is implemented in a cellular-band CMOS LNA. Even though this approach increases the IIP_3 peak, the latter remains shifted relative to the gate bias for zero 3rd-order derivative and, thus, requires a manual bias adjustment. It is shown experimentally that a current-derived bias of a linearized FET results in less IIP_3 variations from part to part than a voltage-derived bias. While IIP_3 of the designed LNA using the optimum gate biasing marginally meets the derived specification, the NF and gain of the LNA fall short of their requirements due to a low f_{T} at the optimum gate bias.

The DS method reduces the IIP_3 bias sensitivity, indicative of the previous method, by extending the bias voltage range in which a significant IIP_3 improvement is achieved. It also improves the amplifier gain by having one of the two parallel FETs operate in the SI region. However, the second-order interaction still degrades IIP_3 at RF. A modified DS method is proposed to cancel the 2nd-order contributions to IMD_3 against the 3rd-order ones. This method boosted the IIP_3 of a cellular-band CMOS LNA by 20dB. The LNA also showed an improved gain and NF in comparison with the LNA using the optimum gate bias. The measured NF is still higher than that of a single FET LNA. This result is theoretically explained by the contribution of the induced gate noise of the FET operating in the WI region to the overall noise of the composite FET. The measured results show that the van der Ziel noise theory, which was extended here for subthreshold biases, overestimates this NF degradation, which indicates its deficiency at these biases. The designed CMOS LNA using the modified DS method has the highest dynamic range FOM among known

state-of-the-art LNAs.

VII.2 Future Research Directions

Wireless networks will continue evolve towards higher cell capacity and higher data rate. The CDMA technology opens the doors for this evolution. This is why it has been chosen as a core of the 3G standards. However, the older standards such as AMPS and GSM will not disappear right away. They will coexist with the new standards, creating interferences to CDMA phones. Thus, XMD will continue to degrade the mobile RX sensitivity. Besides narrow-band jammers from AMPS or GSM offending base stations, there will be wideband jammers from the competitors' CDMA base stations. This interfering signal environment has already been considered by the 3G standards [152], [153]. It will be important to develop accurate behavioral models of XMD, which take into account the statistical properties of the TX leakage and jammer, generated using new coding and modulation schemes. One of these models has already been published [154].

The phone miniaturization and cost reduction will continue pushing for new, low-cost front-end solutions. Moving towards an all-CMOS implementation of the RX front end is one of the low-cost solutions. Therefore, FET linearization techniques will be of great interest; especially those suitable for low-supply voltages, which will dominate in the future due to the gate-length reduction trend. Another way to reduce the cost and area of a CDMA RX is to get rid of the RF SAW filter and the associated matching circuits at the LNA-mixer interface. Two researches will probably be conducted in parallel to investigate

the possibility of removing the RF SAW filter: one will concentrate on achieving a high TX-RX isolation of the duplexer in the TX band, and the other will concentrate on designing an active TX leakage filter.

The duplexer isolation can be improved by making the RX ports differential. The RX architecture would have to be fully differential too. With an improved TX-RX isolation, the requirements to the LNA linearity will become less stringent to the point that no special linearization techniques will be needed. However, without the RF SAW filter, the mixer will become a dominant XMD contributor, and its linearity will have to be improved. The modified DS method proposed here or the post-distortion method described in [95] can be used to linearize the mixer. However, they would have to be converted to the differential architecture. Some of the issues associated with these methods, such as the NF degradation, will have to be understood and resolved. For example, a more accurate FET noise theory for subthreshold biases is needed.

The research effort towards an active TX leakage filter would have to find a way to reject the TX leakage without significantly degrading the RX cascaded NF, gain, and current consumption. The filter will also have to automatically track the TX frequency. Such a self-tracking filter, based on the least-mean-square algorithm, has already been reported in [155]. However, its TX leakage rejection was limited by the reference signal leakage to the LNA output. The filter also degraded the LNA NF by 1.3dB, moving the RX cascaded NF above the acceptance level. More work will have to be done to increase the filter TX rejection and reduce the cascaded NF.

Appendix A

Derivation of Autocorrelation Function of OQPSK Signal and BPGN

This section derives the autocorrelation function of $c(t)$ given by (II.3), with $I(t)$ and $Q(t)$ given by (II.2a) and (II.2b), respectively. The statistical properties of i_k and q_k samples of $I(t)$ and $Q(t)$ for an OQPSK signal and BPGN are summarized in Table II.1.

Due to the randomness and zero crosscorrelation of ϕ and θ, the statistical properties of $c(t)$ are time-independent. So, each of the considered signals and its distortions are *stationary* processes under the made assumptions. To shorten the formulas, the time variable t will be set to zero in further derivations without losing accuracy.

By definition,

$$\begin{aligned} R_c(\tau) &= E\{c(0)c(\tau)\} \\ &= E_\theta\{\cos(\theta)\cos(\omega_{\mathrm{TX}}\tau+\theta)\}E\{I(0)I(\tau)\} \\ &\quad + E_\theta\{\sin(\theta)\sin(\omega_{\mathrm{TX}}\tau+\theta)\}E\{Q(0)Q(\tau)\}, \end{aligned} \tag{A.1a}$$

where the crosscorrelation terms between $I(t)$ and $Q(t)$ were omitted because they are zero. The average over θ can be computed as follows

$$E_\theta\{\} = \frac{1}{2\pi}\int_0^{2\pi}\{\}d\theta. \tag{A.2}$$

Both averages over θ in (A.1a) result in $0.5\cos(\omega_{\mathrm{TX}}\tau)$. Therefore,

$$R_c(\tau) = \frac{1}{2}\cos(\omega_{\mathrm{TX}}\tau)\left[E\{I(0)I(\tau)\} + E\{Q(0)Q(\tau)\}\right]. \tag{A.3}$$

The first term in the brackets of (A.3) can be evaluated as follows

$$\begin{aligned} E\{I(0)I(\tau)\} &= E_\phi\left\{\sum_{k=-\infty}^{\infty}\sum_{l=-\infty}^{\infty} E\{i_k i_l\}\,\mathrm{sinc}(\phi/\pi - k)\,\mathrm{sinc}(B\tau + \phi/\pi - l)\right\} \\ &= E_\phi\left\{\sum_{k=-\infty}^{\infty}\sum_{l=-\infty}^{\infty} \delta_{kl}\,\mathrm{sinc}(\phi/\pi - k)\,\mathrm{sinc}(B\tau + \phi/\pi - l)\right\} \\ &= E_\phi\left\{\sum_{k=-\infty}^{\infty} \mathrm{sinc}(\phi/\pi - k)\,\mathrm{sinc}(B\tau + \phi/\pi - k)\right\}, \end{aligned} \tag{A.4}$$

where we used the correlation propertied of i_k from Table II.1. Since these properties are the same for the OQPSK signal and BPGN, the present analysis is valid for both signals. The average over ϕ is defined as

$$E_\phi\{\} = \frac{1}{2\pi}\int_0^{2\pi}\{\}d\phi. \tag{A.5}$$

Applying the following identity, derived using the *Poisson sum formula* [125],

$$\sum_{k=-\infty}^{\infty}\mathrm{sinc}(\phi/\pi - k)\,\mathrm{sinc}(b\tau + \phi/\pi - k) = \mathrm{sinc}(b\tau), \tag{A.6}$$

we get

$$E\{I(0)I(\tau)\} = \mathrm{sinc}(b\tau). \tag{A.7}$$

It can be shown that $E\{Q(0)Q(\tau)\}$ gives the same result. Substituting $E\{I(0)I(\tau)\}$ and $E\{Q(0)Q(\tau)\}$ into (A.3), we get

$$R_c(\tau) = \cos(\omega_{\mathrm{TX}}\tau)\,\mathrm{sinc}(b\tau). \tag{A.8}$$

Appendix B

Example of Infinite Sum Evaluation Using MAPLE 7

This section demonstrates how to evaluate in closed form the infinite sums in (II.29). As an example, we use the last sum in this expression. This sum appears only in the case of a CDMA TX leakage and is absent in the case of BPGN.

Since most symbolic math packages do not recognize the sinc function, the first step is to replace it with its definition as follows

$$\sum_{k=-\infty}^{\infty} \operatorname{sinc}^2(\phi/\pi - k)\operatorname{sinc}^2(b\tau + \phi/\pi - k) = \sin^2(\phi)\sin^2(\pi b\tau + \phi)\sum_{k=-\infty}^{\infty} \frac{1}{(\phi - k\pi)^2(\pi b\tau + \phi - k\pi)^2}. \quad \text{(B.1)}$$

The following Maple 7 script finds the closed-form result of the above expression and averages it over ϕ.

```
> assume(b,real);# b denotes Pi*b*tau
> sin(phi)^2*sin(b+phi)^2*sum(1/(phi-k*Pi)^2/(b+phi-k*Pi)^2,
> k=-infinity..infinity):simplify(%):combine(%);# Evaluating the sum:
```

$$(b^{\sim} - \frac{1}{2}\, b^{\sim}\cos(2\, b^{\sim} + 2\,\phi) - \frac{1}{2}\, b^{\sim}\cos(2\,\phi) - \frac{1}{2}\sin(2\,\phi) - \frac{1}{2}\sin(2\, b^{\sim}) + \frac{1}{2}\sin(2\, b^{\sim} + 2\,\phi))/b^{\sim 3}$$

```
> convert(%,exp):simplify(%):1/2/Pi*int(%,phi=0..2*Pi):
> evalc(%):combine(%,trig);# Averaging over phi:
```

$$\frac{1}{2}\,\frac{2\,\tilde{b} - \sin(2\,\tilde{b})}{\tilde{b}^3}$$

Appendix C

Derivation of Volterra Series Coefficients of Common Emitter Circuit

In this section, the 1st and 3rd-order coefficients of the Volterra series (IV.8) are derived using the harmonic input method.

The Kirchhoff's current law equations for each node of the circuit in Fig. IV.1 are

$$\frac{v_{\rm x}-v_1}{Z_1(s)} - i_{\rm c}\left(\frac{1}{\beta_{\rm F}}+s\tau_{\rm F}\right) - (v_1-v_2)sC_{\rm je} - (v_1-v_3)sC_{\mu} = 0, \tag{C.1a}$$

$$i_{\rm c}\left(1+\frac{1}{\beta_{\rm F}}+s\tau_{\rm F}\right) + (v_1-v_2)sC_{\rm je} - \frac{v_2}{Z_2(s)} = 0, \tag{C.1b}$$

$$(v_1-v_3)sC_{\mu} - i_{\rm c} - \frac{v_3}{Z_3(s)} = 0. \tag{C.1c}$$

Equations (C.1) can be solved for v_1, v_2, and v_3 as functions of the excitation voltage $v_{\rm x}$ and the nonlinear collector current $i_{\rm c}$. Since the latter is controlled by v_π $(= v_1 - v_2)$ (see (IV.1)), it is convenient to combine the solutions for v_1 and v_2 into v_π. Then, we get

$$v_\pi = \frac{1}{g(s)}\left[\frac{v_{\rm x}b(s)}{a(s)Z_1(s)+(1+a(s))Z(s)} - i_{\rm c}\right], \tag{C.2a}$$

$$v_3 = Z_3(s)\frac{v_{\rm x}sC_{\mu}d(s) - i_{\rm c}\left[c(s)+d(s)+a(s)sC_{\mu}Z_1(s)\right]}{b(s)+c(s)+sC_{\rm je}Z(s)}, \tag{C.2b}$$

where the following shorthand notations were used

$$a(s) = \frac{1}{\beta_{\mathrm{F}}} + s\tau_{\mathrm{F}}, \tag{C.3a}$$

$$b(s) = 1 + sC_{\mu}Z_3(s), \tag{C.3b}$$

$$c(s) = s(C_{\mathrm{je}} + C_{\mu})Z_1(s), \tag{C.3c}$$

$$d(s) = 1 + sC_{\mathrm{je}}Z_2(s), \tag{C.3d}$$

$$g(s) = \frac{b(s) + c(s) + sC_{\mathrm{je}}Z(s)}{a(s)Z_1(s) + (1 + a(s))Z(s)}, \tag{C.3e}$$

$$Z(s) = Z_2(s) + sC_{\mu}\left[Z_1(s)Z_2(s) + Z_1(s)Z_3(s) + Z_2(s)Z_3(s)\right]. \tag{C.3f}$$

Equation (C.2b) can not be solved for v_3 directly because its right side includes i_{c}, which depends on v_{π}. Therefore, we will have to find v_{π} from (C.2a) first. Equation (C.2a) is transcendental because i_{c} is a nonlinear function of v_{π}. To find v_{π} as a function of v_{x}, we will use the following Volterra series representation for v_{π}:

$$v_{\pi} = A_1(s) \circ v_{\mathrm{x}} + A_2(s_1, s_2) \circ v_{\mathrm{x}}^2 + A_3(s_1, s_2, s_3) \circ v_{\mathrm{x}}^3 + \cdots \quad . \tag{C.4}$$

Substituting (C.4) into (IV.1), we get [15]

$$\begin{aligned} i_{\mathrm{c}} = {} & g_1 A_1(s) \circ v_{\mathrm{x}} + \left[g_1 A_2(s_1, s_2) + g_2 A_1(s_1) A_1(s_2)\right] \circ v_{\mathrm{x}}^2 \\ & + \left[g_1 A_3(s_1, s_2, s_3) + 2g_2 \overline{A_1(s_1) A_2(s_2, s_3)} + g_3 A_1(s_1) A_1(s_2) A_1(s_3)\right] \circ v_{\mathrm{x}}^3 + \cdots \quad , \end{aligned} \tag{C.5}$$

where the bar indicates the symmetrization (averaging) of the corresponding transfer function over all possible permutations of the Laplace variables, i.e.,

$$\overline{A_1(s_1)A_2(s_2, s_3)} = \frac{1}{3}\left[A_1(s_1)A_2(s_2, s_3) + A_1(s_2)A_2(s_1, s_3) + A_1(s_3)A_2(s_1, s_2)\right]. \tag{C.6}$$

The idea of the harmonic input method is that equations (C.2) must hold separately for the 1st-order (i.e., linear) terms as well as the 2nd and 3rd-order intermodulation products. To find the linear transfer functions $A_1(s)$ and $C_1(s)$, we will excite the circuit with a single tone $v_{\rm x} = e^{st}$. Substituting (C.5), (C.4), and (IV.8) into (C.2), equating the coefficients of e^{st} on both sides of (C.2), and solving for $A_1(s)$ and $C_1(s)$, we get

$$A_1(s) = \frac{1}{g_1 + g(s)} \cdot \frac{b(s)}{a(s)Z_1(s) + (1 + a(s))Z(s)} \tag{C.7a}$$

$$C_1(s) = Z_3(s)\frac{sC_\mu d(s) - g_1 A_1(s)\left[c(s) + d(s) + a(s)sC_\mu Z_1(s)\right]}{b(s) + c(s) + sC_{\rm je}Z(s)}. \tag{C.7b}$$

Among the 2nd-order transfer functions, we will only need $A_2(s_1, s_2)$ as will be seen later. To find it, we will excite the circuit with two tones $v_{\rm x} = e^{s_1 t} + e^{s_2 t}$. Substituting (C.5) and (C.4) into (C.2a), equating the coefficients of $e^{(s_1+s_2)t}$ on both sides of (C.2a), replacing s with $s_1 + s_2$, and solving for $A_2(s_1, s_2)$, we get

$$A_2(s_1, s_2) = -\frac{g_2 A_1(s_1)A_1(s_2)}{g_1 + g(s_1 + s_2)}. \tag{C.8}$$

Similarly, using a three tone excitation, we can derive

$$A_3(s_1, s_2, s_3) = -\frac{2g_2\overline{A_1(s_1)A_2(s_2, s_3)} + g_3 A_1(s_1)A_1(s_2)A_1(s_3)}{g_1 + g(s_\Sigma)}, \tag{C.9a}$$

$$\begin{aligned} C_3(s_1, s_2, s_3) = &-Z_3(s_\Sigma)\frac{c(s_\Sigma) + d(s_\Sigma) + a(s_\Sigma)s_\Sigma C_\mu Z_1(s_\Sigma)}{b(s_\Sigma) + c(s_\Sigma) + s_\Sigma C_{\rm je}Z(s_\Sigma)} \\ &\cdot \left[g_1 A_3(s_1, s_2, s_3) + 2g_2\overline{A_1(s_1)A_2(s_2, s_3)} + g_3 A_1(s_1)A_1(s_2)A_1(s_3)\right], \end{aligned} \tag{C.9b}$$

where $s_\Sigma = s_1 + s_2 + s_3$.

For the input excitation given by (IV.7), IMD_3 at $2\omega_{\rm b} - \omega_{\rm a}$ is found by setting $s_1 = s_2 = s_{\rm b}$ and $s_3 = -s_{\rm a}$. Assuming closely spaced frequencies such that $s_{\rm a} \approx s_{\rm b} \approx s$, we

can simplify (C.9) as follows

$$A_3(s_\mathrm{b}, s_\mathrm{b}, -s_\mathrm{a}) = -\frac{2g_2\overline{A_1(s_\mathrm{b})A_2(s_\mathrm{b}, -s_\mathrm{a})} + g_3 A_1(s)\left|A_1(s)\right|^2}{g_1 + g(s)}, \tag{C.10a}$$

$$\begin{aligned} C_3(s_\mathrm{b}, s_\mathrm{b}, -s_\mathrm{a}) = &-Z_3(s)\frac{c(s) + d(s) + a(s)sC_\mu Z_1(s)}{b(s) + c(s) + sC_\mathrm{je}Z(s)} \\ &\cdot \left[g_1 A_3(s_\mathrm{b}, s_\mathrm{b}, -s_\mathrm{a}) + 2g_2\overline{A_1(s_\mathrm{b})A_2(s_\mathrm{b}, -s_\mathrm{a})} + g_3 A_1(s)\left|A_1(s)\right|^2\right]. \end{aligned} \tag{C.10b}$$

Substituting (C.10a) into (C.10b), we get

$$\begin{aligned} C_3(s_\mathrm{b}, s_\mathrm{b}, -s_\mathrm{a}) = &-Z_3(s)\frac{c(s) + d(s) + a(s)sC_\mu Z_1(s)}{b(s) + c(s) + sC_\mathrm{je}Z(s)}\frac{g(s)}{g_1 + g(s)} \\ &\cdot \left[2g_2\overline{A_1(s_\mathrm{b})A_2(s_\mathrm{b}, -s_\mathrm{a})} + g_3 A_1(s)\left|A_1(s)\right|^2\right]. \end{aligned} \tag{C.11}$$

The averaged product $\overline{A_1(s_\mathrm{b})A_2(s_\mathrm{b}, -s_\mathrm{a})}$ can be evaluated using (C.6) and (C.8) as follows

$$\overline{A_1(s_\mathrm{b})A_2(s_\mathrm{b}, -s_\mathrm{a})} = -\frac{g_2}{3}A_1(s)\left|A_1(s)\right|^2\left[\frac{2}{g_1 + g(\Delta s)} + \frac{1}{g_1 + g(2s)}\right], \tag{C.12}$$

where $\Delta s = s_\mathrm{b} - s_\mathrm{a}$. Substituting (C.12) into (C.11), we get

$$C_3(s_\mathrm{b}, s_\mathrm{b}, -s_\mathrm{a}) = -Z_3(s)\frac{c(s) + d(s) + a(s)sC_\mu Z_1(s)}{b(s) + c(s) + sC_\mathrm{je}Z(s)}\frac{g(s)}{g_1 + g(s)}A_1(s)\left|A_1(s)\right|^2\varepsilon(\Delta s, 2s), \tag{C.13}$$

where

$$\varepsilon(\Delta s, 2s) = g_3 - \frac{2g_2^2}{3}\left[\frac{2}{g_1 + g(\Delta s)} + \frac{1}{g_1 + g(2s)}\right]. \tag{C.14}$$

To calculate IIP_3, we need to compute the ratio $C_1(s)/C_3(s_\mathrm{b}, s_\mathrm{b}, -s_\mathrm{a})$. Using (C.13) and (C.7b), we get

$$\frac{C_1(s)}{C_3(s_\mathrm{b}, s_\mathrm{b}, -s_\mathrm{a})} = \frac{1}{H(s)A_1(s)\left|A_1(s)\right|^2\varepsilon(\Delta s, 2s)}, \tag{C.15}$$

where

$$H(s) = -\frac{c(s) + d(s) + a(s)sC_\mu Z_1(s)}{sC_\mu d(s) - g_1 A_1(s)\left[c(s) + d(s) + a(s)sC_\mu Z_1(s)\right]} \cdot \frac{g(s)}{g_1 + g(s)}. \tag{C.16}$$

Substituting (C.7a) into (C.16) and expanding the shorthand notations (C.3), we can simplify (C.16) to

$$H(s) = \frac{1 + sC_{\mathrm{je}}\left[Z_1(s) + Z_2(s)\right] + sC_\mu Z_1(s)\left(1 + 1/\beta_{\mathrm{F}} + s\tau_{\mathrm{F}}\right)}{g_1 - sC_\mu\left[1 + Z_2(s)\left(g_1 + g_1/\beta_{\mathrm{F}} + s\tau_{\mathrm{F}} g_1 + sC_{\mathrm{je}}\right)\right]}. \tag{C.17}$$

Appendix D

Derivation of Noise Coefficients for a FET in Weak Inversion

This section derives the drain and induced gate noise coefficients for a saturated long-channel MOSFET biased in WI (M_{A} in Fig. VI.2), following the approach outlined by van der Ziel in [144]. For simplicity, the letter "A" in the subscripts of notations is omitted here.

To find the drain noise current, we will start with an expression for the drain current caused by the noise voltage Δv_{x0} across the channel section between x_0 and $x_0 + \Delta x_0$ [144]:

$$\Delta i_{\mathrm{nd}} = \frac{g(V_0)}{L_{\mathrm{eff}}} \Delta v_{x0}, \tag{D.1}$$

where $g(V_0)$ is the channel conductance per unit length at x_0 and V_0 is the dc potential at x_0. In the WI region, the drain current mechanism is due to diffusion. According to [145],

$$g(V_0) = g_0 e^{-\frac{V_0}{\phi_{\mathrm{t}}}}, \tag{D.2}$$

where g_0 is the channel conductance per unit length at the source terminal ($V_0 = 0$) and ϕ_{t} is the thermal voltage kT/q.

The mean-square value of Δi_{nd} is given by

$$\overline{\Delta i_{\mathrm{nd}}^2} = \frac{g^2(V_0)}{L_{\mathrm{eff}}^2} \overline{\Delta v_{x0}^2}, \tag{D.3}$$

where

$$\overline{\Delta v_{x0}^2} = 4kT\Delta f \frac{\Delta x_0}{g(V_0)} = 4kT\Delta f \frac{\Delta V_0}{I_{\rm D}}. \tag{D.4}$$

The total drain noise current can be found as follows:

$$\overline{i_{\rm nd}^2} = \int_0^{L_{\rm eff}} \frac{d\left(\overline{\Delta i_{\rm nd}^2}\right)}{dx} dx = \frac{4kT\Delta f}{L_{\rm eff}^2 I_{\rm D}} \int_0^{V_{\rm D}} g^2(V_0) dV_0, \tag{D.5}$$

where $V_{\rm D}$ is the dc drain potential (the source is assumed grounded). The last equation was first derived by Klaassen and Prins [146]. Substituting (D.2) into (D.5) and simplifying the result for $V_{\rm D} \gg \phi_{\rm t}$, we get

$$\overline{i_{\rm nd}^2} \approx 2kT\Delta f \frac{g_0^2 \phi_{\rm t}}{L_{\rm eff}^2 I_{\rm D}}. \tag{D.6}$$

We also know that

$$I_{\rm D} = \frac{1}{L_{\rm eff}} \int_0^{V_{\rm D}} g(V_0) dV_0. \tag{D.7}$$

Substituting (D.2) into (D.7), we get

$$I_{\rm D} = \frac{g_0 \phi_{\rm t}}{L_{\rm eff}} \left(1 - e^{-\frac{V_{\rm D}}{\phi_{\rm t}}}\right). \tag{D.8}$$

For $V_{\rm D} \gg \phi_{\rm t}$, the above expression simplifies to

$$I_{\rm D} \approx \frac{g_0 \phi_{\rm t}}{L_{\rm eff}}. \tag{D.9}$$

Solving for g_0 in (D.9) and substituting it to (D.6), we get

$$\overline{i_{\rm nd}^2} = 2kT\Delta f \frac{I_{\rm D}}{\phi_{\rm t}} = 2qI_{\rm D}\Delta f. \tag{D.10}$$

Using (D.8) and (D.9), we can also find

$$g_{\rm d0} = \left.\frac{\partial I_{\rm D}}{\partial V_{\rm D}}\right|_{V_{\rm D}=0} = \frac{g_0}{L_{\rm eff}} \approx \frac{I_{\rm D}}{\phi_{\rm t}}, \tag{D.11}$$

and, thus,

$$\overline{i_{\rm nd}^2} = 2kT\Delta f g_{\rm d0}. \tag{D.12}$$

A comparison of (D.12) with (VI.1) yields $\gamma = 1/2$.

In the first-order approximation, the gate current caused by the noise voltage Δv_{x0} is given by [144], [147]:

$$\Delta i_{\rm ng} = j\omega C_{\rm ox} W g(V_0)\Delta v_{x0}\left[\int_{V_0}^{V_{\rm D}} \frac{dx}{g(V)} - \int_0^{V_{\rm D}} \frac{xdx}{L_{\rm eff} g(V)}\right] \tag{D.13}$$

We know that [144], [147]

$$dx = \frac{g(V)dV}{I_{\rm D}}, \tag{D.14}$$

and, therefore,

$$x = \int_0^V \frac{g(u)du}{I_{\rm D}} = \frac{g_0\phi_{\rm t}}{I_{\rm D}}\left(1 - e^{-\frac{V}{\phi_{\rm t}}}\right). \tag{D.15}$$

Substituting (D.14), (D.15), and (D.2) into (D.13) and simplifying the result for $V_{\rm D} \gg \phi_{\rm t}$, we get

$$\Delta i_{\rm ng} \approx \frac{j\omega C_{\rm ox} W g(V_0)\Delta v_{x0}}{I_{\rm D}}(\phi_{\rm t} - V_0). \tag{D.16}$$

The total induced gate noise current is

$$\begin{aligned}\overline{i_{\rm ng}^2} &= \int_0^{L_{\rm eff}} \frac{d\left(\overline{\Delta i_{\rm ng}^2}\right)}{dx}dx \\ &= 4kT\Delta f\frac{\omega^2 C_{\rm ox}^2 W^2}{I_{\rm D}^3}\int_0^{V_{\rm D}} g^2(V_0)(\phi_{\rm t} - V_0)^2 dV_0 \\ &\approx kT\Delta f\omega^2 C_{\rm ox}^2 W^2 L_{\rm eff}^2\frac{\phi_{\rm t}}{I_{\rm D}}.\end{aligned} \tag{D.17}$$

Taking into account (D.11), we can write

$$\overline{i_{\rm ng}^2} = kT\Delta f\frac{\omega^2(C_{\rm ox} W L_{\rm eff})^2}{g_{\rm d0}}. \tag{D.18}$$

A comparison of (D.18) with (VI.2) yields $\delta = 45/16$.

To find the correlation coefficient between $i_{\rm ng}$ and $i_{\rm nd}$, we need the following cross-correlation

$$\overline{i_{\rm ng} i_{\rm nd}^*} = \int_0^{L_{\rm eff}} \frac{d\left(\overline{\Delta i_{\rm ng} \Delta i_{\rm nd}^*}\right)}{dx} dx. \tag{D.19}$$

Substituting (D.16) and (D.1) into (D.19) and taking into account (D.4), we get

$$\begin{aligned} \overline{i_{\rm ng} i_{\rm nd}^*} &= 4kT\Delta f \frac{j\omega C_{\rm ox} W}{I_{\rm D}^2 L_{\rm eff}} \int_0^{V_{\rm D}} g^2(V_0)(\phi_{\rm t} - V_0) dV_0 \\ &\approx kT\Delta f j\omega C_{\rm ox} W L_{\rm eff}. \end{aligned} \tag{D.20}$$

Finally, the correlation coefficient

$$c = \frac{\overline{i_{\rm ng} \cdot i_{\rm nd}^*}}{\sqrt{i_{\rm ng}^2 \cdot i_{\rm nd}^2}} = \frac{j}{\sqrt{2}}. \tag{D.21}$$

Appendix E

Derivation of Volterra Series Coefficients in Modified DS Method

In this section, the 1st and 3rd-order coefficients of the Volterra series (VI.12) are derived using the harmonic input method.

First, we will establish the relationship between the combined output current i and the gate-source voltages v_{A} and v_{B}. From Fig. VI.5,

$$i_{\mathrm{A}} = g_{3\mathrm{A}} v_{\mathrm{A}}^3, \tag{E.1a}$$

$$i_{\mathrm{B}} = g_{1\mathrm{B}} v_{\mathrm{B}} + g_{2\mathrm{B}} v_{\mathrm{B}}^2 + g_{3\mathrm{B}} v_{\mathrm{B}}^3, \tag{E.1b}$$

$$i = i_{\mathrm{A}} + i_{\mathrm{B}} = g_{3\mathrm{A}} v_{\mathrm{A}}^3 + g_{1\mathrm{B}} v_{\mathrm{B}} + g_{2\mathrm{B}} v_{\mathrm{B}}^2 + g_{3\mathrm{B}} v_{\mathrm{B}}^3. \tag{E.1c}$$

The gate-source voltages can be modeled by the following truncated Volterra series in terms of the excitation voltage v_{x}:

$$v_{\mathrm{A}} = A_1(s) \circ v_{\mathrm{x}} + A_2(s_1, s_2) \circ v_{\mathrm{x}}^2 + A_3(s_1, s_2, s_3) \circ v_{\mathrm{x}}^3, \tag{E.2a}$$

$$v_{\mathrm{B}} = B_1(s) \circ v_{\mathrm{x}} + B_2(s_1, s_2) \circ v_{\mathrm{x}}^2 + B_3(s_1, s_2, s_3) \circ v_{\mathrm{x}}^3. \tag{E.2b}$$

Substituting (E.2) into (E.1c) and comparing the resulting expression with (VI.12), we can

write

$$C_1(s) = g_{1\mathrm{B}} B_1(s), \tag{E.3a}$$

$$\begin{aligned} C_3(s_1, s_2, s_3) = {} & g_{3\mathrm{A}} A_1(s_1) A_1(s_2) A_1(s_3) + g_{1\mathrm{B}} B_3(s_1, s_2, s_3) \\ & + 2 g_{2\mathrm{B}} \overline{B_1(s_1) B_2(s_2, s_3)} + g_{3\mathrm{B}} B_1(s_1) B_1(s_2) B_1(s_3), \end{aligned} \tag{E.3b}$$

where the bar indicates the symmetrization (averaging) of the corresponding transfer function over all possible permutations of the Laplace variables, i.e.,

$$\overline{B_1(s_1) B_2(s_2, s_3)} = \frac{1}{3} \left[B_1(s_1) B_2(s_2, s_3) + B_1(s_2) B_2(s_1, s_3) + B_1(s_3) B_2(s_1, s_2) \right]. \tag{E.3c}$$

Therefore, to find $C_1(s)$ and $C_3(s_1, s_2, s_3)$, we first need to find $A_1(s)$, $B_1(s)$, $B_2(s_1, s_2)$, and $B_3(s_1, s_2, s_3)$.

The Kirchhoff's current law equations for each node of the circuit in Fig. VI.5 are

$$\frac{v_{\mathrm{x}} - v_0}{Z_1(s)} + (v_1 - v_0) s C_{\mathrm{A}} + (v_2 - v_0) s C_{\mathrm{B}} = 0, \tag{E.4a}$$

$$(v_0 - v_1) s C_{\mathrm{A}} + i_{\mathrm{A}} + \frac{v_2 - v_1}{s L_2} - \frac{v_1}{s L_1} = 0, \tag{E.4b}$$

$$(v_0 - v_2) s C_{\mathrm{B}} + i_{\mathrm{B}} + \frac{v_1 - v_2}{s L_2} = 0. \tag{E.4c}$$

Solving these equations for v_0, v_1, and v_2 and substituting the solutions into $v_{\mathrm{A}} = v_0 - v_1$ and $v_{\mathrm{B}} = v_0 - v_2$, we get

$$v_{\mathrm{A}} = \frac{v_{\mathrm{x}} a(s) - i_{\mathrm{A}} a(s) b(s) l - i_{\mathrm{B}} b(s) c(s)}{a(s) d(s) - c(s)}, \tag{E.5a}$$

$$v_{\mathrm{B}} = \frac{v_{\mathrm{x}} - i_{\mathrm{A}} b(s) l - i_{\mathrm{B}} b(s) d(s)}{a(s) d(s) - c(s)}, \tag{E.5b}$$

where

$$l = \frac{L_1}{L_2}, \tag{E.5c}$$

$$a(s) = 1 + s^2 L_2 C_{\mathrm{B}}, \tag{E.5d}$$

$$b(s) = sL_2, \tag{E.5e}$$

$$c(s) = l - sC_{\mathrm{B}} Z_1(s), \tag{E.5f}$$

$$d(s) = 1 + l + sC_{\mathrm{A}}(Z_1(s) + sL_1). \tag{E.5g}$$

Equations (E.5) are the starting point for derivations of the transfer functions of (E.2).

To find the linear transfer functions $A_1(s)$ and $B_1(s)$, we will excite the circuit with a single tone $v_{\mathrm{x}} = e^{st}$. Substituting (E.1a), (E.1b), and (E.2) into (E.5), equating the coefficients of e^{st} on both sides of (E.5), and solving for $A_1(s)$ and $B_1(s)$, we get

$$A_1(s) = n(s) B_1(s), \tag{E.6a}$$

$$B_1(s) = \frac{1}{a(s)d(s) - c(s) + g_{1\mathrm{B}} b(s) d(s)}, \tag{E.6b}$$

where

$$n(s) = a(s) + g_{1\mathrm{B}} b(s). \tag{E.7}$$

To find the 2nd-order transfer function $B_2(s_1, s_2)$, we will excite the circuit with two tones $v_{\mathrm{x}} = e^{s_1 t} + e^{s_2 t}$. Substituting (E.1a), (E.1b), and (E.2b) into (E.5b), equating the coefficients of $e^{(s_1+s_2)t}$ on both sides of (E.5b), replacing s with $s_1 + s_2$, and solving for $B_2(s_1, s_2)$, we get

$$B_2(s_1, s_2) = -g_{2\mathrm{B}} b(s_1 + s_2) d(s_1 + s_2) B_1(s_1 + s_2) B_1(s_1) B_1(s_2). \tag{E.8}$$

Similarly, using a three tone excitation, we can derive

$$B_3(s_1,s_2,s_3) = -b(s_1+s_2+s_3)B_1(s_1+s_2+s_3) \cdot\Big\{d(s_1+s_2+s_3)\left[g_{3\mathrm{B}}B_1(s_1)B_1(s_2)B_1(s_3)+2g_{2\mathrm{B}}\overline{B_1(s_1)B_2(s_2,s_3)}\right] + lg_{3\mathrm{A}}A_1(s_1)A_1(s_2)A_1(s_3)\Big\}. \tag{E.9}$$

For the input excitation given by (VI.13), IMD_3 at $2\omega_\mathrm{b}-\omega_\mathrm{a}$ is found by setting $s_1=s_2=s_\mathrm{b}$ and $s_3=-s_\mathrm{a}$. Assuming closely spaced frequencies such that $s_\mathrm{a}\approx s_\mathrm{b}\approx s$, we can simplify (E.9) and (E.3c) as follows

$$B_3(s_\mathrm{b},s_\mathrm{b},-s_\mathrm{a}) = -b(s)B_1(s) \cdot\Big\{d(s)\left[g_{3\mathrm{B}}B_1(s)\left|B_1(s)\right|^2+2g_{2\mathrm{B}}\overline{B_1(s_\mathrm{b})B_2(s_\mathrm{b},-s_\mathrm{a})}\right] + lg_{3\mathrm{A}}A_1(s)\left|A_1(s)\right|^2\Big\}, \tag{E.10}$$

$$\overline{B_1(s_\mathrm{b})B_2(s_\mathrm{b},-s_\mathrm{a})} = \frac{1}{3}\left[2B_1(s_\mathrm{b})B_2(s_\mathrm{b},-s_\mathrm{a})+B_1(-s_\mathrm{a})B_2(s_\mathrm{b},s_\mathrm{b})\right]. \tag{E.11}$$

Substituting (E.8) into (E.11), we get

$$\overline{B_1(s_\mathrm{b})B_2(s_\mathrm{b},-s_\mathrm{a})} = -\frac{g_{2\mathrm{B}}B_1(s_\mathrm{b})^2B_1(-s_\mathrm{a})}{3}\left[2b(\Delta s)d(\Delta s)B_1(\Delta s) + b(2s_\mathrm{b})d(2s_\mathrm{b})B_1(2s_\mathrm{b})\right], \tag{E.12}$$

where $\Delta s = s_\mathrm{b}-s_\mathrm{a}$. From the assumption that $s_\mathrm{a}\approx s_\mathrm{b}$, it follows that $\Delta s\approx 0$ and $b(\Delta s)\approx 0$. Then, (E.12) simplifies to

$$\overline{B_1(s_\mathrm{b})B_2(s_\mathrm{b},-s_\mathrm{a})} \approx -\frac{g_{2\mathrm{B}}B_1(s)|B_1(s)|^2}{3}b(2s)d(2s)B_1(2s). \tag{E.13}$$

Substituting (E.13) and (E.6a) into (E.10), we get

$$B_3(s_\mathrm{b}, s_\mathrm{b}, -s_\mathrm{a}) = -b(s)B_1(s)^2|B_1(s)|^2 \cdot\left\{d(s)\left[g_{3\mathrm{B}} - \frac{2g_{2\mathrm{B}}^2}{3}b(2s)d(2s)B_1(2s)\right] + lg_{3\mathrm{A}}n(s)|n(s)|^2\right\}. \quad \text{(E.14)}$$

Substituting (E.14), (E.13), and (E.6a) into (E.3b), we get

$$C_3(s_\mathrm{b}, s_\mathrm{b}, -s_\mathrm{a}) = B_1(s)|B_1(s)|^2 \cdot\left\{g_{3\mathrm{A}}n(s)|n(s)|^2\left[1 - lg_{1\mathrm{B}}b(s)B_1(s)\right] + \left[1 - g_{1\mathrm{B}}b(s)d(s)B_1(s)\right]\left[g_{3\mathrm{B}} - \frac{2g_{2\mathrm{B}}^2}{3}b(2s)d(2s)B_1(2s)\right]\right\}. \quad \text{(E.15)}$$

To simplify (E.15), we will consider the case of the conjugately matched input at the fundamental frequency, i.e.,

$$Z_1(s) = Z_{\text{in}}(-s), \quad \text{(E.16)}$$

where $Z_{\text{in}}(s)$ is the input impedance of the circuit given by

$$Z_{\text{in}}(s) = sL_1 + \frac{1 + s(L_1 + L_2)g_{1\mathrm{B}} + s^2L_2C_\mathrm{B}}{s(C_\mathrm{A} + C_\mathrm{B} + sL_2C_\mathrm{A}g_{1\mathrm{B}} + s^2L_2C_\mathrm{A}C_\mathrm{B})}. \quad \text{(E.17)}$$

In this case,

$$1 - g_{1\mathrm{B}}b(s)d(s)B_1(s) = 1/2. \quad \text{(E.18)}$$

We will further assume that

$$\omega^2 L_1 C_{\mathrm{A}} \ll \frac{\omega}{\omega_{\mathrm{TB}}}, \tag{E.19a}$$

$$\omega^2 L_2 C_{\mathrm{B}} \ll 1/4, \tag{E.19b}$$

$$\Re(Z_1(2s)) \ll (L_1 + L_2) \cdot \min\left(\omega_{\mathrm{TB}}, \frac{g_{1\mathrm{B}}}{C_{\mathrm{A}}}\right), \tag{E.19c}$$

$$|\Im(Z_1(2s))| \ll \frac{1}{2\omega \cdot \max(C_{\mathrm{A}}, C_{\mathrm{B}})}, \tag{E.19d}$$

where $\omega_{\mathrm{TB}} = g_{1\mathrm{B}}/C_{\mathrm{B}}$. The last two assumptions call for a relatively low impedance presented to the composite FET gate at the 2nd-harmonic frequency. They are not necessary for the proposed modified DS method to work and are only used here to simplify expressions for demonstration purposes. Using (E.19), we can write

$$n(s) \approx 1 + g_{1\mathrm{B}} s L_2, \tag{E.20a}$$

$$1 - l g_{1\mathrm{B}} b(s) B_1(s) \approx \frac{1}{2}\left[1 + \frac{L_2 C_{\mathrm{B}}}{L_1(C_{\mathrm{A}} + C_{\mathrm{B}}) + L_2 C_{\mathrm{B}}}\right], \tag{E.20b}$$

$$b(2s) d(2s) B_1(2s) \approx \frac{1}{g_{1\mathrm{B}} + \dfrac{1}{2s(L_1 + L_2)}}. \tag{E.20c}$$

Substituting (E.18) and (E.20) into (E.15), we get

$$C_3(s_{\mathrm{b}}, s_{\mathrm{b}}, -s_{\mathrm{a}}) = \frac{1}{2} B_1(s) |B_1(s)|^2 \varepsilon, \tag{E.21a}$$

where

$$\begin{aligned}\varepsilon \approx\ & g_{3\mathrm{A}}(1 + s L_2 g_{1\mathrm{B}})\left[1 + (\omega L_2 g_{1\mathrm{B}})^2\right]\left[1 + \frac{L_2 C_{\mathrm{B}}}{L_1(C_{\mathrm{A}} + C_{\mathrm{B}}) + L_2 C_{\mathrm{B}}}\right] \\ & + g_{3\mathrm{B}} - \frac{2 g_{2\mathrm{B}}^2}{3 g_{1\mathrm{B}}} \frac{1}{1 + \dfrac{1}{2s(L_1 + L_2) g_{1\mathrm{B}}}}.\end{aligned} \tag{E.21b}$$

For IIP_3 derivations, the following quantity will also be needed

$$\Re(Z_1(s))|B_1(s)|^2 \approx \frac{1}{4g_{1\mathrm{B}}\omega^2[L_1(C_\mathrm{A}+C_\mathrm{B})+L_2C_\mathrm{B}]}. \tag{E.22}$$

Bibliography

[1] T. Rappaport, *Wireless Communications - Principles and Practice*, Prentice Hall, 2002.

[2] *TIA/EIA/IS-95 Mobile Station - Base Station Compatability Standard for Dualmode Wideband Spread Spectrum Cellular System*, July 1995.

[3] J. F. Sevic, M. B. Steer, and A. M. Pavio, "Nonlinear analysis methods for digital wireless communication systems," *Int. J. of Microwave and Millimeter-Wave CAE*, vol. 6, no. 3, pp. 197-216, 1996.

[4] S. L. Loyka and J. R. Mosig, "New behavioral-level simulation techniques for RF/microwave applications," *RF and Microwave CAE*, vol. 10, no. 4, pp. 221-252, July 2000.

[5] S. Ciccarelli, "Cross modulation and phase noise effects in single-tone desense," *QUALCOMM Internal Memorandum*, Sept. 1998.

[6] K. Gard, H. Gutierrez, and M. Steer, "Characterization of spectral regrowth in microwave amplifiers based on the nonlinear transformation of a complex Gaussian process," *IEEE Trans. Microwave Theory Tech.*, vol. 47, no. 7, pp. 1059-1069, July 1999.

[7] G. T. Zhou and J. S. Kenney, "Predicting spectral regrowth of nonlinear power amplifiers," *IEEE Trans. Commun.*, vol. 50, no. 5, pp. 718-722, May 2002.

[8] Q. Wu, M. Testa, and R. Larkin, "On design of linear RF power amplifier for CDMA signals," *Int. J. RF and Microwave CAE*, vol. 8, no. 3, pp. 283-292, 1998.

[9] V. Aparin, "Analysis of CDMA signal spectral regrowth and waveform quality," *IEEE Trans. Microwave Theory Tech.*, vol. 49, no. 12, pp. 2306-2314, Dec. 2001.

[10] D. D. Weiner and J. F. Spina, *Sinusoidal Analysis and Modeling of Weakly Nonlinear Circuits*, New York, Van Nostrand Reinhold, 1980.

[11] N. M. Blachman, *Noise and its Effect on Communication*. 2nd ed., Malabar, FL: Krieger, 1982.

[12] J. C. Pedro and N. B. Carvalho, "On the use of multitone techniques for assessing RF components' intermodulation distortion," *IEEE Trans. Microwave Theory Tech.*, vol. 47, no. 12, pp. 2393-2402, Dec. 1999.

[13] R. Mohindra, "Cross modulation and linearization in CDMA mobile phone transceivers," *Wireless Symp./Portable by Design*, Feb. 22-26, 1999.

[14] W. H. Y. Chan and G. Bck, "Linearization of receivers using envelope signal injection," *IEEE Microwave & Wireless Components Lett.*, vol. 14, no. 7, pp. 325-327, July 2004.

[15] Rober Meyer, *Advanced Integrated Circuits for Communications*, UC Berkeley EECS 242 Course Notes, 1995.

[16] O. Shana'a, I. Linscott, and L. Tyler, "Frequency-scalable SiGe bipolar RF front-end design," *IEEE J. Solid-State Circuits*, vol. 36, no. 6, pp. 888-895, June 2001.

[17] J. Lee, W. Kim, Y. Kim, T. Rho, and B. Kim, "Intermodulation mechanism and linearization of GaAlAs/GaAs HBTs," *IEEE Trans. Microwave Theory Tech.*, vol. 45, no. 12, pp. 2065-2072, Dec. 1997.

[18] K. W. Kobayashi, A. K. Oki, J. C. Cowles, L. T. Tran, P. C. Grossman, T. R. Block, and D. C. Streit, "The voltage-dependent IP3 performance of a 35-GHz InAlAs/InGaAs-InP HBT amplifier," *IEEE Microwave & Guided Wave Lett.*, vol. 7, pp. 66-68, March 1997.

[19] K. W. Kobayashi, J. C. Cowles, L. T. Tran, A. Gutierrez-Aitken, M. Nishimoto, J. H. Elliot, T. R. Block, A. K. Oki, and D. C. Streit, "A 44-GHz high IP3 InP HBT MMIC amplifier for low dc power millimeter-wave receiver applications,"*IEEE J. Solid-State Circuits*, vol. 34, no. 2, pp. 1188-1195, Sept. 1999.

[20] G. Niu, Q. Liang, J. D. Cressler, C. S. Webster, and D. L. Harame, "RF linearity characteristics of SiGe HBTs," *IEEE Trans. Microwave Theory Tech.*, vol. 49, no. 9, pp. 1558-1565, Sept. 2001.

[21] M. Iwamoto, P. M. Asbeck, T. S. Low, C. P. Hutchinson, J. B. Scott, A. Cognata, X. Qin, L. H. Camnitz, and D. C. D'Avanzo, "Linearity characteristics of GaAs HBTs and the influence of collector design," *IEEE Trans. Microwave Theory Tech.*, vol. 48, no. 12, pp. 2377-2388, Dec. 2000.

[22] M. Vaidyanathan, M. Iwamoto, L. E. Larson, P. S. Gudem, and P. M. Asbeck, "A theory of high-frequency distortion in bipolar transistors," *IEEE Trans. Microwave Theory Tech.*, vol. 51, no. 2, pp. 448-461, Feb. 2003.

[23] S. Kang, B. Choi, and B. Kim, "Linearity analysis of CMOS for RF application," *IEEE Trans. Microwave Theory Tech.*, vol. 51, no. 3, pp. 972-977, March 2003.

[24] P. Rodgers, M. Megahed, C. Page, J. Wu, and D. Staab, “Silicon UTSi CMOS RFIC for CDMA wireless communications systems,” *IEEE RFIC Symp. Dig.*, pp. 181-184, June 1999.

[25] S. A. Maas and D. Neilson, “Modeling MESFETs for intermodulation analysis of mixers and amplifiers”, *IEEE Trans. Microwave Theory Tech.*, vol. 38, no. 12, pp. 1964-1971, Dec. 1990.

[26] J. C. Pedro and J. Perez, “Accurate simulation of GaAs MESFET’s intermodulation distortion using a new drain-source current model,” *IEEE Trans. Microwave Theory Tech.*, vol. 42, no. 1, pp. 25-33, Jan. 1994.

[27] G. Qu and A. E. Parker “Analysis of intermodulation nulling in HEMTs,” *Conf. on Optoelectr. & Microelectr. Mat. & Dev.*, pp. 227-230, Dec. 1996.

[28] M. T. Terrovitis and R. G. Meyer, “Intermodulation distortion in current-commutating CMOS mixers,” *IEEE J. Solid-State Circ.*, vol. 35, no. 10, pp. 565-567, Oct. 2000.

[29] P. H. Woerlee, M. J. Knitel, R. van Langevelde, D. B. M. Klaassen, L. F. Tiemeijer, A. J. Scholten, and A. T. A. Zegers-van Duijnhoven, “RF-CMOS performance trends”, *IEEE Trans. Electron Devices*, vol. 48, no. 8, pp. 1776-1782, Aug. 2001.

[30] C. Fager, N. B. de Carvalho, J. C. Pedro, and H. Zirath, “Intermodulation distortion behavior in LDMOS transistor amplifiers,” *IEEE MTT-S Int. Microwave Symp. Dig.*, vol. 1, pp. 131-134, June 2002.

[31] B. Toole, C. Plett, and M. Cloutier, “RF circuit implications of moderate inversion enhanced linear region in MOSFETs,” *IEEE Trans. Circ. & Sys. I*, vol. 51, no. 2, pp. 319-328, Feb. 2004.

[32] H. S. Black,“Stabilised Feedback Amplifiers”,*Bell System Tech. Journal*, vol. 13, no. 1, pp. 1-18, 1934.

[33] W. Sansen, “Distortion in elementary transistor circuits,” *IEEE Trans. Circ. & Sys. II*, vol. 46, no. 3, pp. 315-325, March 1999.

[34] G. V. Klimovitch, “On robust suppression of third-order intermodulation terms in small-signal bipolar amplifiers,” *IEEE MTT-S Int. Microwave Symp. Dig.*, vol. 1, pp. 477-479, June 2000.

[35] B. Razavi, *RF Microelectronics*. Prentice Hall, 1998.

[36] D. K. Shaeffer and T. H. Lee, “A 1.5-V, 1.5-GHz CMOS low noise amplifier,” *IEEE J. Solid-State Circuits*, vol. 32, no. 5, pp. 745-759, May 1997.

[37] F. Iturbide-Sanchez, H. Jardon-Aguilar, and J. A. Tirado-Mendez, "Comparison of different high-linear LNA structures for PCS applications using SiGe HBT and low bias voltage," *Electron. Lett.*, vol. 38, no. 12, pp. 536-538, June 2002.

[38] R. W. Ketchledge, "Distortion in feedback amplifiers," *Bell Syst. Tech. J.*, vol. 34, pp. 1265-1285, Nov. 1955.

[39] S. Narayannan, "Application of Volterra series to intermodulation distortion analysis of transistor feedback amplifies," *IEEE Trans. Circuit Theory*, vol. 17, no. 4, pp. 518-527, Nov. 1970.

[40] A. H. J. N. Dijkum and J. J. Sips, "Cross modulation and modulation distortion in A.M. receivers equipped with transistors," *Electronic Applications*, vol. 20, no.3, pp. 107-127, 1959-1960.

[41] D. D. Weiner, K. L. Su, and J. F. Spina, "Reduction of circuit intermodulation distortion via the design of linear out-of-band behaviour," *IEEE Int. Symp. on Electromag. Compat.*, pp. 6BIg/1-4, 7-9 Oct. 1975.

[42] F. N. Sechi, "Linearized Class-B Transistor Amplifiers," *IEEE J. Solid-State Circuits*, vol. 11, pp. 264-270, April 1976.

[43] K. Vennema, "Ultra Low Noise Amplifiers for 900 and 2000 MHz with High IIP3," *Philips Semiconductors App. Note*, Dec. 1996.

[44] J. Durec, "An integrated silicon bipolar receiver subsystem for 900-MHz ISM band applications," *IEEE J. Solid-State Circuits*, vol. 33, no. 9, pp. 1352-1372, Sept. 1998.

[45] J. Lucek and R. Damen, "Designing an LNA for a CDMA front end," *RF Design*, pp. 20-30, Feb. 1999.

[46] K. L. Fong, "High-frequency analysis of linearity improvement technique of common-emitter trans-conductance stage using a low-frequency trap network," *IEEE J. of Solid-State Circuits*, vol. 35, no. 8, pp. 1249-1252, Aug. 2000.

[47] P. Shah, P. Gazzerro, V. Aparin, R. Sridhara, and C. Narathong, "A 2GHz low-distortion low-noise two-stage LNA employing low-impedance bias terminations and optimum inter-stage match for linearity," *Europ. Solid-State Circ. Conf.*, pp. 213-216, Sept. 2000.

[48] G. Wevers, "A high IIP3 low noise amplifier for 1900 MHz Applications using the SiGe BFP620 transistor," *Appl. Microwave & Wireless*, vol. 12, no. 7, pp. 64-80, July 2000.

[49] G. Watanabe, H. Lau, T. Schlitz, and R. Holbrook, "IP3 boost circuitry for highly linear CDMA low noise amplifiers (LNA)," *Asia Pacific Microwave Conf.*, pp. 213-214, Dec. 3-6, 2000.

[50] J. Vuolevi and T. Rahkonen, “The effects of source impedance on the linearity of BJT common-emitter amplifiers,” *IEEE Int. Symp. on Circ. and Syst.*, vol. IV, pp. 197-200, May 28-31, 2000.

[51] J.-S. Ko, H.-S. Kim, B.-K. Ko, B. Kim, and B.-H. Park, “Effect of bias scheme on intermodulation distortion and its use for the design of PCS TX driver,” *IEEE RFIC Symp.*, pp. 105-108, 2000.

[52] B.-K. Ko, J.-S. Ko, H.-S. Kim, B. Kim, and B.-H. Park, “A new linearity enhancing technique for ultra-wide dynamic range low noise amplifiers,” *2nd Int. Conf. Microwave and Millimetr Wave Technology*, pp. 150-152, Sept. 2000.

[53] V. Aparin, E. Zeisel, and P. Gazzerro, “Highly linear SiGe BiCMOS LNA and mixer for cellular CDMA/AMPS applications,” *IEEE RFIC Symp.*, pp. 129-132, June 2002.

[54] J. Lee, G. Lee, G. Niu, J. D. Cressler, J. H. Kim, J. C. Lee, B. Lee, and N. Y. Kim, “The design of SiGe HBT LNA for IMT-2000 mobile application,” *IEEE MTT-S Int. Microwave Symp. Dig.*, pp. 1261-1264, 2002.

[55] L. Sheng and L. E. Larson, “An Si/SiGe BiCMOS direct-conversion mixer with second-order and third-order nonlinearity cancellation for WCDMA applications,” *IEEE Trans. Microwave Theory Tech.*, vol. 51, no. 11, pp. 2211-2220, Nov. 2003.

[56] H. Waite, P. Ta, J. Chen, H. Li, M. Gao, C. S. Chang, Y. S. Chang, W. Redman-White, O. Charlon, Y. Fan, R. Perkins, D. Brunel, E. Soudee, N. Lecacheur, and S. Clamagirand, “A CDMA2000 zero-IF receiver with low-leakage integrated front-end,” *IEEE J. of Solid-State Circuits*, vol. 39, no. 7, pp. 1175-1179, July 2004.

[57] J. Sevic, K. Burger, and M. Steer, “A Novel Envelope-Termination Load-Pull Method for ACPR Optimization of RF/Microwave Power Amplifiers,” *IEEE MTT-S Int. Microwave Symp. Dig.*, pp. 723-726, 1998.

[58] S. Watanabe, S. Takatuka, and K. Takagi, “Simulation and Experimental Results of Source Harmonic Tuning on Linearity of Power GaAs FET under Class AB Operation,” *IEEE MTT-S Int. Microwave Symp. Dig.*, pp. 1771-1774, 1996.

[59] R. Nagy, J. Bartolic, and B. Modlic, “GaAs MESFET small signal amplifier intermodulation distortion improvement by the second harmonic termination,” *MELECON 98*, vol. 1, pp. 358-361, May 1998.

[60] T. Y. Yum, Q. Xue, and C. H. Chan, “Amplifier linearization using compact microstrip resonant cell - theory and experiment,” *IEEE Trans. Microwave Theory Tech.*, vol. 52, no. 3, pp. 927-934, March 2004.

[61] Y. Hu, J. C. Mollier, and J. Obregon, “A new method of third-order intermodulation reduction in nonlinear microwave systems,” *IEEE Trans. Microwave Theory Tech.*, vol. 34, no. 2, pp. 245-250, Feb. 1986.

[62] J. J. Majewski, "New method of phase noise and intermodulation distortion reduction in high-order QAM systems," *13th Int. Conf. on Microwaves, Radar and Wireless Comm.*, vol. 1, pp. 258-264, May 2000.

[63] W. J. Jenkins and A. Khanifar, "Power amplifier linearization through low-frequency feedback," *30th Europ. Microwave Conf.*, vol. 3, pp. 356-359, Oct. 2000.

[64] J. Sun;, Y. W. M. Chia, and B. Li, "A new BJT linearizer design for RF power amplifier," *Asia-Pacific Microwave Conf.*, pp. 1117-1121, Dec. 2000.

[65] M. R. Moazzam and C. S. Aitchison, "A low third order intermodulation amplifier with harmonic feedback circuitry," *IEEE MTT-S Int. Microwave Symp. Dig.*, pp. 827-830, 1996.

[66] N. Males-Ilic, B. Milovanovic, and D. Budimir, "Low intermodulation amplifiers for RF and microwave wireless systems," *Proc. Asia-Pacific Microwave Conf.*, vol. 3, pp. 984-987, Dec. 2001.

[67] J. R. Macdonald, "Nonlinear distortion reduction by complementary distortion," *IRE Trans. Audio*, vol. 7, pp. 128-133, Sept.-Oct. 1959.

[68] K. Yamauchi, K. Mori, M. Nakayama, Y. Itoh, Y. Mitsui, and O. Ishida, "A novel series diode linearizer for mobile radio power amplifiers," *IEEE MTT-S Int. Microwave Symp. Dig.*, pp. 831-834, 1996.

[69] J. Sun, B. Li, and M. Y. W. Chia, "Linearised and highly efficient CDMA power amplifier," *Electron. Lett.*, vol. 35, no. 10, pp. 786-787, May 1999.

[70] C. Haskins, T. Winslow, and S. Raman, "FET diode linearizer optimization for amplifier predistortion in digital radios," *IEEE Microwave and Guided Wave Lett.*, vol. 10 , no. 1 , pp. 21-23, Jan. 2000.

[71] K. Yamauchi, K. Mori, M. Nakayama, Y. Mitsui, and T. Takagi, "A microwave miniaturized linearizer using a parallel diode with a bias feed resistance," *IEEE Trans. Microwave Theory & Tech.*, vol. 45, no. 12, pp. 2431-2434, Dec. 1997.

[72] M. Bao, Y. Li, and A. Cathelin, "A 23 GHz active mixer with integrated diode linearizer in SiGe BiCMOS technology," *33rd Europ. Microwave Conf.*, vol. 1, pp. 391-393, Oct. 2003.

[73] S. Cha, T. Matsuoka, and K. Taniguchi, "A CMOS predistorter using a P+/N-well junction diode with a bias feed resistor," *Asia Pacific Microwave Conf.*, vol. 1, pp. 77-80, Nov. 4-7, 2003.

[74] T. Yoshimasu, M. Akagi, N. Tanba and S. Hara, "An HBT MMIC power amplifier with an integrated diode linearizer for low voltage portable phone applications," *IEEE J. Solid-State Circuits*, vol. 33, no. 9, pp. 1290-1296, Sept. 1998.

[75] H. Kawamura, K. Sakuno, T. Hasegawa, M. Hasegawa, H. Koh, and H. Sato, "A miniature 44% efficiency GaAs HBT power amplifier MMIC for the W-CDMA application," *22nd Anual GaAs IC Symp.*, pp. 25-28, Nov. 2000.

[76] K. Fujita, K. Shirakawa, N. Takahashi, Y. Liu, T. Oka, M. Yamashita, K. Sakuno, H. Kawamura, M. Hasegawa, H. Koh, K. Kagoshima, H. Kijima, and H. Sato, "A 5 GHz high efficiency and low distortion InGaP/GaAs HBT power amplifier MMIC," *IEEE MTT-S Int. Microwave Symp. Dig.*, vol. 2, pp. 871-874, June 2003.

[77] C.-C. Yen and H.-R. Chuang, "A 0.25-um 20-dBm 2.4-GHz CMOS power amplifier with an integrated diode linearizer," *IEEE Microwave and Wireless Components Lett.*, vol. 13, no. 2, pp. 45-47, Feb. 2003.

[78] Y. S. Noh and C. S. Park, "PCS/W-CDMA dual-band MMIC power amplifier with a newly proposed linearizing bias circuit," *IEEE J. Solid-State Circuits*, vol. 37, no. 9, pp. 1096-1099, Sept. 2002.

[79] J. H. Kim, Y. S. Noh, and C. S. Park, "MMIC power amplifier adaptively linearized with RF coupled active bias circuit for W-CDMA mobile terminals applications," *IEEE MTT-S Int. Microwave Symp. Dig.*, vol. 3, pp. 2209-2212, June 2003.

[80] Y. Yang, K. Choi, and K. P. Weller, "DC boosting effect of active bias circuits and its optimization for class-AB InGaP-GaAs HBT power amplifiers," *IEEE Trans. Microwave Theory & Tech.*, vol. 52, no. 5, pp. 1455-1463, May 2004.

[81] E. Taniguchi, T. Ikushima, K. Itoh, and N. Suematsu, "A dual bias-feed circuit design for SiGe HBT low-noise linear amplifier," *IEEE Trans. Microwave Theory & Tech.*, vol. 51, no. 2, pp. 414-421, Feb. 2003.

[82] J. Kaukovuori, M. Hotti, J. Ryynanen, J. Jussila, and K. Halonen, "A linearized 2-GHz SiGe low noise amplifier for direct conversion receiver," *IEEE Int. Symp. on Circ. and Syst.*, vol. II, pp. 200-203, May 2003.

[83] M.-G. Kim, C.-H. Kim, H.-K. Yu, and J. Lee, "An FET-level linearization method using a predistortion branch FET," *IEEE Microwave & Guided Wave Lett.*, vol. 9, no. 6, pp. 233-235, June 1999.

[84] G. Hau, T. B. Nishimura, and N. Iwata, "A highly efficient linearized wide-band CDMA handset power amplifier based on predistortion under various bias conditions," *IEEE Trans. Microwave Theory & Tech.*, vol. 49, no. 6, pp. 1194-1201, June 2001.

[85] K.-I. Jeon, Y.-S. Kwon, and S.-C. Hong, "Input harmonics control using non-linear capacitor in GaAs FET power amplifier," *IEEE MTT-S Int. Microwave Symp. Dig.*, vol. 2, pp. 817-820, June 1997.

[86] C. S. Yu, W. S. Chan, and W.-L. Chan, “1.9 GHz low loss varactor diode pre-distorter,” *Electron. Lett.*, vol. 35, no. 20, pp. 1681-1682, Sept. 1999.

[87] W. K. Lo, W. S. Chan, and C. W. Li, “Improved predistorter for GaAs FET power amplifier,” *Microwave and Opt. Tech. Lett.*, vol. 40, no. 3, pp. 211-213, Feb. 2004.

[88] C. Wang, M. Vaidyanathan, and L. E. Larson, “A capacitance-compensation technique for improved linearity in CMOS class-AB power amplifiers,” *IEEE J. Solid-State Circuits*, vol. 39, no. 11, pp. 1927-1937, Nov. 2004.

[89] S. Narayanan, “Intermodulation distortion of cascaded transistors,” *IEEE J. Solid-State Circuits*, vol. 4, no. 3, pp. 97-106, June 1969.

[90] G. W. Holbrook, “Reducing amplifier distortion,” *Electronic Tech.* (England), vol. 37, pp. 13-20, Jan. 1960.

[91] A. Katz, R. Sudarsanam, and D. Aubert, “A reflective diode linearizer for spacecraft applications,” *IEEE MTT-S Int. Microwave Symp. Dig.*, pp. 661-664, June 1985.

[92] T. Nojima and T. Konno, “Cuber predistortion linearizer for relay equipment in the 800 mhz band land mobile telephone system,” *IEEE Trans. Vehicular Technology*, vol. 34, no. 4, pp.169-177, Nov 1985.

[93] W. Huang and R. E. Saad, “Novel third-order distortion generator with residual IM2 suppression capabilities,” *IEEE Trans. Microwave Theory & Tech.*, vol. 46, no. 12, pp. 2372-2382, Dec. 1998.

[94] Y.-J. Jeon, H.-W. Kim, M.-S. Kim, Y.-S. Ahn, J.-W. Kim, J.-Y. Choi, D.-C. Jung, and J.-H. Shin, “Improved HBT linearity with a ”post-distortion”-type collector linearizer,” *IEEE Microwave and Wireless Components Lett.*, vol. 13, no. 3, pp. 102-104, March 2003.

[95] C. H. Kim, C. S. Kim, H. K. Yu, M. Park, and D. Y. Kim, “RF active balun circuit for improving small-signal linearity,” U.S. Patent 6 473 595, Oct. 29, 2002.

[96] R. A. Hall, “Nonlinear compensation,” *IEEE Trans. Comm. Tech.*, vol. 17, no. 6, pp. 700-704, Dec. 1969.

[97] J. Kim, M.-S. Jeon, J. Lee, and Y. Kwon, “A new ”active” predistorter with high gain and programmable gain and phase characteristics using cascode-FET structures,” *IEEE Trans. Microwave Theory & Tech.*, vol. 50, no. 11, pp. 2459-2466, Nov. 2002.

[98] M. Muraguchi and M. Aikawa, “A linear limiter: a 11-GHz monolithic low distortion variable gain amplifier,” *IEEE MTT-S Int. Microwave Symp. Dig.*, vol. 2, pp. 525-528, June 1991.

[99] K. Nishikawa and T. Tokumitsu, "An MMIC low-distortion variable-gain amplifier using active feedback," *IEEE Trans. Microwave Theory & Tech.*, vol. 43, no. 12, pp. 2812-2816, Dec. 1995.

[100] K. W. Kobayashi, D. C. Streit, A. K. Oki, D. K. Umemoto, and T. R. Block, "A novel monolithic HEMT LNA integrating HBT-tunable active-feedback linearization by selective MBE," *IEEE Trans. Microwave Theory & Tech.*, vol. 44, no. 12, pp. 2384-2391, Dec. 1996.

[101] N. Sushi, "A linear amplifier with non-linear feedback," *Inst. Elec. Commun. Engr. J.* (Japan), pp. 1212-1218, July 1967.

[102] H. S. Black, U.S. Patent 1 686 792, Issued Oct. 9, 1929.

[103] J. C. Schmoock, "An input stage transconductance reduction technique for high-slew rate operational amplifiers," *IEEE J. Solid-State Circuits*, vol. 10, no. 6, pp. 407-411, Dec. 1975.

[104] B. Gilbert, "The multi-tanh principle: a tutorial overview," *IEEE J. Solid-State Circuits*, vol. 33, no. 1, pp. 2-17, Jan. 1998.

[105] L. Sheng, J. C. Jensen, and L. E. Larson, "A wide-bandwidth Si/SiGe HBT direct conversion sub-harmonic mixer/downconverter," *IEEE J. Solid-State Circuits*, vol. 35, no. 9, pp. 1329-1337, Sept. 2000.

[106] S. K. Reynolds, B. A. Floyd, T. Beukema, T. Zwick, U. Pfeiffer, and H. Ainspan, "A direct-conversion receiver IC for WCDMA mobile systems," *IEEE J. Solid-State Circuits*, vol. 38, no. 9, pp. 1555-1560, Sept. 2003.

[107] H. Khorramabadi, "High-frequency CMOS continuous-time filters," Ph.D. dissertation, Univ. of Calif., Berkeley, Feb. 1985.

[108] K. Kimura, "Some circuit design techniques using two cross-coupled, emitter-coupled pairs," *IEEE Trans. Circ. & Syst., Part I*, vol. 41, no. 5, pp. 411-423, May 1994.

[109] C. Popa and D. Coada, "A new linearization technique for a CMOS differential amplifier using bulk-driven weak inversion MOS transistors," *Int. Symp. on Signals, Circuits and Systems*, vol. 2, pp. 589-592, July 2003.

[110] O. Mitrea, C. Popa, A. M. Manolescu, and M. Glesner, "A linearization technique for radio frequency CMOS Gilbert-type mixers," *Proc. 10th IEEE Int. Conf. on Electronics, Circuits and Systems*, vol. 3, pp. 1086-1089, Dec. 2003.

[111] Y. Ding and R. Harjani, "A +18dBm IIP3 LNA in 0.35um CMOS," *IEEE ISSCC*, pp. 162-163, Feb. 2001.

[112] D. Webster, J. Scott, and D. Haigh, "Control of circuit distortion by the derivative superposition method," *IEEE Microwave Guided Wave Lett.*, vol. 6, pp. 123-125, Mar. 1996.

[113] B. Kim, J.-S. Ko, and K. Lee, "A new linearization technique for MOSFET RF amplifier using multiple gated transistors," *IEEE Microwave & Guided Wave Lett.*, vol. 10, no. 9, pp. 371-373, Sept. 2000.

[114] T. W. Kim, B. Kim, and K. Lee, "Highly linear receiver front-end adopting MOSFET transcoductance linearization by multiple gated transistors," *IEEE J. Solid-State Circuits*, vol. 39, no. 1, pp. 223-229, Jan. 2004.

[115] S. Ock, K. Han, J.-R. Lee, and B. Kim, "A modified cascode type low noise amplifier using dual common source transistors," *IEEE MTT-S Int. Microwave Symp. Dig.*, pp. 1423-1426, 2002.

[116] C. Xin and E. Sanchez-Sinencio, "A linearization technique for RF low noise amplifier," *IEEE Int. Symp. on Circ. and Syst.*, vol. IV, pp. 313-316, May 2004.

[117] S. Tanaka, E. Behbahani, and A. A. Abidi, "A linearization technique for CMOS RF power amplifiers," *Symp. VLSI Circuits Dig.*, pp. 93-94, June 1997.

[118] Y.-S. Youn, J.-H. Chang, K.-J. Koh, Y.-J. Lee, and H.-K. Yu, "A 2GHz 16dBm IIP3 low noise amplifier in 0.25μm CMOS technology," *IEEE Int. Solid-State Circ. Conf.*, Paper 25.7, 2003.

[119] V. Aparin and L. E. Larson, "Analysis and reduction of cross modulation distortion in CDMA receivers," *IEEE Trans. Microwave Theory Tech.*, vol. 51, no. 5, pp. 1591-1602, May 2003.

[120] V. Aparin and C. Persico, "Effect of out-of-band terminations on intermodulation distortion in common-emitter circuits," *IEEE MTT-S Int. Microwave Symp. Dig.*, vol. 3, pp. 977-980, 1999.

[121] V. Aparin and L. E. Larson, "Linearization of monolithic LNAs using low-frequency low-impedance input termination," *Europ. Solid-State Circ. Conf.*, pp. 137-140, Sept. 2003.

[122] V. Aparin, G. Brown, and L. E. Larson "Linearization of CMOS LNAs via optimum gate biasing," *IEEE Int. Symp. on Circ. and Sys.*, vol. IV, pp. 748-751, May 2004.

[123] V. Aparin and L. E. Larson "Modified derivative superposition method for linearizing FET low-noise amplifiers," *IEEE Trans. Microwave Theory Tech.*, vol. 53, no. 2, Feb. 2005.

[124] J. E. Mazo, "Jitter comparison of tones generated by squaring and by fourth-power circuits," *Bell Syst. Tech. J.*, vol. 57, no. 5, pp. 1489-1498, May-June 1978.

[125] R. J. Marks II, *Introduction to Shannon Sampling and Interpolation*. New York: Springer-Verlag, 1991.

[126] W. Y. Ali-Ahmad, "RF system issues related to CDMA receiver specifications," *RF Design*, pp. 22-32, Sept. 1999.

[127] P. Wambacq and W. Sansen, *Distortion Analysis of Analog Integrated Circuits*. Norwell, MA: Kluwer, 1998.

[128] H. C. de Graaff and F. M. Klaassen, *Compact Transistor Modelling for Circuit Design*. New York: Springer-Verlag, 1990.

[129] K. L. Fong and R. G. Meyer, "High-Frequency Nonlinearity Analysis of Common-Emitter and Differential-Pair Transconductance Stages," *IEEE J. Solid-State Circuits*, vol. 33, pp. 548-555, April 1998.

[130] V. Aparin and C. J. Persico, "Impedance matching networks for non-linear circuits," U.S. Patent 6 166 599, Dec. 26, 2000.

[131] Y. Wang, S. V. Cherepko and J. C. M. Hwang, "Asymemetry in intermodulation distortion of HBT power amplifiers," *IEEE GaAs IC Symp.*, pp. 201-204, Oct. 2001.

[132] N. B. de Carvalho and J. C. Pedro, "A comprehensive explanation of distortion sideband asymmetries," *IEEE Trans. Microwave Theory Tech.*, vol. 50, no. 9, pp. 2090-2101, Sept. 2002.

[133] J. Brinkhoff and A. E. Parker, "Effect of baseband impedance on FET intermodulation," *IEEE Trans. Microwave Theory Tech.*, vol. 51, no. 3, pp. 1045-1051, March 2003.

[134] V. Aparin and P. J. Shah, "Circuit for linearizing electronic devices," U.S. Patent 6 717 463, Apr. 6, 2004.

[135] D. C. Ahlgren, N. King, G. Freeman, R. Groves, and S. Subbanna, "SiGe BiCMOS technology for RF device and design applications," *IEEE Radio and Wireless Conf. Proc.*, pp. 281-284, Aug. 1999.

[136] M. Kamat, P. Ye, Y. He, B. Agarwal, P. Good, S. Lloyd, and A. Loke, "High performance low current CDMA receiver front end using 0.18 /spl mu/m SiGe BiCMOS," *IEEE RFIC Symp.*, pp. 23-26, June 2003.

[137] P. Gould, J. Lin, O. Boric-Lubecke, C. Zelley, Y.-J. Chen, and R. H. Yan, "0.25-m BiCMOS receivers for normal and micro GSM900 and DCS 1800 base stations," *IEEE Trans. Microwave Theory Tech.*, vol. 50, no. 1, pp. 369-376, Jan. 2002.

[138] D. Wang, K. Krishnamurthi, S. Gibson, and J. Brunt, "A 2.5 GHz low noise high linearity LNA/mixer IC in SiGe BiCMOS technology," *IEEE RFIC Symp.*, pp. 249-252, May 2001.

[139] P. Leroux, J. Janssens, and M. Steyaert, "A 0.8dB NF ESD-protected 9-mW CMOS LNA operating at 1.23GHz," *IEEE J. Solid-State Circ.*, vol. 37, no. 6, pp. 760-765, June 2002.

[140] V. Aparin, "Bias method and circuit for distortion reduction," U.S. Patent 6 531 924, Mar. 11, 2003.

[141] M. J. M. Pelgrom, A. C. J. Duinmaijer, and A. P. G. Welbers, "Matching properties of MOS transistors", *IEEE J. Solid-State Circ.*, vol. 24, no. 5, pp. 1433-1440, Oct. 1989.

[142] H. P. Tuinhout, *Matching of MOS Transistors*. Advanced Engineering Course on Deep Submicron: Modeling and Simulation, Ecole Polytechnique Fdrale deLausanne, Lausanne, Switzerland, 12-15 Oct. 1998.

[143] M. J. M. Pelgrom, H. P. Tuinhout, and M. Vertregt, "Transistor matching in analog CMOS applications," *IEDM Dig.*, pp. 915-918, Dec. 1998.

[144] A. van der Ziel, *Noise in Solid State Devices and Circuits*. New York: Wiley, 1986.

[145] R. J. van Overstraeten, G. .J. deClerck, and P. A. Muls, "Theory of the MOS transistor in weak inversion - New method to determine the number of surface states," *IEEE Trans. Electron Devices*, vol. ED-22, p. 282, 1975.

[146] F. M. Klaassen and J. Prins, "Thermal noise of MOS transistors," *Philips Res. Repts*, vol. 22, pp. 505-514, 1967.

[147] E. N. Wu and A. van der Ziel, "Induced-gate thermal noise in high electron mobility transistors," *Solid-State Electronics*, vol. 26, no. 7, pp. 639-642, 1983.

[148] T. H. Lee, *The Design of CMOS Radio-Frequency Integrated Circuits*. Cambridge, U.K.: Cambridge Univ. Press, 1998, ch. 11.

[149] K.-H. To, Y.-B. Park, T. Rainer, W. Brown, and M. W. Huang, "High frequency noise characteristics of RF MOSFETs in subthreshold region," *IEEE RFIC Symp. Dig.*, pp. 163-167, June 2003.

[150] B. McNamara, S. Zhang, M. Murphy, H. M. Banzer, H. Kapusta, E. Rohrer, T. Grave, and L. Verweyen, "Dual-band/tri-mode receiver IC for N- and W-CDMA systems using 6"-PHEMT technology," *IEEE RFIC Symp. Dig.*, pp. 13-16, 2001.

[151] S. Kumar, M. Vice, H. Morkner, and L. Wayne, "Enhancement mode PHEMT low noise amplifier with LNA linearity control (IP3) and mitigated bypass switch," *IEEE RFIC Symp. Dig.*, pp. 213-216, June 2002.

[152] *TIA/EIA/IS-2000.1-A Introduction to CDMA2000 Standard for Spread Spectrum Systems*, March 2000

[153] "UE Radio transmission and reception (FDD)", Tech. Specification Group, 3GPP, TS 25.101, Release 6.6.0, Jan. 2005.

[154] V. Aparin and L. E. Larson, "Analysis of cross modulation in W-CDMA receivers," *IEEE MTT-S Int. Microwave Symp. Dig.*, vol. 2, pp. 787-790, June 2004.

[155] V. Aparin, G. Ballantyne, C. Persico, and A. Cicalini, "An integrated LMS adaptive filter of TX leakage for CDMA receiver front ends," Accepted for publication in *IEEE RFIC Symp.*, June 2005.